ATATURK
UNIVERSITY
PUBLICATIONS

NanoEra

Official journal of Atatürk University
Nanoscience and Nanoengineering Research and Application Center

Volume 5 • Issue 1 • June 2025

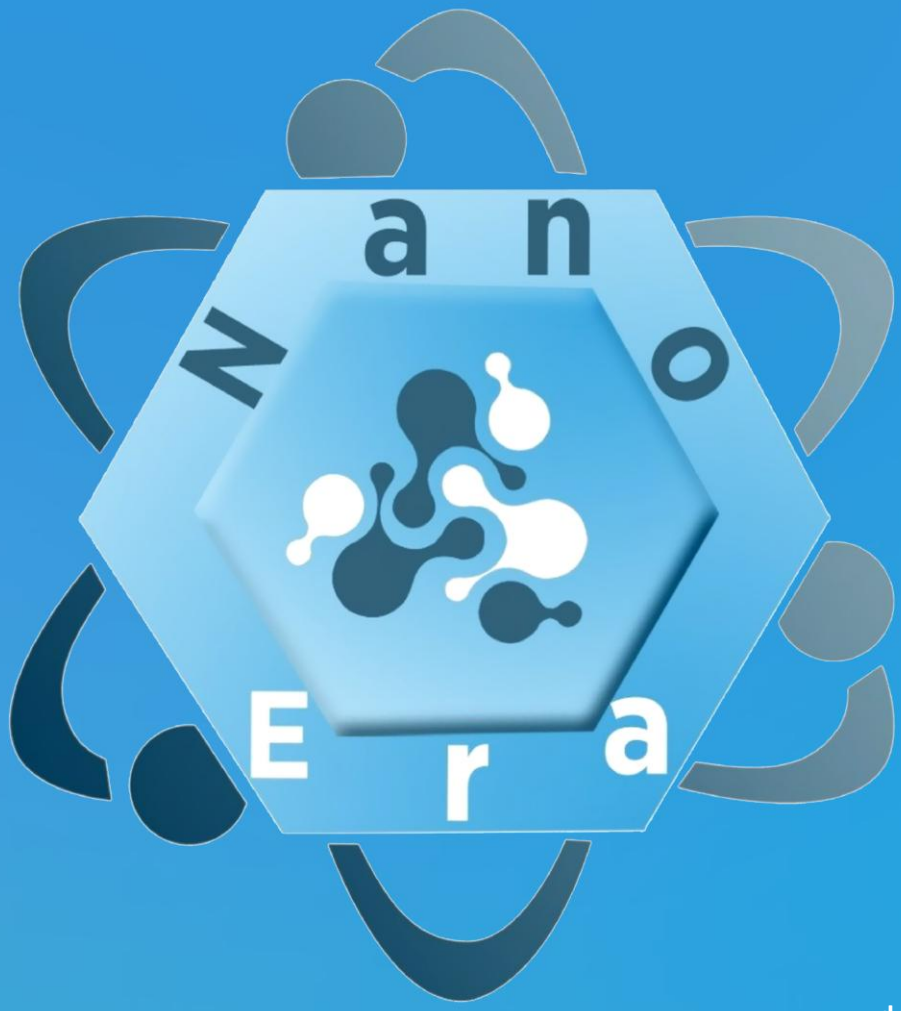

EISSN 2792-0666
dergipark.org.tr/nanoera

NanoEra

NanoEra

NanoEra is a peer reviewed, open access, online-only journal published by the Atatürk University, Nanoscience and Nanoengineering Research and Application Center.

NanoEra is a biannually journal that is published in English in June, and December.

NanoEra aims to contribute to the literature by publishing manuscripts at the highest scientific level in the fields of nanoscience and nanoengineering. The NanoEra journal publishes international scientific Research and Review articles in English (US).

Scope of the journal is all fields that are directly or indirectly related to research on the design, characterization, fabrication, and applications of structures, devices, and systems involving the manipulation or control of atomic, molecular, and nanoscale materials, and events.

Research areas covered in the journal

- 2D Materials
- Biomaterials & Nanobiotechnology
- Computational Nanotechnology
- Energy Storage & Applications
- Nanoelectronic Systems, Components & Devices
- Nanofabrication, Nanoprocessing & Nanomanufacturing
- Nanomaterials, Their Applications & Characterization
- Nanomedicine, Toxicology, Drug Delivery Systems & Biopharmaceutical
- Nanotechnology in Construction Industry
- Nanotechnology for Green Energy & Environment Sciences
- Organic and Inorganic Nanocomposites, Polymers
- Smart Textiles & Apparels

The target audience of the journal includes researchers and specialists who are interested or working in all fields of scope of the journal.

Abstracting and Indexing

NanoEra is covered in the following abstracting and indexing databases;
- EBSCO - Central & Eastern European Academic Source (CEEAS)
- EBSCO - H. W. Wilson Databases - Applied Science & Technology Source
- Gale Cengage

To guarantee that all papers published in the journal are maintained and permanently accessible, articles are stored in Dergipark which serves as a national archival web site and at the same time permits LOCKSS to collect, preserve, and serve the content.

Disclaimer

Statements or opinions expressed in the manuscripts published in the journal reflect the views of the author(s) and not the opinions of the editors, editorial board, and/or publisher; the editors, editorial board, and publisher disclaim any responsibility or liability for such materials.

Open Access Statement

You can find the current version of the Instructions to Authors at dergipark.org.tr/nanoera/writing-rules

Contact (Chief Editor)
Hayrunnisa NADARĞLU
Department of Food Technology, Vocational School of Technical Sciences, Atatürk University, Erzurum, Türkiye
hnisa25@atauni.edu.tr
nanoera@atauni.edu.tr
dergipark.org.tr/nanoera
+90 442 231 18 18

Contact (Publisher) / İletişim (Yayıncı)
Atatürk University
Atatürk University, Erzurum, Turkey
Atatürk Üniversitesi Rektörlüğü 25240 Erzurum, Türkiye
ataunijournals@atauni.edu.tr
bilimseldergiler.atauni.edu.tr
+90 442 231 15 16

NanoEra

CONTENTS

Research Articles

Review Article

ATATÜRK ÜNİVERSİTESİ YAYINLARI
ATATURK UNIVERSITY PUBLICATIONS

Research Article DOI: 10.5281/zenodo.15727928

Preparation and characterization of melamine formaldehyde organo clay nanocomposite foams (MFCNCF)

Elif ŞAHİN [1]

[1] Department of Nanoscience and Nanoengineering, Graduate School of Natural and Applied Sciences, Atatürk University, Erzurum, Türkiye

Ahmet GÜRSES [1, 2]

[1] Department of Nanoscience and Nanoengineering, Graduate School of Natural and Applied Sciences, Atatürk University, Erzurum, Türkiye

[2] Department of Chemistry Education, K.K. Education Faculty, Atatürk University, Erzurum, Türkiye

ABSTRACT

Melamine formaldehyde resins are one of the well-known thermosetting resins. It has been observed that melamine formaldehyde foam composites prepared with various nanoparticle reinforcements exhibit better mechanical, thermal and sound insulation properties. In this study, it was aimed to synthesize melamine formaldehyde organoclay nanocomposite foams and investigate their thermal insulation and mechanical stability by using microwave irradiation and heating technique together, which can offer advantages such as faster reaction, high yield and purity, reduced curing time. Pure melamine formaldehyde foam, MFF, and melamine formaldehyde organoclay nanocomposite foams, MFCNCFs, prepared with various organoclay contents were characterized by HRTEM, FTIR, SEM and XRD techniques. From spectroscopic and microscopic analyses, it was observed that organoclay platelets could be exfoliated with increasing clay content without undergoing much change in the resin matrix. The highest compressive strength was obtained in the MFCNCF3 foam with high organo clay content (0.68 N/mm^2) and the bulk density was determined to be quite low (0.20 g/cm^3). On the other hand, in the nanocomposite with 0.15 % organo clay content (MFCNCF2), a compressive strength of 0.32 N/mm^2 and a thermal conductivity coefficient of 0.065 W/m·K were measured.

Keywords: Melamine formaldehyde, Melamine formaldehyde organo clay nanocomposite, foam, Thermal insulation, Compressive strength

INTRODUCTION

Nanotechnology, which is used to refer to the design, construction and use of functional structures with at least one characteristic dimension measured in nanometers, has become increasingly popular in recent years.[1,2] Nanoparticles, which form the basis of nanotechnology, are incredibly small particles with a size of less than 100 nm and can contain carbon, metal, metal oxides or organic substances.[3] One of the most important features of nanotechnological studies is that the basic physical and chemical properties of a material or system at the nanoscale (e.g., melting temperature, thermal conductivity, load capacity, electronic conductivity, tensile strength and color) can be designed as desired and used in many different areas.[4] Nanoparticles provide improvements in the functionality of metal, ceramic, polymer or composite systems and are used in the development and production of many products in daily life.[5] Nanoparticles appear to have different physical, chemical, and biological properties compared to their larger counterparts, contributing to effects such as increased chemical reactivity, stability, or greater surface area relative to volume, greater mechanical strength, etc. Among the diverse uses of nanoparticles is polymer clay nanocomposites.[6]

Polymer clay nanocomposites can be made by directly mixing two aqueous solutions containing monomer and clay suspension, respectively, and subsequent polymerization induced by the addition of thermal or light sources or chemical oxidants.[7-12] Layered silicates are among the most widely studied nanofillers and are used in modified form. It is known that organoclay or silicates generally improve the properties of nanocomposites compared to traditional macro and micromaterials.[13-15] Organoclay particles are dispersed in the polymeric matrix in three different ways: phase separated (micro-composite) structure, intercalated (intercalated layered) structure and exfoliated (dispersed) structure.[16-18] There is also a mixed structure in which exfoliated and intercalated structures are seen together.

Three main techniques are used to obtain polymer/clay nanocomposites. These techniques differ according to the starting material and the preparation method. They are in situ (simultaneous) polymerization method, solution intercalation method and melt intercalation method (simultaneous) polymerization.[7,19,20] In situ polymerization method is a particularly suitable method for the preparation of thermoset polymer clay nanocomposites, but it has also been used for thermoplastics.[21-29]

Received 10.12.2024
Revised 10.01.2025
Accepted 01.03.2025
Publication Date 24.06.2025

Corresponding author:
Ahmet GÜRSES
E-mail:
agurses@atauni.edu.tr

Cite this article: Şahin E, Gürses A. Preparation and characterization of melamine formaldehyde organo clay nanocomposite foams (MFCNCF). *NanoEra*. 2025;5(1):1-8

Melamine formaldehyde (MF) is a hard, very durable and versatile resin with high flame and temperature resistance, and is synthesized by condensation of melamine and formaldehyde. MF resins have good flame-retardant properties since they release nitrogen gas during combustion. It is emphasized in the literature that the mechanical, thermal and barrier properties of MF nanocomposites are not at the desired level. Improving these properties with various methods is of great importance in terms of the field of use of nanocomposites. It can be said that there is a significant gap in the literature on this subject. For this reason, the aim of the presented study was to synthesize nanoclay reinforced, cross-linked melamine formaldehyde organo clay nanocomposite foams (MFCNCF) by microwave irradiation technique and to investigate the thermal, mechanical and morphological properties of these composites.

MATERIALS and MERHOD

Raw montmorillonite (MMT), supplied from Karakayalar A.Ş. in Çankırı province, Türkiye, with a specific surface area of 64.2 m^2/g and X-ray Fluorescence (XRF) composition given in Table 1, was used for the synthesis of organo montmorillonite (OMMT) to be used in the preparation of nanocomposites.

Table 1. X-ray Fluorescence (XRF) chemical compositions of Montmorillonite (MMT).

Component (%)	
SiO_2	59.32
Al_2O_3	17.19
Fe_2O_3	5.95
MgO	3.63
CaO	2.21
Na_2O	1.68
K_2O	0.97
TiO_2	0.74
SO_3	0.51
Other	7.81

Melamine, formaldehyde (37 wt%), NaOH, acetic acid, Tween 80, a nonionic surfactant (polyoxyethylene (20) sorbitan monooleate), and analytical grade glycerin (all supplied by Merck KGaA, Germany) were used for the preparation of melamine formaldehyde (MFF) and melamine formaldehyde organoclay composite foams (MFCNCF). In addition, gasoline, a mixture of isooctane, butane, and 3-ethyltoluene used for foaming, was supplied by a local gas station.

MERHOD

Preparation of organo clay

Montmorillonite (MMT), a cationic surfactant, cetyltrimethylammonium bromide and CTAB (Merck Co.) suspensions, a hydrocarbon material that is a product of petroleum refining and some of the properties of which are given in Table 2, were used to prepare organoclay by solution intercalation method. The procedure applied for the synthesis of organo-montmorillonite (OMMT) is the same as in our previous work.[30,31]

Table 2. Some characteristics of the hydrocarbon material.

Density (15°C), kg/m^3	990.7
Calorific Value MJ/kg	42.74
Flash Point °C	105.8
Water by Distillation, wt. %	0.1
C	83.4
H	11.9
N	0.8
S	1.5
Ash	0.03

Preparation of melamine formaldehyde foam (MFF) and melamine formaldehyde organo clay nanocomposite foams (MFCNCF)

Melamine and formaldehyde (37% by weight) (mass ratio: 0.67:0.33) were placed in a three-necked flat-bottomed flask with a thermometer and cooling equipment connected, then mixed with a magnetic stirrer and then heated under reflux until dissolution at approximately 60°C. The pH was adjusted to 8.5 with 40% by weight NaOH solution. Considering the viscosity of the mixture, it was heated under reflux at approximately 95°C for 60 minutes. Then, a certain amount of concentrated acetic acid, 1.0 wt.% glycerin and Tween 80 as well as 6.0 wt.% gasoline was added to the obtained prepolymer and mechanically mixed vigorously to homogenize the mixture. In addition, when preparing untreated melamine formaldehyde foam (MFF), the same processes were performed using only melamine and formaldehyde (37% by weight) (mass ratio: 0.68:0.32). When preparing the MF-organoclay nanocomposite via in situ synthesis, 0.1%, 0.15% and 0.45% organoclay was added to the container by weight. For foam synthesis, the mixture was exposed to microwave radiation in a microwave oven for 2 minutes in a suitable container. Finally, the mixture was placed in a modular square aluminum mold with a volume of 10.0 x 10.0 x 1.0 cm^3 and cured by heat treatment at 140°C for 1 hour in a hot air heated oven to remove water and residual formaldehyde and complete the process.

Table 3. Sample Codes and Contents of Pure Melamine Formaldehyde Foam (MFF) and MF-organoclay Nanocomposite Foams (MFCNCF1-3).

Sample Codes	Nano Filler	(%w)
MFF	-	-
MFCNCF1	Organo clay	0.10
MFCNCF2	Organo clay	0.15
MFCNCF3	Organo clay	0.45

Spectroscopic and microscopic analyses and measurements of compressive strength and thermal conductivity

Structural, crystallographic and textural characterization of virgin MF foam and MF organo clay nanocomposite foams were performed using spectroscopic techniques such as XRD and FTIR and microscopic techniques such as HRTEM and SEM.

XRD diffractograms for the prepared samples were obtained using a PANalytical Empyrean X-ray diffractometer with Cu Ka (1.540 Å) radiation operating at 5 kV and 40 mA for 2h in the 9°–90° range and a scan rate of 4/min (Malvern PANalytical Ltd., United Kingdom).

FTIR spectra were obtained using a Vertex 70V FTIR spectrometer with a mid-IR ceramic source in the range of 4,000 to 400 cm^{-1}, an average of 100 scans and a resolution of 1 cm^{-1} (Bruker Optics Inc., USA).

HRTEM images of the samples were taken using a HITACHI HT7700 high-resolution transmission electron microscope (LaB6 filament) operating at 120.0 kV (Hitachi Ltd, Japan).

SEM patterns of virgin MFF and MF organo clay nanocomposite foams were taken using SEM (FEI-INSPECT S50 model) at 30 kV.

Compressive strength of virgin MFF and MFCNCF foams were performed using a universal testing machine (Zwick/Roell) according to DIN ISO 844:2009-10 standard. The thermal conductivity coefficients of virgin MFF and MFCNCF foams were also measured using a thermal conductivity meter (Quick Thermal Conductivity Meter QTM-500, Japan) with a probe consisting of a single heating wire and a thermocouple.

RESULTS

Textural characterization of melamine formaldehyde foam (MFF) and melamine formaldehyde organoclay nanocomposites (MFCNCF)

In order to compare the differences in the textural structures of raw montmorillonite (MMT) and organo-montmorillonite (OMMT) and to see the effectiveness of the modification, HRTEM images of both were taken and are given in Figure 1. The dark long-fiber lines seen in the HRTEM images indicate clay layers with their 2:1 layered structure. HR-TEM images of melamine formaldehyde foam (MFF) (a) and melamine formaldehyde-organoclay foams containing varying organoclay ratios (MFCNCF1-3 (b-d)) are given in Figure 2.

Figure 2a shows that pure melamine formaldehyde resin is formed as agglomerated microspheres and the aggregates develop in three dimensions.[32,33] This textural arrangement is due to the use of microwave irradiation-assisted foaming method before curing. Figure 2b shows that due to the exfoliation of organoclay layers into the polymer matrix, MF molecule clusters are regularly sparse or separated while maintaining their spherical structures.[34] As the amount of clay increases, the structures of spherical MF molecules are thoroughly separated (Figures 2c and 2d).

Surface morphological characterization of melamine formaldehyde foam (MFF) and melamine formaldehyde organoclay nanocomposite foams (MFCNCF)

SEM patterns taken for pure melamine formaldehyde foam (MFF) and MF-organoclay nanocomposite foams (MFCNCF1-3) are given in Figure 3.

It can be seen that Figure 3a clearly reflects the surface morphology of pure melamine formaldehyde foam (MF) formation. This textural structuring shows that the microsphere clusters develop as three-dimensional branched structures.[32,35,36] However, it can be seen from Figure 3b that the branched structure almost disappears and the MF molecule clusters show regular stacking, resulting in a more uniform surface morphology due to the exfoliation of organoclay flakes in the polymeric matrix. It can be seen from Figures 3c and 3d that the morphological structures are similar.

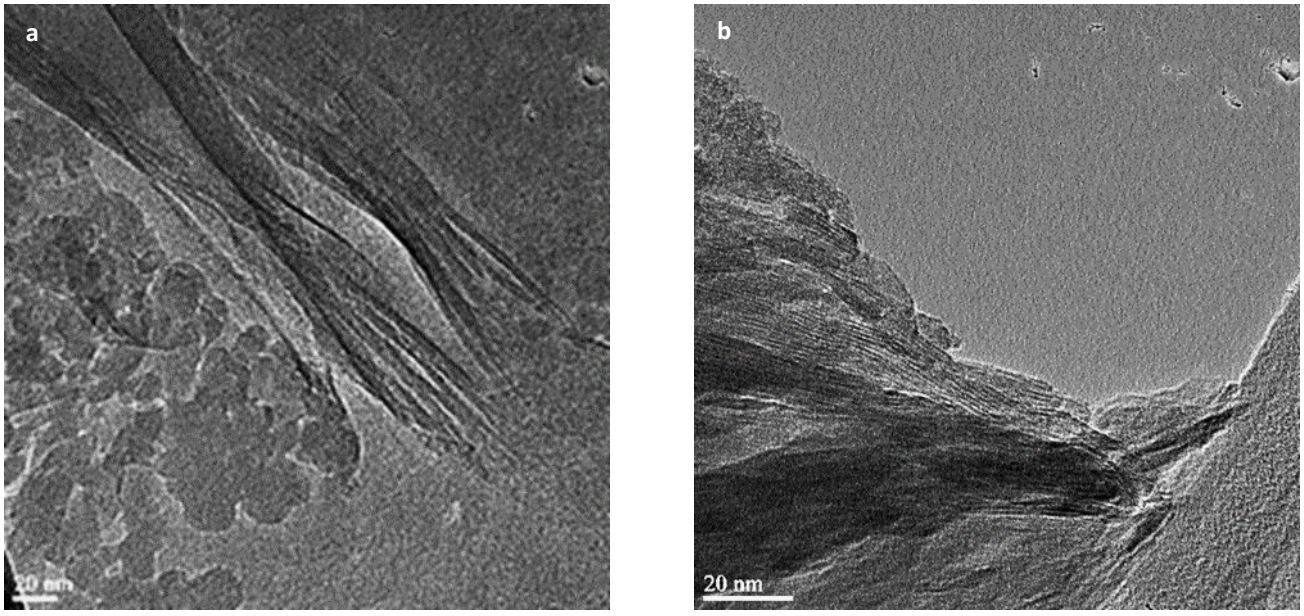

Figure 1. HRTEM images of raw montmorillonite (MMT) (a), Organo-montmorillonite (OMMT) (b).

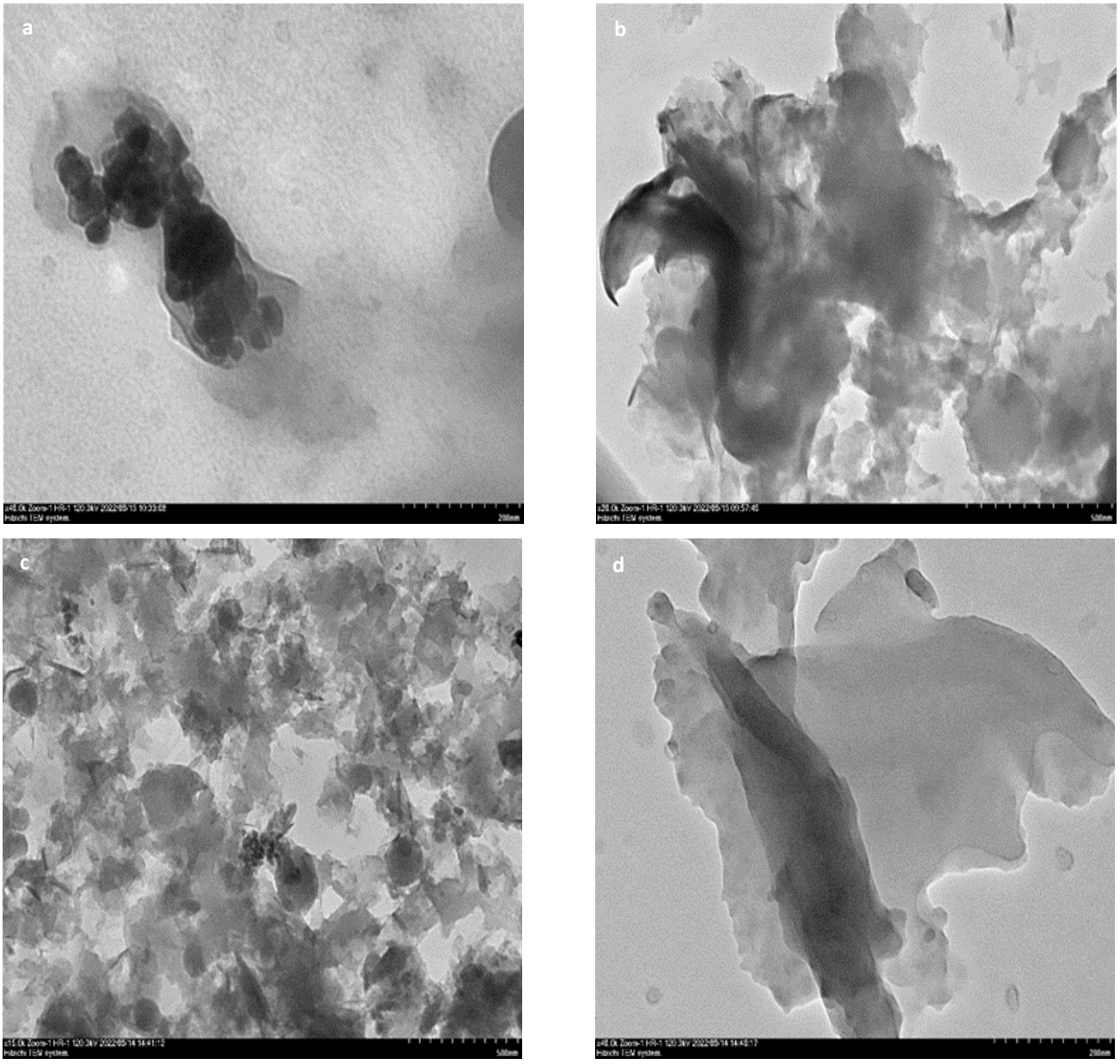

Figure 2. HR-TEM images of melamine formaldehyde foam (MFF) (a) and melamine formaldehyde-organoclay foams containing varying organoclay ratios (MFCNCF1-3 (b-d).

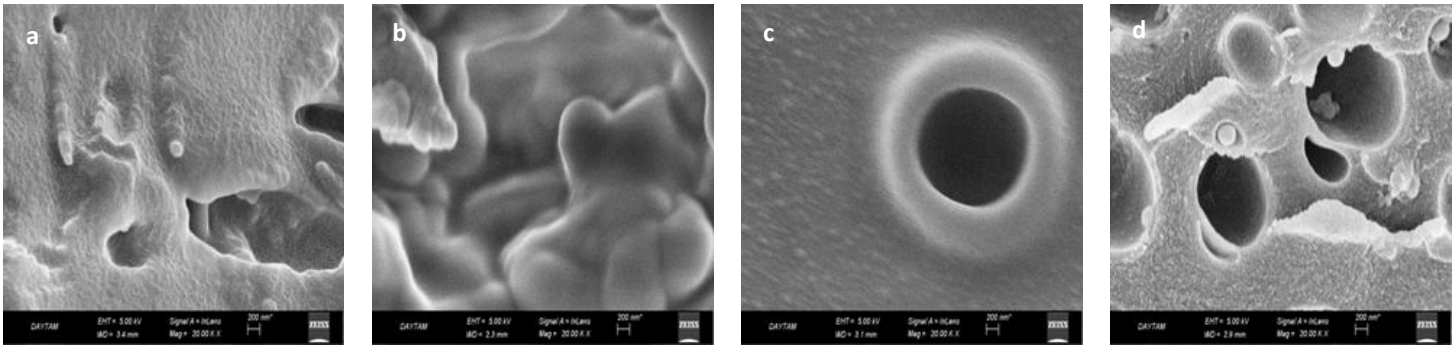

Figure 3. SEM patterns of pure melamine formaldehyde foam (MFF) (a) and MF-organoclay nanocomposite foams containing different clay ratios (MFCNCF1-3) (b-d).

Analysis of FT-IR spectra of melamine formaldehyde foam (MFF) and melamine formaldehyde organoclay nanocomposite foams (MFCNCF)

FT-IR spectra of pure melamine formaldehyde foam (MF) and MF-organoclay nanocomposite foams (MFCNCF) are given in Figure 4.

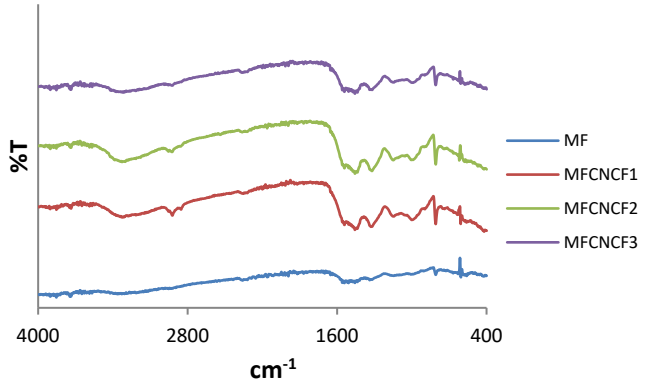

Figure 4. FT-IR spectra of pure melamine formaldehyde foam (MFF) and MF-organoclay nanocomposite foams containing different clay ratios (MFCNCF1-3).

In the FT-IR spectrum of the MF-organoclay nanocomposite foam (MFCNCF) in Figure 4, apart from the strong peak at 3354 cm^{-1} originating from the water-derived hydroxyl group, there are three more peaks at 2926, 2914 and 2881 cm^{-1}, which are the peaks belonging to the secondary amine group stretching, C–H anti-stretching and C–H stretching vibrations.[37] All these specific peaks appear at lower intensities and shift to lower values due to interactions between CTA+ ions bound by clay layers and long-chain hydrocarbon molecules. In addition, two peaks were observed at 1454 cm^{-1} and 1129 cm^{-1}, corresponding to the C–N stretching and the N–H bending of CTAB, respectively. On the other hand, it can be claimed that the peaks appearing in the 1302–1657 cm^{-1} region are due to the CH_2 shift vibration mode and the O–H bending mode of the water molecule around the attached head group. Si-O and Al-OH are the main functional groups observed in the range of 1000 cm^{-1} to 500 cm^{-1}. The peak at 866 cm^{-1} corresponds to Al-OH bending vibrations, while the double Si-O-Si bonds in SiO_2 at 802 cm^{-1} and the Si-O stretching vibrations observed around 714-617 cm^{-1} indicate the presence of quartz. The emergence of characteristic peaks with low intensity and shifted from their specific values may be indicative of intense interactions between clay plates and CTA+ ions bound to long-chain hydrocarbons.[38,39]

Characterization of mineralogical structures of melamine formaldehyde foam (MFF)and melamine formaldehyde organoclay nanocomposite foams (MFCNCF)

Figure 5 shows the XRD diffraction patterns of pure melamine formaldehyde foam (MF) and containing different clay ratios MF-organoclay nanocomposite foams (MFCNCF1-3).

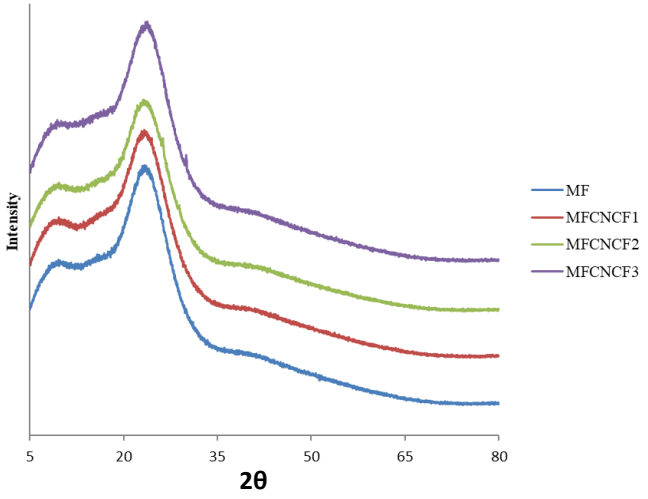

Figure 5. XRD diffractograms of pure melamine formaldehyde foam and MF-organoclay nanocomposite foams (MFCNCF1-3) containing different clay ratios.

Figure 5 shows that two typical broad peaks at 9.4° and 23.8°appeared in the XRD pattern of MF foam, indicating an amorphous structure. This means that the formaldehyde resin of melamine is composed of methylol monomers and the polymeric backbone is spread. It can be seen from Figure 5 that the smaller of the two peaks of MF resin partially overlaps with the characteristic smectite peak at 8.1°.[38,40] This left-shifted and enlarged smectite peak clearly indicates that the polymer molecules can enter the interlayer space of the clay and the nanocomposite is formed. The HRTEM image in Figure 1b also supports this claim.

Thermal conductivities of melamine formaldehyde foam (MFF) and melamine formaldehyde organoclay nanocomposite foams (MFCNCF)

Thermal conductivity is an important indicator for evaluating the thermal performance of a material under constant conditions. Thermal conductivity coefficients measured for different samples were considered in the evaluation of the thermal insulation performance of materials [41]. The thermal conductivity coefficients of pure melamine formaldehyde foam (MFF) and MF-organoclay nanocomposite foams containing different proportions of clay (MFCNCF1-3) are shown in Table 4.

Table 4. Thermal Conductivity Analysis Results of Pure Melamine Formaldehyde Foam and Containing Different Clay Ratios MF-organoclay Nanocomposite Foams

Sample Codes	Heat Conductivity Coefficient (λ) (W/m·K)	Standard Deviation
MFF	0.0826	0.0012
MFCNCF1	0.0869	0.0021
MFCNCF2	0.0650	0.0048
MFCNCF3	0.0812	0.0036

When Table 4 is examined, it is seen that MFCNCF2 has the smallest heat transfer coefficient. This shows that MFCNCF2 can be used as an alternative to insulation materials.

Dependence of density and compressive strength of melamine formaldehyde foam (MF) and melamine formaldehyde organoclay nanocomposite foams on their compositions

Compressive strength is an important mechanical property measured by placing a material directly under compressive loads. Compressive strength is also a critical design feature, and composite materials can exhibit some unique compressive strength behaviors depending on the composite structure. Some materials fracture at the limit of their compressive strength, and some deform irreversibly, so a certain amount of deformation can be considered the limit of the compressive load. Table 5 shows the bulk density and compressive strength values of pure MF foam and MF organo clay nanocomposite foams (MFCNCF1-3).

Table 5. Variation of Density and Compressive Strength of Melamine Formaldehyde Foam (MF) and Melamine Formaldehyde Organoclay Nanocomposite Foams Depending on Their Compositions

Sample Codes	Bulk Density (g/cm^3)	Compressive Strength (N/mm^2)	Standard Deviation
MFF	0.26	0.270	0.002
MFCNCF1	0.39	0.230	0.001
MFCNCF2	0.18	0.320	0.002
MFCNCF3	0.20	0.680	0.007

When Table 5 is examined, it is seen that MFCNCF3 has the highest compressive strength. With increasing clay ratio, the compressive strength has increased approximately threefold. It can be said that the three-fold increase in compressive strength, especially observed at high organoclay ratio, provides increased ductility due to improved adhesion interactions in the brittle MF foam matrix of organoclay plates.

CONCLUSION

This study focused on the synthesis of melamine formaldehyde organoclay nanocomposite foams using microwave irradiation and heating technique together and the investigation of their thermal insulation and mechanical stability.

- Advantages such as faster reaction, high yield and purity, and reduced curing time were obtained with microwave irradiation.
- HRTEM, FTIR, SEM and XRD techniques were used for the characterization of pure melamine formaldehyde foam, MFF and melamine formaldehyde organoclay nanocomposite foams, MFCNCFs, prepared with various organoclay contents. From spectroscopic and microscopic analyses, it was observed that organoclay platelets were exfoliated with increasing clay content without much structural change in the resin matrix.
- The highest compressive strength was obtained in MFCNCF3 foam with high organoclay content (0.68 N/mm^2) and it was determined that its bulk density was quite low (0.20 g/cm^3).
- In the nanocomposite (MFCNCF2) with 0.15% organo clay content, the compressive strength was measured as 0.32 N/mm^2 and the thermal conductivity coefficient was measured as 0.065 W/m·K.

Peer-review: Externally peer-reviewed.

Author Contributions: Concept – A.G.; Design – A.G.; Supervision – A.G.; Resources – A.G., E.S.; Data Collection and/or Processing – E.S.; Analysis and/or Interpretation – A.G., E.S.; Literature Search – E.S.; Writing Manuscript – A.G., E.S.; Critical Review – A.G.

Conflict of Interest: The authors have no conflicts of interest to declare.

Financial Disclosure: This study was supported by Atatürk University Scientific Research Projects Coordination Unit (BAP) (Project Code: FDK-2022-10258). The authors are grateful to Atatürk University for their financial support.

REFERENCES

1. Kelsall R, Hamley IW, Geoghegan M, eds. *Nanoscale Science and Technology*. John Wiley & Sons, Ltd; 2005. https://www.wiley.com/en-gb/Nanoscale+Science+and+Technology-p-9780470850862
2. Ramsden J. *Nanotechnology: An Introduction*. 2nd ed. Elsevier; 2016. doi:10.1016/C2014-0-03912-3
3. Roco MC. The long view of nanotechnology development: the National Nanotechnology Initiative at 10 years. *J Nanoparticle Res*. 2011;13(2):427-445. doi:10.1007/s11051-010-0192-z
4. Dahman Y. *Nanotechnology and Functional Materials for Engineers*. Elsevier; 2017.
5. Yakar Z. *Nanotechnology 1: Fundamentals of Nanotechnology*. (Ersöz M, Işıtan A, Balaban M, eds.). BilalOfset; 2018. https://hdl.handle.net/11499/3117%09
6. Yang B, Chen J, Liu B, Ding Y, Tang Y, Yan X. One dimensional graphene nanoscroll-wrapped MnO nanoparticles for high-performance lithium ion hybrid capacitors. *J Mater Chem A*. 2021;9(10):6352-6360. doi:10.1039/D1TA00404B
7. LeBaron PC, Wang Z, Pinnavaia TJ. Polymer-layered silicate nanocomposites: an overview. *Appl Clay Sci*. 1999;15(1-2):11-29. doi:10.1016/S0169-1317(99)00017-4
8. Thostenson E, Li C, Chou T. Nanocomposites in context. *Compos Sci Technol*. 2005;65(3-4):491-516. doi:10.1016/j.compscitech.2004.11.003
9. Balta JA, Simpson J, Michaud V, Månson J-AE, Schrooten J. Embedded shape memory alloys confer aerodynamic profile adaptivity. *Smart Mater Bull*. 2001;2001(12):8-12. doi:10.1016/S1471-3918(01)80094-0
10. Bernet N, Wakeman MD, Bourban P-E, Månson J-AE. An integrated cost and consolidation model for commingled yarn based composites. *Compos Part A Appl Sci Manuf*.

2002;33(4):495-506. doi:10.1016/S1359-835X(01)00140-3
11. Clifford S, Jansson N, Yu W, Michaud V, Månson J-A. Thermoviscoelastic anisotropic analysis of process induced residual stresses and dimensional stability in real polymer matrix composite components. *Compos Part A Appl Sci Manuf*. 2006;37(4):538-545. doi:10.1016/j.compositesa.2005.05.008
12. Jansson N, Wakeman WD, Månson J-AE. Optimization of hybrid thermoplastic composite structures using surrogate models and genetic algorithms. *Compos Struct*. 2007;80(1):21-31. doi:10.1016/j.compstruct.2006.02.036
13. Giannelis EP. Polymer Layered Silicate Nanocomposites. *Adv Mater*. 1996;8(1):29-35. doi:10.1002/adma.19960080104
14. Thostenson ET, Ren Z, Chou T-W. Advances in the science and technology of carbon nanotubes and their composites: a review. *Compos Sci Technol*. 2001;61(13):1899-1912. doi:10.1016/S0266-3538(01)00094-X
15. Chen G, Wu C, Weng W, Wu D, Yan W. Preparation of polystyrene/graphite nanosheet composite. *Polymer (Guildf)*. 2003;44(6):1781-1784. doi:10.1016/S0032-3861(03)00050-8
16. Kumar AP, Depan D, Singh Tomer N, Singh RP. Nanoscale particles for polymer degradation and stabilization—Trends and future perspectives. *Prog Polym Sci*. 2009;34(6):479-515. doi:10.1016/j.progpolymsci.2009.01.002
17. Kiliaris P, Papaspyrides CD. Polymer/layered silicate (clay) nanocomposites: An overview of flame retardancy. *Prog Polym Sci*. 2010;35(7):902-958. doi:10.1016/j.progpolymsci.2010.03.001
18. Judah H. The Synthesis, Characterisation and Rheological Properties of Clay-Polymer Nanocomposites. *Sheff Hallam Univ*. Published online 2019. doi:https://doi.org/10.7190/shu-thesis-00316
19. Ogata N, Kawakage S, Ogihara T. Poly(vinyl alcohol)-clay and poly(ethylene oxide)-clay blends prepared using water as solvent. *J Appl Polym Sci*. 1997;66(3):573-581. doi:10.1002/(SICI)1097-4628(19971017)66:3<573::AID-APP19>3.0.CO;2-W
20. Rehab A, Salahuddin N. Nanocomposite materials based on polyurethane intercalated into montmorillonite clay. *Mater Sci Eng A*. 2005;399(1-2):368-376. doi:10.1016/j.msea.2005.04.019
21. Usuki A, Kawasumi M, Kojima Y, Okada A, Kurauchi T, Kamigaito O. Swelling behavior of montmorillonite cation exchanged for ω-amino acids by ∈-caprolactam. *J Mater Res*. 1993;8(5):1174-1178. doi:10.1557/JMR.1993.1174
22. Lan T, Kaviratna PD, Pinnavaia TJ. Mechanism of Clay Tactoid Exfoliation in Epoxy-Clay Nanocomposites. *Chem Mater*. 1995;7(11):2144-2150. doi:10.1021/cm00059a023
23. Li Y, Zhao B, Xie S, Zhang S. Synthesis and properties of poly(methyl methacrylate)/montmorillonite (PMMA/MMT) nanocomposites. *Polym Int*. 2003;52(6):892-898. doi:10.1002/pi.1121
24. Lee DC, Jang LW. Characterization of epoxy-clay hybrid composite prepared by emulsion polymerization. *J Appl Polym Sci*. 1998;68(12):1997-2005. doi:10.1002/(SICI)1097-4628(19980620)68:12<1997::AID-APP14>3.0.CO;2-P
25. Azeez AA, Rhee KY, Park SJ, Hui D. Epoxy clay nanocomposites – processing, properties and applications: A review. *Compos Part B Eng*. 2013;45(1):308-320. doi:10.1016/j.compositesb.2012.04.012
26. Xie T, Yang G, Fang X, Ou Y. Synthesis and characterization of poly(methyl methacrylate)/montmorillonite nanocomposites by in situ bulk polymerization. *J Appl Polym Sci*. 2003;89(8):2256-2260. doi:10.1002/app.12468
27. Gürses A, Şahin E. Preparation of Melamine Urea Formaldehyde Organo Clay Nanocomposite Foams Using Thermal Processing and Microwave Irradiation Techniques and Investigation of Their Thermal Insulation and Compressive Strength. *Polym Sci Ser B*. 2024;66(1):117-128. doi:10.1134/S1560090424600396
28. Vaia RA, Giannelis EP. Lattice Model of Polymer Melt Intercalation in Organically-Modified Layered Silicates. *Macromolecules*. 1997;30(25):7990-7999. doi:10.1021/ma9514333
29. Tseng C, Wu J, Lee H, Chang F. Preparation and characterization of polystyrene–clay nanocomposites by free-radical polymerization. *J Appl Polym Sci*. 2002;85(7):1370-1377. doi:10.1002/app.10585
30. Gürses A, Güneş K, Mindivan F, Korucu ME, Açıkyıldız M, Doğar Ç. The investigation of electrokinetic behaviour of micro-particles produced by CTA+ ions and Na-montmorillonite. *Appl Surf Sci*. 2014;318:79-84. doi:10.1016/j.apsusc.2014.01.036
31. Singla P, Mehta R, Upadhyay SN. Clay Modification by the Use of Organic Cations. *Green Sustain Chem*. 2012;02(01):21-25. doi:10.4236/gsc.2012.21004
32. Santos EC dos, Bandeira RM, Vega ML, Santos Junior JR dos. Poly(melamine-formaldehyde-silica) Composite Hydrogel for Methylene Blue Removal. *Mater Res*. 2021;24(4). doi:10.1590/1980-5373-mr-2020-0574
33. Naresh R, Parameshwaran R, Vinayaka Ram V. Microcapsules of n-dodecanoic acid/melamine-formaldehyde with enhanced thermal energy storage capability for solar applications. *J Sci Adv Mater Devices*. 2022;7(3):100462. doi:10.1016/j.jsamd.2022.100462
34. Gürses A, Şahin E. Preparation of Melamine Formaldehyde Foam and a Melamine-Formaldehyde-Organo-Clay Nanocomposite and Hybrid Composites. *Minerals*. 2023;13(11):1407. doi:10.3390/min13111407
35. Gao Y, Liu S, Wang Q, Wang G. Preparation of melamine–formaldehyde resin grafted by (3-aminopropyl) triethoxysilane for high-performance hydrophobic materials. *J Appl Polym Sci*. 2020;137(19). doi:10.1002/app.48664
36. Nemanič V, Zajec B, Žumer M, Figar N, Kavšek M, Mihelič I. Synthesis and characterization of melamine–formaldehyde rigid foams for vacuum thermal insulation. *Appl Energy*. 2014;114:320-326. doi:10.1016/j.apenergy.2013.09.071
37. Chen Z, Wang J, Yu F, Zhang Z, Gao X. Preparation and

properties of graphene oxide-modified poly(melamine-formaldehyde) microcapsules containing phase change material n-dodecanol for thermal energy storage. *J Mater Chem A*. 2015;3(21):11624-11630. doi:10.1039/C5TA01852H

38. Gürses A, Doğar Ç, Köktepe S, Mindivan F, Güneş K, Aktürk S. Investigation of Thermal Properties of PUF/colored Organoclay Nanocomposites. *Acta Phys Pol A*. 2015;127(4):979-983. doi:10.12693/APhysPolA.127.979
39. Wanyika H, Maina E, Gachanja A, Marika D. Instrumental characterization of montmorillonite clays by X-ray fluorescence spectroscopy, fourier transform infrared spectroscopy, X-ray diffraction and UV/visible spectrophotometry. *J Agric Sci Technol*. 2016;17(1):224-239. https://www.ajol.info/index.php/jagst/article/view/219175
40. Yu C, Xu W, Zhao X, Xu J, Jiang M. Effects of the reaction degree of melamine-formaldehyde resin on the structures and properties of melamine-formaldehyde/polyvinyl alcohol composite fiber. *Fibers Polym*. 2014;15(9):1828-1834. doi:10.1007/s12221-014-1828-x
41. Amaral C, Vicente R, Ferreira VM, Silva T. Polyurethane foams with microencapsulated phase change material: Comparative analysis of thermal conductivity characterization approaches. *Energy Build*. 2017;153:392-402. doi:10.1016/j.enbuild.2017.08.019

ATATÜRK ÜNİVERSİTESİ YAYINLARI
ATATURK UNIVERSITY PUBLICATIONS

Research Article DOI: 10.5281/zenodo.15729047

Investigation of the physicochemical and textural properties of yogurt made from milk with different somatic cell count

Tamer TURGUT [1]

[1] Department of Food Processing, Vocational School of Technical Science, Atatürk University, Erzurum, Türkiye

Abdulkerim DİLER [1, 2]

[2] Department of Plant and Animal Science, Vocational School of Technical Science, Atatürk University, Erzurum, Türkiye

ABSTRACT

In dairy cows, infection of the mammary gland leads to a significant increase in the somatic cell count (SCC) in the milk. This increase has a negative effect on the physical and chemical composition of the milk. The aim of this study was to analyze the effect of three different SCC content on the physicochemical and textural properties of yogurt during a 28-day storage period. For this purpose, yogurts were made from milk with three different SCC values: low (<100,000 cells/ml), medium (100,000-500,000 cells/ml) and high (>500,000 cells/ml). Analyses were performed on days 1, 7, 14, 21 and 28 of storage.

The SCC content of the milk had a significant effect on the pH value, titratable acidity (TA) and syneresis values of the yogurts, but no significant effect on water holding capacity (WHC), dry matter (DM) and fat content. The highest acidity values were found in yogurts made from milk with a low SCC content. The evaluations of the color parameters in the yogurts were only influenced by the storage time. The color parameters (L* a* b*) decreased during storage. In particular, significant effects were observed on the color parameters after 21 days of storage. The SCC content of the milk had no significant effect on the color parameters (L*, a*, C*) of the yogurts. The SCC content of the milk had a significant effect on the texture parameters (hardness, adhesiveness, cohesiveness, resilience). Yogurt made from milk with a higher SCC value had lower values for hardness and adhesiveness values, and consequently had unsatisfactory texture.

Keywords: Somatic cell count (SCC), Syneresis, Yogurt quality, Yogurt texture.

INTRODUCTION

Somatic cells (SC) are nano-sized cells found in milk and consist of dead epithelial cells from the mammary gland as well as leukocytes from the blood. Epithelial cells appear in milk as a result of the natural process of cell turnover and repair, although their number increases towards the end of lactation or after mastitis-related inflammation.[1,2] Additionally, the number of leukocytes increases, especially in case of mastitis-related infections or trauma. Leukocytes are immune cells that combat invading organisms. The ratio of epithelial cells to SCs varies between 35% and 70%; in normal milk, epithelial cells typically constitute 65–70 % of SCs.[1] Mastitis is an infectious disease characterized by an increased number of SCs.[3] In mastitis, the number of leukocytes in the milk increases and the proportion of epithelial cells decreases. Leukocytes are therefore a more important factor in the assessment of SCC. SCC is widely used for evaluating milk quality.[4] According to the Turkish Food Codex "Raw Milk and Heat-Processed Drinking Milk Communiqué," the maximum number of somatic cells in raw cow milk should be 500,000 per ml. Elevated SCC in milk is associated with mastitis however current knowledge on the relationship between milk quality and SCC is limited.[5]

Yogurt is the most widely consumed dairy product and is made by fermenting milk with *Streptococcus thermophilus* and *Lactobacillus delbrueckii* subsp. *bulgaricus*. These two bacteria are lactic acid bacteria and are famous for their antimicrobial, antiviral and immunomodulatory properties and play a role in the treatment of many gastrointestinal diseases.[6–8] Possible health benefits of regular yogurt consumption include lowering cholesterol levels, aiding digestion, reducing weight gain, reducing gastrointestinal infections and risk of colon cancer, as well as preventing obesity, strengthening the immune system, preventing diabetes, promoting calcium absorption, and eliminating symptoms of lactose intolerance.[9–11]

Current knowledge of the relationship between elevated SCC in milk and the physicochemical quality, color characteristics and shelf life of yogurt is limited. The aim of the present study was to investigate the relationship between different SCC values in milk and yogurt quality. The study was formulated as plain yogurt. In the study, yogurts were produced from milk samples with three different SCC values, and an investigation was conducted into their physicochemical, textural and color properties.

Received 26.02.2025
Revised 07.04.2025
Accepted 07.05.2025
Publication Date 24.06.2025

Corresponding author:
Tamer TURGUT
E-mail:
tturgut@atauni.edu.tr

Cite this article: Turgut T., Diler A. Investigation of the physicochemical and textural properties of yogurt made from milk with different somatic cell count. *NanoEra*. 2025;5(1):9-15

METHODS

Materials

The raw milk used in the study came from the herd at the Atatürk University Food and Livestock Application Centre. The cows were in the middle lactation and showed no clinical signs of mastitis. The analysis of milk batches from cows was conducted using a DeLaval cell counter (DeLaval International, Sweden). This device was used for the precise measurement of SCC value in milk. The raw milk samples were collected in three groups according to the SCC status: low SCC value (LSCC, < 100,000 cells/ml), medium SCC value (MSCC, 100,000 – 500,000 cells/ml) and high SCC value (HSCC, > 500,000 cells/ml). Commercial yogurt culture, YC-381, containing *S. thermophilus* and *L. bulgaricus* was purchased from Chr. Hansen (Hørsholm, Denmark). The cultures were freeze-dried and inoculated according to the manufacturer's recommendations.

Manufacture of Yogurts

Each batch of milk sample (2.5 L, per SCC value) was standardised by evaporation to 11 % non-fat milk solids. The standardised batches were heated to 90°C for 10 minutes and cooled to 43 ± 1 °C for the incubation phase. To inoculate the milk with the starter culture according to the manufacturer's recommendations, half of the sachet containing 50 units of starter culture YC-381 (Chr. Hansen, Denmark) was dissolved in 250 ml of sterilised milk and 12 ml was used to inoculate each 2.5 l batch. The inoculated milk was filled into sterile 170-ml glass jars and left at 43 ± 1°C for a final fermentation. The yogurt groups were coded according to the three different SCC values they contained: low SCC value (LCY), medium SCC value (MCY) and high SCC value (HCY). Fermentation was terminated when pH 4.5 was reached. After fermentation, the yogurt batches were transferred to a refrigerator at a temperature of 4 ± 1°C and kept and stored at this temperature. Each group consisted of 15 jars of yogurt and weekly samples were taken from different jars for physicochemical, microbiological and textural analysis.

Physicochemical analyses

The yogurt samples were analysed 24 hours after production and after storage for 7, 14, 21 and 28 days. DM and fat content were determined according to AOAC by the drying method and the Gerber method, respectively.[12] The pH was measured using a digital benchtop pH meter (pH 211, Hanna Instruments, Portugal). The TA and pH were determined according to Kurt et al.[13]. The TA was determined after mixing 10 g yogurt with the same volume of distilled water and titrating it with 0.1 N NaOH. The TA is calculated by the following formula 1.

$$\text{TA}\ (\%) = \frac{V(ml) * 0.009}{m} x100 \qquad (1)$$

V is the volume of 0.1 NaOH spent in the titration and m is the mass of the sample.

Syneresis is the separation of the whey phase from the yogurt, and WHC is the term for its retention. The syneresis of analysed yogurts was determined according to the drainage method described by Turgut and Diler.[11] For syneresis, 25 g of the sample was weighed and filtered through filter paper (Whatman No 1, UK) for 2 h at 4°C. The syneresis values were calculated using the following formula 2.

$$\text{Syneresis}\ (\%) = \frac{\text{Whey volume}}{\text{İnitial volume}} \times 100 \qquad (2)$$

For water holding capacity, a 10 g sample was weighed and centrifuged (4500×g, 30 min at 4°C). The WHC was calculated using the following formula 3.

$$\text{WHC}\ (\%) = [1 - \frac{\text{Whey weigh}}{\text{initial weight}}] * 100 \qquad (3)$$

Colorimetric Analysis

The color parameters were measured with a colorimeter (PCE XXM-20, PCE GmbH, Germany) and LED lighting at a viewing angle of 45°. The results were expressed as L* a* b* values using the CIELAB color system (L*a*b* color space). L* value indicates lightness and is expressed on a vertical axis with values from 0 to 100. The value zero means completely black, i.e., no light transmission, while 100 is completely white. The a* and b* values are chromaticity coordinates and characterize a point in the three-dimensional color space in which the colors flow from the red axis (a*) to the yellow axis (b*) and from the green axis (–a*) to the blue axis (-b*).[14] The chroma C* value stands for the clarity or saturation of the color. The line obtained by connecting the coordinate centre of the axes to a point in space is called chroma C*. ΔE is used to express the range of difference between the current color and the ideal whiteness. The ΔE and chroma C were calculated in the CIELCh color space using the following equations.[15]

$$(\Delta E) = \sqrt{(\Delta L^*)^2 + (\Delta a^*)^2 + (\Delta b^*)^2} \qquad (4)$$

$$C^* = \sqrt{(a^*)^2 + (b^*)^2} \qquad (5)$$

$\Delta L = L_i - L_0$. The i stands for the observed value for each storage time and the index 0 for the references used. In the study, we have the color parameters of the white standard (L: 100)

Texture Analysis

Texture is a general term and encompasses the physical properties of the product that can be perceived by the human senses.[16] Texture properties were determined on the 1st, 7th, 14th, 21st and 28th day of storage using the TA-XTPlus Texture Analyzer (Stable Micro System, Surrey, UK) calibrated with a 500 g load cell and equipped with a cylindrical P/25P probe (Ø25 mm, perspex). The pre-test temperature of the yogurt samples was approximately 10°C. The penetration depth was set at 30 mm and the constant test speed of the probe was set at 1 mm/s during the compression and relaxation cycle.[17] Instrumental texture profile analysis (TPA) was used to determine texture parameters such as hardness, adhesiveness, cohesiveness, gumminess and resilience. Instrumental TPA analysis is the quantification of texture properties obtained from areas under

force or force-time curves. TPA analysis is the quantification of tissue features obtained from areas under force or force-time curves. Hardness corresponds to the maximum force (N) in the first compression cycle in the TPA diagram and is used instead of firmness. Adhesiveness refers to the force required to overcome the adhesion between the probe and samples. Cohesiveness is defined as the internal stickiness of the samples. Gumminess is a textural characteristic of semi-solid foods that have low hardness and high cohesion. Force-time diagrams were plotted for these three texture parameters and the areas under the curves were determined using Exponent (4.0.9.0) software. All measurements were performed in two replicates.

Statistical Analysis

The results of the analyses on days 1, 7, 14, 21, and 28 were evaluated using univariate statistical analyses. All analyses were performed twice. The data obtained from the study were compared by Duncan's multiple range tests ($P < .05$) using SPSS 20.0 (IBM SPSS Corp., Armonk, NY, USA) software for Windows.

RESULTS and DISCUSSION

Measurement of pH and Titratable Acidity (TA)

Table 1 summarizes some physicochemical analysis results of the yogurt varieties produced from milk with different SCC values. The effect of storage time on pH and TA values was significant ($P < .05$). The TA value of the yogurt samples ranged between 1.164 % and 1.273 %. The lowest TA value was on day 1 and the highest was on day 28. The mean pH value, which was 4.28 at the beginning of storage, decreased to 4.19 on day 28. After day 21, however, the differences between the mean values were statistically significant ($P < .05$). The increase in the acidity of the yogurt samples during storage is due to the post-acidification process in which the yogurt bacteria become active during the storage period. Donkor et al.[18] reported that yogurt cultures are responsible for the decrease in pH and increase in the acidity of yogurt during storage. Najaf Najafi et al.[19] reported that the effect of SCC on the TA or pH of yogurt was significant ($P < .05$) after 7 days. The TA values in the study were higher than the results of Fernandes et al.[20].

The influence of the SCCs on the pH and TA was found to be significant ($P < .01$). Yogurts made from milk with high SCC content had higher pH values and lower TA values (Table 1). The mean TA values of the yogurts ranged from 1.172 % to 1.337 %. The lowest TA value was determined in MCY yogurt, while the highest was observed in LCY yogurt. Fernandes et al.[20] reported that high SCC content in milk had no significant effect on the acidity or pH of yogurt during storage. Vivar-Quintana et al.[21] reported that the pH of yogurt made from milk with high SCC content was significantly lower than the pH of yogurt made from milk with low SCC content. The mean pH of the yogurts ranged from 4.17 (LCY yogurt) to 4.28 (HCY yogurt). Fernandes et al. [20] reported that the TA values of yogurts made from milk with different SCC content ranged from 0.7% to 0.74%. In the present study, the TA values were found higher than these reported results. At the end of storage, the pH and TA values of HCY and MCY yogurts were statistically different ($P < .01$) from those of LCY yogurts. The SCC value had no significant influence on the pH of the yogurts up to day 7. The pH of yogurts in the study was lower than the results of Fernandes et al.[20].

Syneresis, Water Holding Capacity (WHC)

Syneresis is the separation of serum from the structure of yogurt and is considered a quality parameter for yogurt.[22] The influence of the storage period on the syneresis values was significant ($P < .05$).

Table 1. The changes in physicochemical characteristics of yogurt samples during storage

		Total Solids $\bar{x} \pm SD$	Fat $\bar{x} \pm SD$	Syneresis $\bar{x} \pm SD$	WHC $\bar{x} \pm SD$	LA $\bar{x} \pm SD$	pH $\bar{x} \pm SD$
Yogurt samples							
LCY		14.36 ± 0.533	3.92 ± 0.556	30.14 ± 3.307^{ab}	52.14 ± 4.834	1.337 ± 0.062^{a}	4.17 ± 0.056^{a}
MCY		14.92 ± 0.537	4.28 ± 0.553	27.94 ± 3.327^{a}	50.03 ± 4.834	1.172 ± 0.061^{b}	4.24 ± 0.055^{b}
HCY		14.66 ± 0.546	4.096 ± 0.570	32.41 ± 3.388^{b}	50.61 ± 4.954	1.181 ± 0.063^{b}	4.28 ± 0.057^{b}
Storage time (days)							
1		14.72 ± 0.536	3.79 ± 0.559	29.95 ± 3.323^{a}	46.90 ± 4.858^{a}	1.160 ± 0.062^{a}	4.28 ± 0.056^{a}
7		14.74 ± 0.540	4.16 ± 0.556	30.63 ± 3.333^{a}	58.82 ± 4.858^{b}	1.195 ± 0.061^{ab}	4.26 ± 0.056^{a}
14		14.63 ± 0.546	4.39 ± 0.553	30.75 ± 3.326^{ab}	49.57 ± 4.858^{a}	1.228 ± 0.062^{abc}	4.24 ± 0.054^{ab}
21		14.77 ± 0.538	4.02 ± 0.559	27.65 ± 3.343^{b}	49.21 ± 4.858^{a}	1.255 ± 0.063^{bc}	4.22 ± 0.056^{ab}
28		14.38 ± 0.543	4.13 ± 0.557	33.43 ± 3.323^{a}	52.28 ± 4.858^{ab}	1.273 ± 0.061^{c}	4.19 ± 0.056^{c}
Source	**D.F**						
SCC value	2	NS	NS	**	NS	**	**
Storage time	4	NS	NS	*	*	*	*
Error	27						
Total	34						

LCY= low SCC value; MCY= medium SCC value; HCY= high SCC value

^{a,b,c} means in the same column without a common superscript different ($P < .05$).

* is significant at 0.05; ** is significant at 0.01 probability levels; NS: not significant

The syneresis values ranged from 27.65% to 33.43%, with a decrease observed during the storage period. The lowest syneresis value was on day 21, and differences between the means were not statistically significant until day 28 ($P > .05$). The SCC content of the milk significantly affected the syneresis values of the yogurt varieties ($P < .01$). The yogurt produced from milk with medium SCC had the lower ($P < .01$) syneresis values than high SCC yogurt. The highest syneresis value was found in HCY yogurt (32.41%), this result indicates that the consistency of the HCY yogurt is weak or the gel is unstable. The syneresis values of HCY yogurt were not statistically different from LCY yogurt, but were significantly different from MCY yogurt ($P < .01$). Vivar-Quintana et al.[21] also reported similar results for yogurts produced from milk with high SCC content.

The influence of storage time on WHC values was significant ($P < .05$). The lowest WHC value was found on day 1, and WHC values increased a little after that, but the differences between the means were not significant after day 7 ($P > .05$). The WHC values of the yogurt varieties ranged from 50.03% to 52.14%. The WHC values of the yogurts made from milk with medium and high SCC content were lower than those of the LCY yogurts (Table 1). As the SCC content of the milk increased, the WHC value decreased, but the differences were not significant ($P > .05$). The MCY yogurt had the lowest WHC value, followed by the HCY yogurt. The WHC values in the study were similar to the results of Bakırcı et al.[23].

Color analysis

Color is one of the first characteristics perceived by the human senses. It is an important factor for the quality of yogurt and thus influences its acceptance[24] The color parameters of the yogurt varieties are shown in Table 2. The L* value, which expresses the lightness, was between 84.51 and 85.42 for all yogurt varieties. The L* values were very close to each other. The influences of SCC content and storage time on the L* values were not significant ($P > .05$). The highest L* value was found on day 1, and it was found that L* values decreased on the following days of storage. This result is consistent with the findings of Nguyen and Hwang et al.[25], who reported that the L* values of yogurts decrease during storage. Scibisz et al.[24] stated that L* values increased during storage of fruit yogurts.

The a* value, which expresses the redness/greenness, ranged between -32.49 and -38.51 for the yogurt varieties. Yogurts made from milk with high SCC content had lower a* values. The highest a* value was found for MCY yogurt and the lowest value for LCY yogurt. However, the differences between the mean values were not significant ($P > .05$). A general decrease in a* values was observed during the storage period. All yogurt varieties showed the loss of redness during storage by the change in a* values. This result is consistent with the findings of Scibisz et al.[24]. The influence of the SCC content was found to be significant only on the b* values ($P < .01$). Yogurts made from milk with the highest SCC content had the lowest b* values (Table 2). The b* value, which expresses yellowness, ranged from 7.83 to 9.68 for the yogurt varieties. The influence of the storage period on the b* values was significant ($P < .05$). The b* values ranged from 7.22 to 9.23 with a small decrease observed during the storage period. The lowest b* value was on day 28, but differences between the mean values were not important until day 28 ($P < .05$). The C* value, which expresses the saturation of color, was between 34.11 and 39.58 for the yogurt varieties. The C* values increased significantly ($P < .05$) during storage, indicating that the color became more vivid. The increase in the C* value is consistent with the increase in acidity of the yogurt during storage.

Textural Analysis

Textural properties are significant indicators of the yogurt quality.[16] The changes in TPA parameters (such as hardness, adhesiveness, cohesiveness, springiness) during storage are shown in Table 3.

Table 2. The color properties of the yogurt samples during storage

		L* $\bar{x} \pm SD$	a* $\bar{x} \pm SD$	b* $\bar{x} \pm SD$	ΔE $\bar{x} \pm SD$	C* $\bar{x} \pm SD$
Yogurt samples						
LCY		84.51 ± 4.449	-38.51 ± 6.963	8.60 ± 1.128^{a}	42.53 ± 7.566	39.58 ± 6.542
MCY		85.40 ± 4.456	-32.49 ± 6.973	9.68 ± 1.126^{b}	37.32 ± 7.566	34.11 ± 6.545
HCY		85.42 ± 4.559	-34.38 ± 7.135	7.83 ± 1.155^{a}	38.23 ± 7.753	35.31 ± 6.703
Storage time (days)						
1		87.81 ± 4.461	-29.03 ± 6.998^{a}	9.07 ± 1.133^{a}	32.99 ± 7.604^{a}	30.59 ± 6.574^{a}
7		84.05 ± 4.471	-37.11 ± 6.987^{ab}	9.23 ± 1.130^{a}	41.51 ± 7.602^{ab}	38.29 ± 6.576^{ab}
14		86.98 ± 4.473	-32.53 ± 6.978^{ab}	8.92 ± 1.132^{a}	36.39 ± 7.604^{ab}	33.96 ± 6.572^{ab}
21		83.46 ± 4.468	-36.28 ± 6.967^{ab}	8.46 ± 1.129^{a}	41.09 ± 7.606^{ab}	37.28 ± 6.578^{ab}
28		83.47 ± 4.470	-40.15 ± 6.989^{b}	7.22 ± 1.130^{b}	44.05 ± 7.601^{b}	40.81 ± 6.573^{b}
Source	**D.F**					
SCC value	2	NS	NS	**	NS	NS
Storage time	4	NS	*	**	*	*
Error	27					
Total	34					

LCY= low SCC value; MCY= medium SCC value; HCY= high SCC value

^{a,b,c} means in the same column without a common superscript different ($P < .05$).

* is significant at 0.05, ** is significant at 0.01 probability levels, NS: not significant

Table 3. The textural properties of yogurt samples during storage

		Hardness $\bar{x} \pm SD$	Adhesiveness $\bar{x} \pm SD$	Springiness $\bar{x} \pm SD$	Cohesiveness $\bar{x} \pm SD$	Gumminess $\bar{x} \pm SD$	Resilience $\bar{x} \pm SD$
Yogurt samples							
LCY		25.20 ± 1.878[a]	-48.20 ± 12.079[a]	0.96 ± 0.011	0.83 ± 0.025[a]	21.002 ± 1.619[a]	0.17 ± 0.053[a]
MCY		25.14 ± 1.876[a]	-47.39 ± 12.077[a]	0.96 ± 0.012	0.83 ± 0.025[a]	20.89 ± 1.616[a]	0.16 ± 0.052[a]
HCY		22.16 ± 1.925[b]	-25.90 ± 12.377[b]	0.97 ± 0.010	0.86 ± 0.026[b]	19.560 ± 1.658[b]	0.23 ± 0.054[b]
Storage time (days)							
1		21.88 ± 1.887[a]	-28.62 ± 12.139[a]	0.97 ± 0.012	0.82 ± 0.025[a]	18.398 ± 1.627[a]	0.21 ± 0.063[a]
7		24.03 ± 1.878[ab]	-31.03 ± 12.130[a]	0.97 ± 0.010	0.86 ± 0.025[b]	21.011 ± 1.627[b]	0.23 ± 0.062[a]
14		22.46 ± 1.882[ab]	-33.87 ± 12.139[a]	0.96 ± 0.011	0.83 ± 0.025[a]	18.984 ± 1.627[a]	0.19 ± 0.060[ab]
21		24.38 ± 1.880[ab]	-41.88 ± 12.134[a]	0.97 ± 0.012	0.86 ± 0.025[b]	21.314 ± 1.627[b]	0.20 ± 0.061[ab]
28		26.64 ± 1.877[b]	-56.66 ± 12.136[b]	0.96 ± 0.011	0.84 ± 0.025[ab]	22.707 ± 1.627[b]	0.14 ± 0.062[b]
Source	**D.F**						
SCC content	2	**	**	NS	*	*	**
Storage time	4	**	**	NS	*	**	*
Error	27						
Total	34						

LCY= low SCC value; MCY= medium SCC value; HCY= high SCC value

[a,b,c] means in the same column without a common superscript different ($P < .05$).

* is significant at 0.05, ** is significant at 0.01 probability levels, NS: not significant

The hardness and adhesiveness increased during storage and the differences between the mean values were significant ($P < .05$). The lowest hardness value was found on day 1, and the hardness of yogurts increased inversely to the syneresis values on the following days of storage. Hardness is the most important parameter for evaluating yogurt texture and is regarded as a measure of yogurt firmness.[26] The hardness values ranged from 22.16 to 25.20, depending on the SCC values. The yogurt made from milk with a high SCC had the lowest hardness values. The lowest hardness value was found in HCY yogurt. This result indicates that the consistency of the HCY yogurt is weak or the gel firmness is not very strong. The decrease in hardness values associated with the increase in SCC content was statistically consistent. The hardness values in the study were lower than the results of Mudgil et al.[27] and Kose et al.[26].

Adhesiveness refers to the strength required to overcome the attractive forces between the surface of the food and the surface of the material in contact with it (probe). The lowest hardness value (-28.62) was found on day 1, and the highest value (-56.66) was found on the last day of storage. The SCC content of the milk significantly affected the adhesiveness value of the yogurt varieties ($P < .05$). The mean adhesiveness value of the yogurt varieties ranged from -25.90 to -48.20, depending on SCC values of milk. The yogurt made from milk with the highest SCC content had the lowest adhesiveness value. The adhesiveness value of LCY yogurt was not significantly different from MCY yogurt but was significantly different from that of HCY yogurt ($P < .01$). Yogurt made from milk with high SCC had the lowest hardness and adhesiveness, while the highest values for hardness were observed in LCY yogurt. The adhesiveness values we found are consistent with the findings of Mudgil et al.[27]. Cohesiveness refers to the force required to overcome the internal stickiness caused by the structure of the food. The storage time had a significant effect on the cohesiveness values of the yogurts ($P < .05$). The lowest cohesiveness value (0.82) was found on day 1 and the highest value (0.86) on day 7. The SCC content of the milk significantly affected the cohesiveness values of the yogurt varieties ($P < .05$). The cohesiveness value of yogurts ranged from 0.82 to 0.86, depending on the different SCC values. The yogurt made from milk with a medium SCC value had the lowest cohesiveness values. The cohesiveness values of the MCY yogurt were not statistically different from those of the LCY yogurt but were significantly ($P < .01$) different from those of the HCY yogurt. It is possible that yogurts with high adhesiveness and low cohesiveness values would stick to the probe during the test. However, since the cohesiveness values were low, there was no sticking to the probe. In the present study, the cohesiveness values were higher than the findings of Domalaga et al.[16].

CONCLUSION

The results showed that the effects of different SCC levels in the milk on the physicochemical and textural properties of the yogurts were important. The pH, TA and syneresis values of the yogurt varieties are significantly influenced by the SCC value of the milk. In contrast, the WHC value was not significantly affected by the SCC of the milk. With increasing SCC content in the milk, the pH of the yogurt varieties increased and the TA values decreased during storage. A high SCC content of the milk led to a significant reduction in the stability of the yogurt and the serum retention capacity.

It was found that the color parameters (L* a* C*) were not significantly affected by the SCC value of the milk. Increasing the SCC value of the milk above 500,000 cells/ml had no significant effect on the L*, a* and C* values of the yogurts. The SCC value of the milk of more than 500,000 cells/ml had a significant negative effect on the texture parameters of the yogurts. A high

SCC value of the milk led to a significant reduction in the hardness and adhesiveness value of the yogurt. Yogurt from milk with the highest SCC value showed the lowest values for hardness and adhesiveness, while the highest values were observed in LCY yogurt. Based on these results, we can say that the SCC in cow's milk for yogurt production should not exceed 500,000 cells/ml, especially with regard to texture quality.

Peer-review: Externally peer-reviewed.

Author Contributions: All authors contributed to the study conception. T.T. and A.D. conceived and designed the study. T.T. and A.D. set up the laboratory study. T.T. wrote the manuscript. A.D. made the statistical analysis. All authors contributed to the critical revision of the manuscript. The final version of the manuscript was approved by all authors.

Conflict of Interest: The authors have no conflicts of interest to declare.

Financial Disclosure: The authors declared that this study has received no financial support

REFERENCES

1. Sharma N, Singh NK, Bhadwal MS. Relationship of Somatic Cell Count and Mastitis: An Overview. *Asian-Australasian J Anim Sci*. 2011;24(3):429-438. doi:10.5713/ajas.2011.10233
2. Vašíček J, Tvarožková K, Uhrinčať M, Mačuhová L, Hleba L, Tančin V. Distribution of leucocytes and epithelial cells in sheep milk in relation to the somatic cell count and bacterial occurrence: A preliminary study. *Slovak J Anim Sci*. 2019;52(04):160-165.
3. Oliveira CAF, Fernandes AM, Neto OCC, Fonseca LFL. Composition and sensory evaluation of whole yogurt produced from milk with different somatic cell counts. *Aust J Dairy Technol*. 2002;57(3):192.
4. Abed AH, Menshawy AMS, Zeinhom MMA, et al. Subclinical Mastitis in Selected Bovine Dairy Herds in North Upper Egypt: Assessment of Prevalence, Causative Bacterial Pathogens, Antimicrobial Resistance and Virulence-Associated Genes. *Microorganisms*. 2021;9(6):1175. doi:10.3390/microorganisms9061175
5. Kodeksi TG. *Çiğ Süt ve Isıl Işlem Görmüş Içme Sütleri Tebliği*. Resmi Gazete 14, 2000/6, 23964 (2000).
6. Ashraf R, Shah NP. Selective and differential enumerations of Lactobacillus delbrueckii subsp. bulgaricus, Streptococcus thermophilus, Lactobacillus acidophilus, Lactobacillus casei and Bifidobacterium spp. in yoghurt — A review. *Int J Food Microbiol*. 2011;149(3):194-208. doi:10.1016/j.ijfoodmicro.2011.07.008
7. Dan T, Hu H, Tian J, He B, Tai J, He Y. Influence of Different Ratios of Lactobacillus delbrueckii subsp. bulgaricus and Streptococcus thermophilus on Fermentation Characteristics of Yogurt. *Molecules*. 2023;28(5):2123. doi:10.3390/molecules28052123
8. Savaiano DA, Hutkins RW. Yogurt, cultured fermented milk, and health: a systematic review. *Nutr Rev*. 2021;79(5):599-614. doi:10.1093/nutrit/nuaa013
9. Guarner F, Perdigon G, Corthier G, Salminen S, Koletzko B, Morelli L. Should yoghurt cultures be considered probiotic? *Br J Nutr*. 2005;93(6):783-786. doi:10.1079/BJN20051428
10. Aktaş H, Yıldız S, Çetin B. Probiotic and technological properties of isolates from homemade and industrial yoghurts. *J Food Process Preserv*. 2022;46(11):e17135. doi:10.1111/jfpp.17135
11. Turgut T, Diler A. The effect of Coriandrum sativum L. on yogurt: a comprehensive study of physicochemical, microbiological, sensory, and textural properties. *Front Nutr*. 2025;11. doi:10.3389/fnut.2024.1493602
12. Chemists A. *Methods of Analysis of AOAC International*. 16th ed. AOAC Washington, DC, USA; 2004.
13. Kurt A, Çakmakçı S, Çağlar A. *A Guide Book of Analysis Methods of Milk and Milk Products.* Ataturk University; 2007.
14. Chudy S, Bilska A, Kowalski R, Teichert J. Colour of milk and milk products in CIE L*a*b* space. *Med Weter*. 2020;76(01):6327-2020. doi:10.21521/mw.6327
15. Milovanovic B, Djekic I, Miocinovic J, et al. What Is the Color of Milk and Dairy Products and How Is It Measured? *Foods*. 2020;9(11):1629. doi:10.3390/foods9111629
16. Domagała J. Instrumental Texture, Syneresis and Microstructure of Yoghurts Prepared from Goat, Cow and Sheep Milk. *Int J Food Prop*. 2009;12(3):605-615. doi:10.1080/10942910801992934
17. Kumar P, Mishra HN. Effect of mango pulp and soymilk fortification on the texture profile of set yoghurt made from buffalo milk. *J Texture Stud*. 2003;34(3):249-269. doi:10.1111/j.1745-4603.2003.tb01060.x
18. Donkor ON, Henriksson A, Vasiljevic T, Shah NP. Effect of acidification on the activity of probiotics in yoghurt during cold storage. *Int Dairy J*. 2006;16(10):1181-1189. doi:10.1016/j.idairyj.2005.10.008
19. Najaf Najafi M, Koocheki A, Valibaigy S. Effects of somatic cell counts on the physicochemical and rheological properties of yoghurt made from sheep's milk. *Int J Food Sci Technol*. 2010;45(4):713-718. doi:10.1111/j.1365-2621.2010.02185.x
20. Fernandes AM, Oliveira CAF, Lima CG. Effects of somatic cell counts in milk on physical and chemical characteristics of yoghurt. *Int Dairy J*. 2007;17(2):111-115. doi:10.1016/j.idairyj.2006.02.005
21. Vivar-Quintana AM, Beneitez De La Mano E, Revilla I. Relationship between somatic cell counts and the properties of yoghurt made from ewes' milk. *Int Dairy J*. 2006;16(3):262-267. doi:10.1016/j.idairyj.2005.03.006
22. Gyawali R, Ibrahim SA. Effects of hydrocolloids and processing conditions on acid whey production with reference to Greek yogurt. *Trends Food Sci Technol*. 2016;56:61-76. doi:10.1016/j.tifs.2016.07.013
23. Bakirci S, Dagdemir E, Boran OS, Hayaloglu AA. The effect of pumpkin fibre on quality and storage stability of reduced-fat set-type yogurt. *Int J Food Sci Technol*. 2017;52(1):180-187. doi:10.1111/ijfs.13264
24. Ścibisz I, Ziarno M, Mitek M. Color stability of fruit yogurt

during storage. *J Food Sci Technol*. 2019;56(4):1997-2009. doi:10.1007/s13197-019-03668-y

25. Nguyen L, Hwang E-S. Quality Characteristics and Antioxidant Activity of Yogurt Supplemented with Aronia (Aronia melanocarpa) Juice. *Prev Nutr Food Sci*. 2016;21(4):330-337. doi:10.3746/pnf.2016.21.4.330
26. Kose YE, Altun I, Kose S. Determination of Texture Profile Analysis of Yogurt Produced By Industrial and Traditional Method. *Int J Sci Technol Res*. 2018;4(8):66-70.
27. Mudgil D, Barak S, Khatkar BS. Texture profile analysis of yogurt as influenced by partially hydrolyzed guar gum and process variables. *J Food Sci Technol*. 2017;54(12):3810-3817. doi:10.1007/s13197-017-2779-1

ATATÜRK ÜNİVERSİTESİ YAYINLARI
ATATURK UNIVERSITY PUBLICATIONS

Research Article DOI: 10.5281/zenodo.15729095

Dynamic thermal cycle ambient simulation under mouth motion; a finite element analysis

Efe Çetin YILMAZ[1]

[1] Department of Control Systems, Engineering and Architecture Faculty, Kilis 7 Aralık University, Kilis, Türkiye

ABSTRACT

The aim of this study is to analyze the experimentally established thermal cycle test experiment using the Finite Element Analysis (FEA) method. Within the scope of this study, the thermal-mechanical behavior of the pure titanium test material at minimum and maximum temperature environments was analyzed in the simulation environment occurred at 1/1 scale with the experimentally established parameters. Pure titanium test materials that different geometry were kept at 5°C temperature for 30 seconds and then exposed to 65°C environment during 2 seconds change period. Thus, 1 thermal cycle was completed under mouth motion simulation. The results obtained showed that the temperature distribution in the circular test sample exhibited a more homogeneous distribution behavior than the square test sample. This result reveals the importance of the geometric structure of the test sample in the experimental environment conditions. Therefore, the use of a circular test sample in *in vitro* laboratory thermal cycling experiments will increase the accuracy of the results obtained under mouth motion simulation tests. As a result, the results obtained in this study are expected to mathematically guide the selected parameters in *in vitro* and *in vivo* studies.

Keywords: Mouth motion thermal simulation, Biomaterials, Finite Element Analysis.

INTRODUCTION

In recent years, titanium and titanium alloys have been preferred as biomaterials in the living body due to their superior mechanical and biocompatibility behavior. It has been reported in the literature that titanium alloys can be preferred in the treatment process due to their superior behavior such as high strength-to-weight ratio, good fatigue resistance, relatively low Young's modulus, good biocompatibility, and high corrosion resistance.[1] However, biomaterials placed in the human body can be exposed to various wear mechanisms. It has been reported in the literature that titanium and its alloys do not have sufficient wear resistance.[2] Finite Element Analysis remains an essential method for initial screening of biomaterial behavior. Thermal cycling is one of the most preferred test methods to simulate the life cycle of biomaterials implanted in the body.[3] In thermal cycle tests, the mechanical, aesthetic and chemical behaviors of biomaterials in the body can be predicted during the time they remain in the body. Researchers are trying to predict the mechanical behavior of biomaterials by using thermal cycling test experiments with *in vivo*, *in vitro* and finite element analysis testing simulation methods. These test methods may have many advantages and disadvantages compared to each other. For example, while the *in vivo* test method takes a very long time, the *in vitro* and finite element analysis test methods can be completed in shorter time periods. However, the ability to mimic living structures when creating test method mechanisms can significantly affect the accuracy and validity of test results. In the literature, many researchers have tried to determine the mechanical, chemical and aesthetic behaviors of biomaterials with *in vitro* wear and test methods and wear test mechanisms.[4–7] The concept of thermal cycling has been used effectively in the literature for approximately 70 years.[8] This process is basically based on the heating and cooling process of a material placed in the tooth or body throughout its life cycle.[8] The environment to which teeth and dental materials are exposed while biting into an ice cream after drinking a hot coffee can be given as an example on living tissue. This system has traditionally been used to simulate *in vivo* aging of restorative materials by subjecting them to repeated cyclic hot and cold temperatures in a water bath to reproduce the thermal changes that occur in the oral cavity.[8] In thermal cycling tests performed in the laboratory, it is very important to select minimum and maximum temperatures. Table 1 gives examples of the temperatures of the absorbed fluids and the resulting average minimum and maximum tooth surface temperatures.[9] This study evaluates the effect of temperature changes occurring in the human oral environment on sat titanium biomaterial with different geometries using the finite element analysis test method under mouth motion simulation. As a result, the results obtained in this study are expected to mathematically guide the selected parameters in *in vitro* and *in vivo* studies.

Received 26.11.2024
Revised 06.01.2025
Accepted 13.02.2025
Publication Date 24.06.2025

Corresponding author:
Efe Çetin YILMAZ
E-mail:
efecetinyilmaz@msn.com

Cite this article: Yılmaz EÇ. Dynamic thermal cycle ambient simulation under mouth motion; a finite element analysis. *NanoEra*. 2025;5(1):16-21

Table 1. Examples of the temperatures of the absorbed fluids and the resulting average minimum and maximum tooth surface temperatures [9]

Location	Volume drunk (mL)	Hot liquid temp. (°C)	Max. tooth temp. (°C)	Cold liquid temp. (°C)	Min. tooth temp. (°C)
Incisor labial	-	60	45	0	15
Incisol palatal	-	< 61	58.5	-	-
Molar occlusal	-	< 61	53.1	0	1.0
	-	63.5	53.5	-	-
	-	58	50	-	-
	-	55	47	-	-
Molar palatal	-	60	48.5	-	-
	30	60	44.86	0	21.63

METHOD

In this study, ANSYS 19 academic version program was preferred for thermal cycle simulation tests of pure titanium material. For this reason, the mesh amount is set to a maximum of 30,000 which this ratio is in a range of values sufficient for the analysis performed finite element thermal test analyses. Pure titanium material was designed as square and cylindrical samples on the Space Claim designer software. The ideal ambient properties of pure titanium and test specimens are shown in Figure 1.

Properties of Outline Row 14: Titanium Alloy

	A	B	C
1	Property	Value	Unit
2	Density	4620	kg m^-3
3	Isotropic Secant Coefficient of Thermal Expansion		
4	Coefficient of Thermal Expansion	9,4E-06	C^-1
5	Isotropic Elasticity		
6	Derive from	Young's M...	
7	Young's Modulus	9,6E+10	Pa
8	Poisson's Ratio	0,36	
9	Bulk Modulus	1,1429E+11	Pa
10	Shear Modulus	3,5294E+10	Pa
11	Tensile Yield Strength	9,3E+08	Pa
12	Compressive Yield Strength	9,3E+08	Pa
13	Tensile Ultimate Strength	1,07E+09	Pa
14	Compressive Ultimate Strength	0	Pa

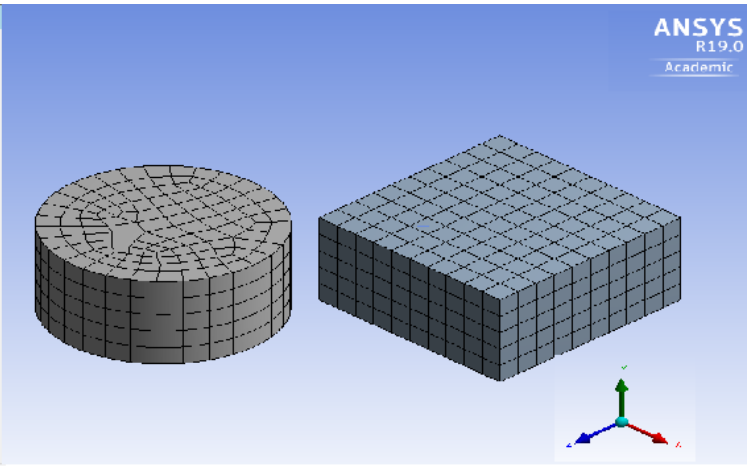

Figure 1. The ideal ambient properties of pure titanium and test specimens

The thermal cycle environment experimental studying environment was simulated on a 1/1 scale and designed as 5°C lower limit, 65°C upper limit, 30 seconds waiting period and 2 seconds thermal change period. Figure 2 shows the dynamic thermal cycling test simulation environment. Test specimen with different geometries were placed in the specimen holder shown in Figure 2 and fixed along the geometry expect for thermal surface to simulate the experimental environment. Thus, the geometric change of the test sample due to the temperature difference was controlled through thermal cycle simulation tests. The test mechanism was given to the 65°C fluid medium from the hot water inlet as a first step and waited for 30 seconds. As a second step, the hot water 5°C fluid was thrown into the hot water tank from the fluid outlet and sent to the cold water test environment. This process took about 2 seconds experimentally. The test sample was kept in the cold water environment for 30 seconds and sent to the cold tank from the water outlet in this environment. This process also took about 2 seconds experimentally. Thus, 1 thermal cycle took about 64 seconds experimentally. In the control experimental structure of this process, the programmable logic controller (PLC) was used to control the fluids with solenoid valves. Briefly, the method of activating solenoid valves using a time-delay control structure was used through thermal cycle test simulation. In future studies, this process will be made more sensitive by taking real-time temperature measurements on the test specimen. Thus, the heat absorption rates of different materials will be taken into account in the test structure.

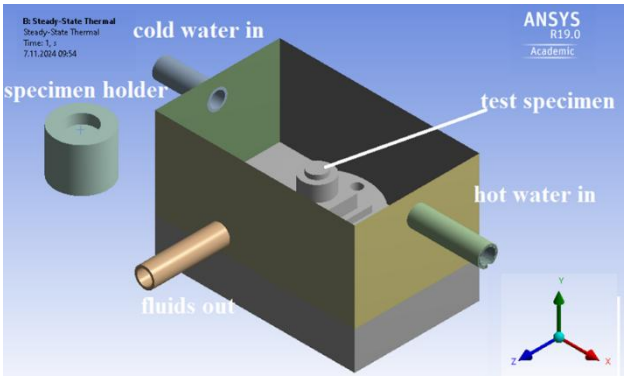

Figure 2. Dynamic thermal cycling test simulation environment based real-time PLC Control.

RESULTS

In this study, the finite element analysis simulation of the thermal cycle test experiment with real-time control structure was carried out through mouth motion. The 65°C distilled fluid was passed through the test inlet pipe and the test sample was submerged in water. In this case, first the temperature increase occurred in the pipe structure and then the temperature change occurred in the area where the pipe was fixed in the experimental structure. When the fluid reached the test sample, the analysis surface was exposed to the hot fluid and the dead weight of the water was included, creating a mechanical and thermal effect through mouth motion. The mechanical effect in this case created a potential loading depending on the gravitational acceleration and the weight of the water. Although this parameter is ignored in experimental studies, it is an important factor for mechanisms operating in deep water structures. In further studies, this parameter will come to the fore in experimental and finite element analysis simulations of the materials preferred in the ship industry. Figure 3 shows the temperature change behavior of the thermal cycling test device during 1 cycle through mouth motion. First, the 65°C liquid flow from the hot water line reached the chamber in show Figure 3A. The control structure of this situation is realized by the solenoid valve in the time delay time band. When enough fluid enters the chamber, the PLC control unit closes the solenoid valve, ensuring that the hot fluid remains in the chamber for the specified time in Figure 3B. With the completion of the hot cycle period, the second step is to remove the fluid from the chamber by opening the outlet line in the time band and removing the fluid from the sample in Figure 3C. Afterwards, the cold fluid line was filled into the 5 °C fluid test chamber by opening the solenoid valve in Figure 3D. The last step in this process was to discharge the fluid. Thus, 1 thermal cycle was completed. For the second thermal cycle, this process continued until the determined thermal cycle number by showing the same behavior in the same time band.

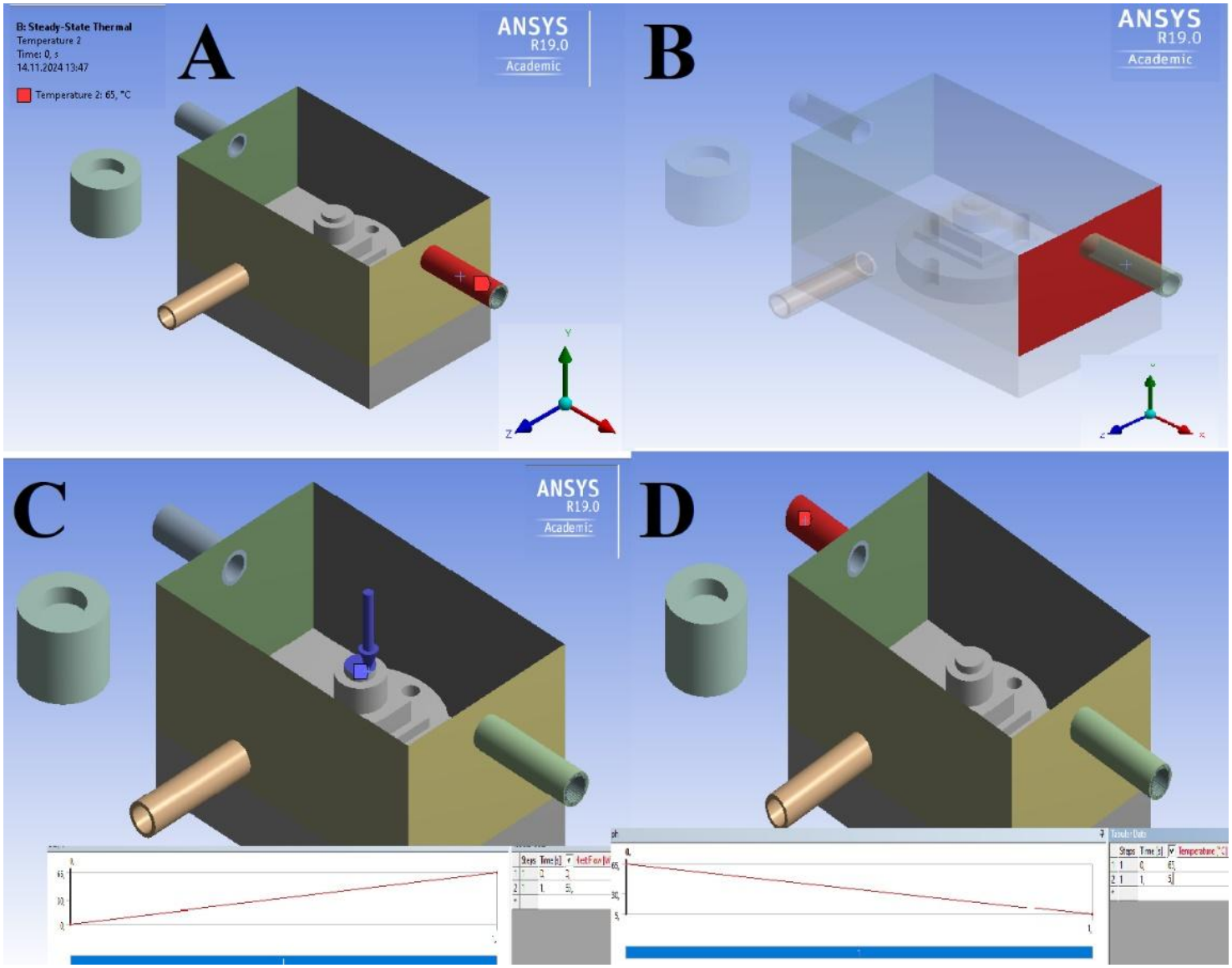

Figure 3. A-D. Temperature change behavior of the thermal cycling test device during 1 cycle through mouth motion

Figure 4 shows the thermal temperature environment behavior of pure titanium test specimens with circular and square geometry. The design of the test samples and their behavior under ideal ambient conditions are shown in Figure 4A. The environment where the circular test specimen is at 65°C and the square test specimen is at 5°C is shown in Figure 4B. Figure 4C and Figure 4D show that the square test specimen is included in the heated medium while the circular test specimen is cooling through mouth motion test mechanism.

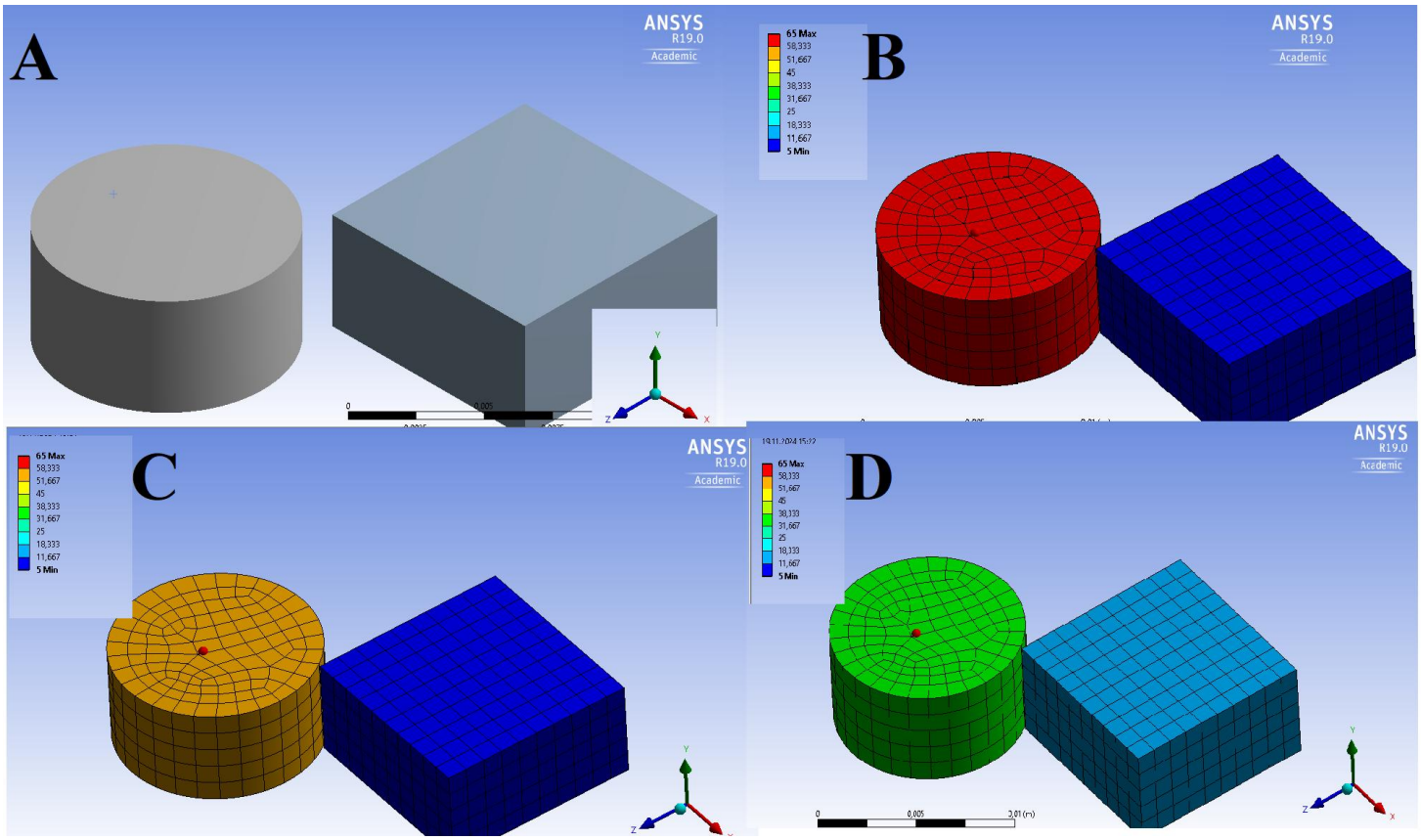

Figure 4. A-D. Thermal temperature environment behavior of pure titanium test specimens with circular and square geometry (temperature unit as °C)

DISCUSSION

The Finite Element Analysis method provides many advantages to researchers in mathematical modeling of experimental studies. The most basic of these advantages can be explained as being able to model in a very short time, being economical, and being more suitable for parameter changes. The ability to model laboratory test experiments one-to-one also provides the opportunity to observe the effects of parameters ignored in laboratory test experiments on the experimental system. Thus, the parameter selection in laboratory test experiments will be more likely to remain in the optimum region. In the literature, many researchers have simulated chewing test experiments *in vitro* and evaluated the mechanical behavior of various biomaterials.[10–13] In experimental studies, it may not always be possible to precisely control standard test parameters. Because the mechanical and control capability of the device that provides the test mechanism is very important for modeling living tissue. For example, the thermal cycling environment was ignored in some chewing test experiments in intra-oral tribology.[14–16] Considering the formation of wear mechanisms during mastication, the occurred of thermal cycling environment is inevitable in both two- and three-component wear mechanism processes. In addition, the type of opposing material selected in the test environment, the chewing force, and the minimum and maximum limits of the thermal cycling environment can positively or negatively affect the mechanical and aesthetic behavior of the test material compared to biomaterials.[17] For these reasons, the evaluation of the parameters that may affect the chewing movement will play an important role in determining the service life of the materials used in the processing process. The parameters of the thermal cycle test procedure (such as exposure time, number of thermal cycles, test temperature range) affect the mechanical and aesthetic behavior of the material. It is reported in the literature that the temperature experienced in the human mouth is approximately 37 degrees. However, this temperature value may vary in variable areas of the mouth structure. Since the material life is evaluated with laboratory test experiments, selecting areas where the temperature is variable will increase the consistency of the test results. Therefore, it is accepted that the temperature is not constant throughout the chewing tests and has a variable structure.[8] The temperature environment in the human oral

cavity is dynamic, so it is very difficult to determine the temperature range that is closest to the physiology of the oral cavity. It is important to consider as many variables as possible that can affect tooth temperature. The main sources of temperature stabilization in the mouth are the cheeks, tongue and periodontal tissue surrounding the teeth, which act as a physical barrier that regulates the temperature distribution of the samples.[18] Liquids that people swallow while chewing can be drunk at temperatures between 0 and 100°C, but cooked foods and frozen solids can reach oral temperatures outside this range. The temperature range that an individual can tolerate can vary among different populations and may depend on variables such as the number of teeth, the amount of dentin, the degree of keratinization of the oral mucosa, and the patient's gender in human factory.[19] In addition, dental materials placed in the mouth are subject to continuous and extreme changes in the oral environment due to temperature and pH fluctuations. The temperature cycle in the temperature parameter simulates the entry of hot and cold substances into the oral cavity and shows the linear thermal expansion coefficient relationship between the tooth and the restorative material.[8] The effect of artificial aging of dental materials during thermal cycling can be twofold. This effect causes an improvement in the mechanical behavior of the material, primarily water absorption in composite materials. In the second stage, it can reduce wear by creating a lubricating effect during wear mechanisms. Therefore, it is inevitable for teeth and dental materials to be exposed to thermal stress when the temperature changes. This thermal stress can cause wear mechanisms to lose more material. In addition, this situation can create some problems in terms of material integrity and aesthetics. In a previous experimental study in the literature, it was reported that Durafill composite material experienced more particle loss on the wear surface in thermal cycling test experiments.[20]

CONCLUSION

The results obtained showed that the temperature distribution in the circular test sample exhibited a more homogeneous distribution behavior than the square test sample. This result reveals the importance of the geometric structure of the test sample in the experimental environment conditions. Therefore, the use of a circular test sample in *in vitro* laboratory thermal cycling experiments will increase the accuracy of the results obtained under mouth motion simulation tests. As a result, the results obtained in this study are expected to mathematically guide the selected parameters in *in vitro* and *in vivo* studies. In addition to the data obtained from this study will increase the test validity of experimental studies by modeling them with finite element analysis simulation.

Peer-review: Externally peer-reviewed.

Conflict of Interest: The author has no conflicts of interest to declare.

Financial Disclosure: The author declared that this study has received no financial support

REFERENCES

1. Tkachenko S, Datskevich O, Kulak L, Jacobson S, Engqvist H, Persson C. Wear and friction properties of experimental Ti–Si–Zr alloys for biomedical applications. *J Mech Behav Biomed Mater*. 2014;39:61-72. doi:10.1016/j.jmbbm.2014.07.011
2. Cvijović-Alagić I, Cvijović Z, Mitrović S, Panić V, Rakin M. Wear and corrosion behaviour of Ti–13Nb–13Zr and Ti–6Al–4V alloys in simulated physiological solution. *Corros Sci*. 2011;53(2):796-808. doi:10.1016/j.corsci.2010.11.014
3. Yilmaz E, Sadeler R. Effect of different thermal change tests of micro tensile strength behavior bio-composite materials; In vitro study. *Biomed Res J*. 2021;8(1):14. doi:10.4103/bmrj.bmrj_6_21
4. Bordbar-Khiabani A, Gasik M. Electrochemical and biological characterization of Ti–Nb–Zr–Si alloy for orthopedic applications. *Sci Rep*. 2023;13(1):2312. doi:10.1038/s41598-023-29553-5
5. Yilmaz EÇ. Influence of lubricating conditions on the two-body wear behavior and hardness of titanium alloys for biomedical applications. *Comput Methods Biomech Biomed Engin*. 2020;23(16):1377-1386. doi:10.1080/10255842.2020.1804882
6. Yilmaz E, Sadeler R. Effects of contact-stress on wear behavior of zirconia-reinforced lithium silicate glass-ceramic. *Biomed Biotechnol Res J*. 2020;4(1):51. doi:10.4103/bbrj.bbrj_148_19
7. Souza JCM, Bentes AC, Reis K, et al. Abrasive and sliding wear of resin composites for dental restorations. *Tribol Int*. 2016;102:154-160. doi:10.1016/j.triboint.2016.05.035
8. Morresi AL, D'Amario M, Capogreco M, et al. Thermal cycling for restorative materials: Does a standardized protocol exist in laboratory testing? A literature review. *J Mech Behav Biomed Mater*. 2014;29:295-308. doi:10.1016/j.jmbbm.2013.09.013
9. Gale M., Darvell B. Thermal cycling procedures for laboratory testing of dental restorations. *J Dent*. 1999;27(2):89-99. doi:10.1016/S0300-5712(98)00037-2
10. Yılmaz EC, Sadeler R. Investigation of three-body wear of dental materials under different chewing cycles. *Sci Eng Compos Mater*. 2018;25(4):781-787. doi:10.1515/secm-2016-0385
11. Yilmaz EÇ, Sadeler R. Investigation of Two- and Three-Body Wear Resistance on Flowable Bulk-Fill and Resin-Based Composites. *Mech Compos Mater*. 2018;54(3):395-402. doi:10.1007/s11029-018-9750-8
12. Hahnel S, Schultz S, Trempler C, Ach B, Handel G, Rosentritt M. Two-body wear of dental restorative materials☆. *J Mech Behav Biomed Mater*. 2011;4(3):237-244. doi:10.1016/j.jmbbm.2010.06.001
13. Koottathape N, Takahashi H, Iwasaki N, Kanehira M, Finger WJ. Quantitative wear and wear damage analysis of composite resins in vitro. *J Mech Behav Biomed Mater*. 2014;29:508-516. doi:10.1016/j.jmbbm.2013.10.003
14. Lazaridou D, Belli R, Petschelt A, Lohbauer U. Are resin

composites suitable replacements for amalgam? A study of two-body wear. *Clin Oral Investig*. 2015;19(6):1485-1492. doi:10.1007/s00784-014-1373-4

15. Cao L, Zhao X, Gong X, Zhao S. An in vitro investigation of wear resistance and hardness of composite resins. *Int J Clin Exp Med*. 2013;6(6):423-430.
16. Koottathape N, Takahashi H, Iwasaki N, Kanehira M, Finger WJ. Two- and three-body wear of composite resins. *Dent Mater*. 2012;28(12):1261-1270. doi:10.1016/j.dental.2012.09.008
17. Yilmaz E, Sadeler R. Effect of thermal cycling and microhardness on roughness of composite restorative materials. *J Restor Dent*. 2016;4(3):93-96. https://link.gale.com/apps/doc/A461035563/HRCA?u=anon~9db94b3b&sid=googleScholar&xid=0503b871
18. Youngson CC, Barclay CW. A pilot study of intraoral temperature changes. *Clin Oral Investig*. 2000;4(3):183-189. doi:10.1007/s007840000060
19. Barclay CW, Spence D, Laird WRE. Intra-oral temperatures during function. *J Oral Rehabil*. 2005;32(12):886-894. doi:10.1111/j.1365-2842.2005.01509.x
20. Yilmaz EÇ. Effects of thermal change and third-body media particle on wear behaviour of dental restorative composite materials. *Mater Technol*. 2019;34(11):645-651. doi:10.1080/10667857.2019.1611201

ATATÜRK ÜNİVERSİTESİ YAYINLARI
ATATURK UNIVERSITY PUBLICATIONS

Research Article DOI: 10.5281/zenodo.15729141

Determination of tramadol in pharmaceutical preparations by GC-MS method

Bilal YILMAZ [1]

[1] Department of Analytical Chemistry, Faculty of Pharmacy, Atatürk University, Erzurum, Türkiye

Emrah ALKAN [1]

[1] Department of Analytical Chemistry, Faculty of Pharmacy, Atatürk University, Erzurum, Türkiye

ABSTRACT

In this study, a gas chromatography-mass spectrometry (GC-MS) method was developed to analyze tramadol in both pure form and pharmaceutical formulations. Diclofenac served as the internal standard. The linearity of the GC-MS method was validated within a concentration range of 0.05-5.0 µg mL^{-1}. The intra- and inter-day relative standard deviations were found to be below 1.18% and 3.51%, respectively. The detection and quantification limits for the GC-MS method were determined to be 0.015 and 0.045 µg mL^{-1}, respectively. Stability testing revealed that tramadol remained stable in solutions after 24 hours of incubation at room temperature or after 72 hours of storage at 4 °C and -20°C. Under the selected assay conditions, tablet excipients did not cause any interference. Furthermore, the method proved to be effective in quantifying tramadol and ensuring the consistency of formulation content in commercial tramadol dosage forms.

Keywords: Tramadol, GC-MS, Validation, Tablet.

INTRODUCTION

For more than 40 years, tramadol has been prescribed often throughout the world; nonetheless, there is a chance that it will be abused and trafficked. Because of this, drug analysis is a crucial component of contemporary analytical chemistry and has several legal and socially significant ramifications. Tramadol is an analogue of codeine that is 2-(dimethylaminomethyl)-1-(3-methoxyphenyl) cyclohexanol or 4-phenylpiperidine. The effectiveness of tramadol, a commonly prescribed analgesic, in reducing moderate to severe pain has drawn a lot of attention in the field of pain treatment.[1]

Large oral dosages of tramadol may have a euphoric affect similar to that of oxycodone. Prevalent reasons of tramadol poisoning have been shown to be attempted suicide (52-80 %), abuse (18-31 %) and inadvertent intoxication (1–11 %). A history of chronic tramadol usage or opioid dependency was linked to at least 20% of cases of tramadol poisoning.[2]

Tramadol is metabolized extensively in the liver as a prodrug. Forensic investigation, therapeutic monitoring, medication interactions, and pharmacokinetic evaluation of tramadol all depend on an understanding of its metabolic metabolism.[3] It is usually administered orally, and within two hours, it is distributed after being fully absorbed. The therapeutic range for TD blood concentrations is 0.1-0.3 mg L^{-1}. Furthermore, it has been said that blood readings of 1 and 2 mg L^{-1}, respectively, have the potential to be lethal and harmful.[4,5]

Due to the early stage of metabolism and the fact that 6% of the population has slow-acting CPY2D6, which has a little diminished analgesic effect, the bioavailability ranges from 65% to 70%. Compounds N and O-desmethylated from tramadol are produced.[6–9]

Tramadol and its metabolites were determined using a variety of analytical techniques, such as mass spectrometry detection[10–12] or gas chromatography with nitrogen selective. Recently, novel separation techniques have been introduced, such as capillary electrophoresis[13] and performance liquid chromatography (HPLC) approaches with electrochemical[14], mass spectrometry[15–18] or fluorescence detection.[19–24]

As of right now, there is no published technique for identifying tramadol in pharmaceutical formulations using GC-MS. Therefore, the current study's goal was to create a GC-MS method that is specific, sensitive, accurate, and precise for analyzing tramadol in pharmaceutical formulations. The International Conference on Harmonization (ICH) criteria were followed in the complete validation of the proposed technique with regard to detection and quantification limits, precision, accuracy, linearity, specificity, stability, and recovery parameters.[25]

Received 04.03.2025
Revised 07.04.2025
Accepted 10.06.2025
Publication Date 24.06.2025

Corresponding author:
Bilal YILMAZ
E-mail:
yilmazb@atauni.edu.tr

Cite this article: Yılmaz B., Alkan E. Determination of tramadol in pharmaceutical preparations by GC-MS method. *NanoEra*. 2025;5(1):22-27

METHODS

Chemicals

Tramadol hydrochloride and diclofenac were purchased from Sigma-Aldrich (St. Louis, MO, USA). Contramal Retard tablet drug (100 mg tramadol hydrochloride) was obtained from the pharmacy (Erzurum, Turkey). Every chemical was of the analytical variety.

GC-MS System and chromatographic conditions

Agilent Technologies, Palo Alto, California, provided the Agilent 6890N gas chromatography system, which was outfitted with an Agilent chemstation, a 7673 series autosampler, and a 5973 series mass selective detector for the chromatographic study. The separation was performed using an HP-5 MS column (30 m × 0.25 mm I.D., USA) with a film thickness of 0.25 µm. Splitless injection was utilized with helium as the carrier gas at a flow rate of one milliliter per minute, and the injector had a capacity of one µL. The solvent delay was set to two minutes, the electron energy for the MS detector was set to 70 eV, and the transfer line temperature was set to 280°C.

The MS detector's characteristics included an electron energy of 70 eV, a solvent delay of 3 minutes, and a transfer line temperature of 290°C. The MS was employed in scan mode (m/z 40-500) for qualitative analysis and in selected ion monitoring (SIM) mode (m/z 214 for internal standard (IS) diclofenac and m/z 58 for tramadol) for quantitative analysis.

Preparation of the standard and quality control solutions

A 100 µg mL^{-1} methanol concentration was used to generate the tramadol stock solution, which was then chilled to -20°C. After that, the mixture was gradually diluted with methanol to provide standard working solutions with tramadol concentrations of 0.05, 0.10, 0.25, 0.5, 1, 2, 3, 4 and 5 µg mL^{-1}. A stock solution containing 50 µg mL-1 of IS was produced in methanol. Before being used, all of the solutions were allowed to come to room temperature from their 4°C storage. The standard working solution of tramadol was added to aliquots to create the quality control (QC) solutions at final concentrations of 0.75, 2.5 and 4.5 µg mL^{-1}, containing 0.1 mL IS (1 µg mL^{-1}).

Procedure for pharmaceutical preparations

Using the mass of the Contramal Retard tablets, the average tablet mass was computed. Following that, they underwent homogenization, fine grinding, and meticulous weighing of a portion of the powder. The necessary amount of methanol was then poured to them in a 100 mL brown measuring flask in order to dilute the powder. After sonicating the mixture for a minimum of fifteen minutes to facilitate dissolution, it was filtered using a Whatman No. 42 paper. After a suitable amount of filtrate was further diluted with methanol to ensure that the final solution's tramadol concentration was within the working range.

Data analysis

A computer program, SPSS 15.0, (SPSS Inc., Chicago, IL, USA) was utilized to perform the statistical analyses. The tramadol standard curve and subsequent calculations were derived using regression analysis techniques. The mean and standard deviation of the results were provided.

RESULTS

Method development and optimization

Based on its chemical properties, the tramadol assay method was developed. The capillary column used in this experiment, coated with 5% phenyl and 95% dimethylpolysiloxane, is an excellent choice for separation because the analytes elute as symmetrical peaks throughout a broad concentration range. For the GC oven, various temperature ranges were examined.

The ideal temperature program for a successful separation was identified at the study's conclusion. The temperature programs for the GC oven were as follows: The increases in temperature were as follows: first, from 70°C to 250 °C at 35°C min^{-1}, which was held for one minute; next, to 290°C at 20°C min^{-1}, which was kept for one minute.

It was decided to use the splitless injection mode. Early accuracy and linearity studies of the method also demonstrated the reproducibility of the 1 µL injection volume and the significance of the peak response at the selected analytical concentration.

Validation of the method

The goal of method validation is to prove that the approach is appropriate for the purpose for which it was designed, as specified in ICH guidelines. The technique was verified for linearity, accuracy, precision stability, recovery and system applicability.[25]

Specificity

To assess the specificity of the method, potential interferences between tramadol and the excipients were investigated. For the quantitative analysis using GC-MS, electron impact ionization with selected ion monitoring (SIM) was applied, targeting the ion at m/z 58 for tramadol. The mass spectrum of tramadol is shown in Figure 1. The retention time of tramadol in the GC-MS analysis was approximately 7.4 minute, with a clear and distinct peak, as illustrated in Figure 2.

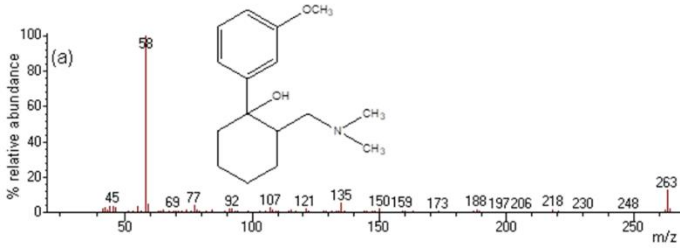

Figure 1. MS spectrum of tramadol (1.0 mg mL^{-1})

Linearity

An analytical procedure is considered linear when the test results are directly related to the analyte concentration in the sample within a specific range, either in a straightforward manner or through a well-defined mathematical transformation. Initially, linearity should be assessed visually by analyzing a plot of the signal against the analyte concentration. If the relationship appears linear, the test results should be validated

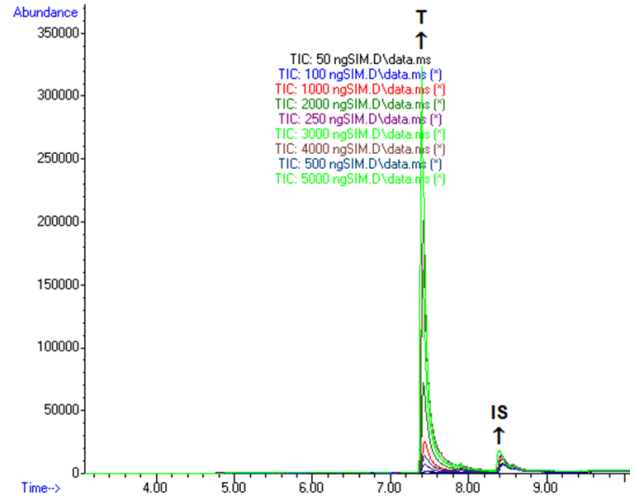

Figure 2. GC-MS chromatogram of tramadol (0.05, 0.10, 0.25, 0.5, 1, 2, 3, 4 and 5 mg mL^{-1}) and IS (1.0 mg mL^{-1})

using appropriate statistical methods, such as calculating a regression line using the least squares method. In some cases, a mathematical adjustment of the test results may be required to ensure linearity between the analyte's response and its concentration.

For the purpose of estimating the degree of linearity mathematically, information from the regression line itself may be useful. It is necessary to present the regression line's slope, residual sum of squares, y-intercept, and correlation coefficient. Analysis was done on standard solutions containing 1.0 µg mL^{-1} of IS and 0.05 - 5.0 µg mL^{-1} of tramadol. The standard curve (Fig. 3) was created by plotting the concentration of ramadol on the X-axis and the peak area ratio of tramadol and IS on the Y-axis.

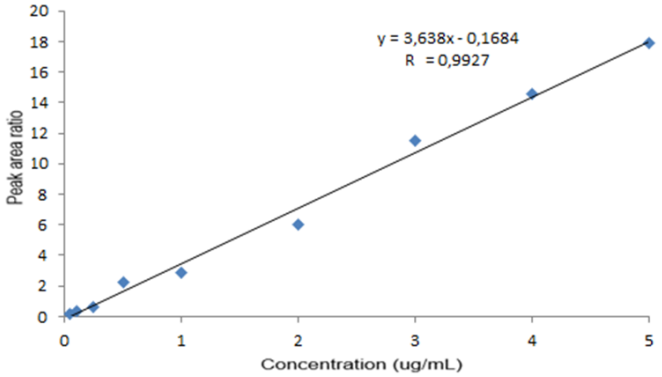

Figure 3. The standard curve of tramadol (0.10-5.0 µg mL^{-1})

Using the least squares regression approach to construct the linear regression analysis, the linearity was assessed. The regression equation was computed from the calibration graphs (Table 1).

Table 1. Linearity of tramadol

Parameter	GC-MS
Linearity (µg mL^{-1})	0.05-5.0
Regression equation	y=3.638x-0.1684
Correlation coefficient	0.9927
LOD (µg mL^{-1})	0.015
LOQ (µg mL^{-1})	0.045

[a]Based on six calibration curves, y=peak area ratio, x=concentration of tramadol

Accuracy and precision

Accuracy is described as how closely test results produced by the procedure resemble the actual value. By using known, added amounts of analyte in the experiment, it is frequently stated as the percent recovery. The exactness of the analytical process is gauged by accuracy. The true values were utilized to determine the variances of the obtained results, which were then reported as a % accuracy.

Precision is the ability to reproduce an analytical process across multiple homogeneous sample samplings. The standard deviation or relative standard deviation of a set of measurements is typically used to represent the precision of an analytical procedure. A measure of precision could be the analytical method's repeatability or degree of reproducibility under typical operating conditions.

By analyzing the QC samples six times, the assay method's accuracy for intra- and inter-day fluctuations was assessed. The precision and accuracy results for the QC samples both within and between day runs are displayed in Table 2. Between 1.18% and 3.51% ranged the precision, and between 0.67% and 3.20% the accuracy.

Table 2. Precision and accuracy of tramadol

	Intra-day			Inter-day		
Added (µg mL^{-1})	Found ± SD[a] (µg/mL)	Precision % RSD[b]	Accuracy[c]	Found ± SD[a] (µg/mL)	Precision % RSD[b]	Accuracy[c]
0.75	0.77 ± 0.027	3.51	2.67	0.74 ± 0.014	1.89	-1.33
2.5	2.42 ± 0.070	2.89	-3.20	2.52 ± 0.037	1.47	0.80
4.5	4.53 ± 0.053	1.18	0.67	4.51 ± 0.067	1.49	2.22

SD[a]: Standard deviation of six replicate determinations, RSD[b]: Relative standard deviation, Accuracy[c]: % relative error: (found-added)/addedx100

Limits of detection (LOD) and quantification (LOQ)

Tramadol's LOD and LOQ values were ascertained by evaluating various tramadol solutions and calculating the signal-to-noise ratio for every analyte. The concentration providing a signal-to-noise ratio of roughly 3:1 is the LOD, while the concentration providing a signal-to-noise ratio of roughly 10:1 with an RSD of less than 10% with triplicate analysis is the LOQ. The GC-MS technique yielded LOD and LOQ values of 0.015 and 0.045 µg mL^{-1}, respectively.

Stability

Standard solutions representing the lowest, middle, and highest points of the calibration curves were prepared independently to evaluate the stability of tramadol under varying temperatures and time conditions. The stability tests revealed that the samples remained stable for 8 hours at room temperature, for short-term storage at 4°C and -20°C, and for 72 hours at these lower temperatures for long-term storage. The stability study results, shown in Table 3, indicated no significant degradation, with values falling within the acceptable range of 90 to 110 percent. The findings are detailed in Table 3.

Table 3. Stability of tramadol in solution (n=6)

	Intra-day			Inter-day	
Conc. (µg mL^{-1})	Room temperature 24 h	Refrigeratory 4°C, 24 h	Frozen -20°C, 24 h	Refrigeratory 4°C, 48 h	Frozen -20°C, 48 h
0.5	100.7 ± 2.76	99.4 ± 3.78	99.2 ± 2.41	99.4 ± 3.47	98.5 ± 3.43
2.5	101.7 ± 2.17	100.6 ± 3.57	97.3 ± 3.75	98.2 ± 2.17	101.2 ± 2.78
5.0	99.3 ± 3.473	101.3 ± 2.74	98.4 ± 3.46	100.2 ± 2.71	99.4 ± 2.74

Table 4. Recovery of tramadol in pharmaceutical preparation

		Intra-day		Inter-day	
Pharmaceutical preparation	Added (µg mL^{-1})	Found ± SD[a] (µg mL^{-1})	% Recovery % RSD[b]	Found ± SD[a] (µg mL^{-1})	% Recovery % RSD[b]
Contramal Retard (1.5 µg mL^{-1})	0.5	0.49 ± 0.019	98.7 (4.07)	0.49 ± 0.016	97.9 (3.27)
	1.5	1.49 ± 0.071	99.2 (4.78)	1.46 ± 0.040	98.7 (2.77)
	3.5	3.51 ± 0.145	100.3 (4.13)	3.47 ± 0.178	99.2 (5.12)

SD[a]: Standard deviation of six replicate determinations, RSD[b]: Relative standard deviation

Recovery

Recovery values were obtained by adding different amounts of pure drug to tablet samples, which had already been pre-analyzed, within the analytical concentration range of the proposed method. The additional doses of each drug were then determined using the described procedure. The results from the recovery tests were considered satisfactory and are presented in Table 4.

System suitability

Before each validation run, a system suitability test was performed on the chromatographic system. Efficiency and area relative standard deviation were calculated for each of the five suitable injections. The five suitability injections' average was used to quantify the check standard. The efficiency was ≥3562 and the %RSD was ≤1.47% for all sample analysis.

Procedure for pharmaceutical preparations

The 100 mg tramadol-containing Contramal Retard tablet was precisely weighed and finely powdered. A measured amount of the powder was dissolved in 50 milliliters of methanol. Then, the solution was transferred to a 100 mL volumetric flask and filled to the mark with methanol. After properly diluting the tablet solutions, they were filtered using a Whatman filter to achieve a final concentration within the linear range of the GC-MS method (Figure 4). The tramadol concentration was determined using the calibration curve.

DISCUSSION

In biological samples, GC-MS is a potent technology that can assess low amounts of analytes quantitatively and with great specificity. High-resolution capillary GC has not been utilized as much as HPLC lately. Tramadol and O-desmethyltramadol could, however, be detected simultaneously because to its naturally high resolving power, high sensitivity, and outstanding precision and accuracy. GC in conjunction with MS also reduced the detection limits to ng levels. Through an investigation of the peak interference from the exogenous chemicals, the specificity of the approach was confirmed. Figure 2 displayed a representative tramadol and IS chromatogram.

El-Sayed et al.[10] developed a GC-MS method for the determination of tramadol and O-desmethyltramadol in human urine following α-glucuronidase hydrolysis and liquid-liquid extraction, utilizing positive electron impact ionization. The total run time for the proposed method was 12.6 minutes. The calibration curve was found to be linear within the 10-1000 ng mL^{-1} range. Intra-assay precision for tramadol and O-desmethyltramadol ranged from 1.29% to 6.48%, while inter-assay precision ranged from 1.28% to 6.84%. The intra-assay accuracy for both tramadol and O-desmethyltramadol was between 91.79% and 106.89%.

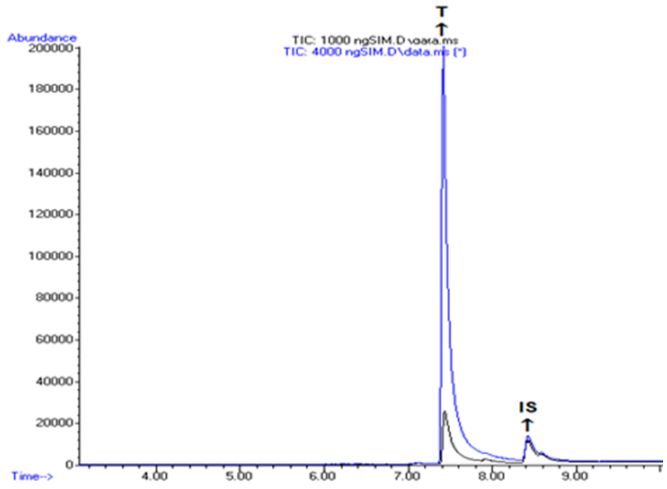

Figure 4. The chromatogram of Contramal Retard tablet solution (1.0 and 4.0 µg mL^{-1})

Using solvent bar microextraction, Ghasemi[11], a GC-MS technique has been developed for the determination of tramadol in various biological samples. With a 4.5 % RSD, the detection limit was 0.02 µg L^{-1}. A solid phase extraction technique was used to remove tramadol from plasma. In addition to being the most thorough approach, this one can extract tramadol in a single extraction process. The entire run time of the procedure is 15 minutes.

Biological samples have low sensitivity and selectivity when it comes to UV detection, even though tramadol and its metabolite molecules include a benzene ring.[26] Currently, mass spectrometry and fluorescence are the only two types of detectors that have attained low quantification levels. The lowest tramadol quantification level[12,19,21] using any of them was around 1.0 ng mL^{-1}, indicating a lower detection limit of 0.2 - 0.5 ng mL^{-1}.[12,19]

Using tandem mass detection using LC techniques, the amount of tramadol and O-desmethyltramadol in human plasma is revealed.[15–18] According to Ceccato et al.[15] tramadol and O-desmethyltramadol in human plasma were evaluated using the LC technique with tandem mass detection. The tramadol calibration curve utilizing the LC-MS/MS method was linear between 20 and 10,000 ng mL^{-1}. The RSD value indicated the intra- and inter-day precision of less than 6.4%, and relative error, or accuracy, was better than 6.1%. More sensitive would be LC-MS/MS detection, although at the moment, not all laboratories can afford it.

In the literature, tramadol was recovered from plasma using a solid phase extraction technique.[26] In addition to being the most thorough approach, this one can extract tramadol in a single extraction step. In comparison to the research published by Ardakani et al.[27] and Moore et al.[28], the mean recovery is higher. The proposed method, with a total run time of 8.0 minutes, is faster than the previously reported GC-MS methods for tramadol and its metabolites.[29,30] Additionally, it achieves adequate sensitivity for both O-desmethyltramadol and tramadol without the need for derivatization, offering an improvement over the methods previously published.[28]

This method's sensitivity was found to be sufficient for pharmacokinetic studies when applied to tablet samples. When compared to the previously mentioned methods, the current approach presents several advantages. It is either superior or at least on par with the methods described in earlier studies.[23,27–30]

CONCLUSION

In this study, a GC-MS method was developed and validated for the determination of tramadol, offering a quick and straightforward approach. The chromatographic method satisfies all essential criteria, including accuracy, linearity, recovery, and precision, making it a reliable and practical technique. Due to the 9-minute run time, a large number of samples can be analyzed in a short period. Therefore, this method is suitable not only for routine formulation and raw material analysis but also for analyzing samples during accelerated stability studies.

Peer-review: Externally peer-reviewed.
Author Contributions: Concept - B.Y., E.A.; Supervision - B.Y.; Resources - B.Y., E.A.; Materials – B.Y., E.A.; Data Collection and/or Processing - E.A., B.Y.; Analysis and/or Interpretation - B.Y., E.A.; Writing Manuscript - B.Y., E.A.; Critical Review – B.Y.
Conflict of Interest: The authors have no conflicts of interest to declare.
Financial Disclosure: The authors declared that this study has received no financial support

REFERENCES

1. Gibson TP. Pharmacokinetics, efficacy, and safety of analgesia with a focus on tramadol HCl. *Am J Med*. 1996;101:S47-S53. doi:10.1016/S0002-9343(96)00138-6
2. Shipton EA. Tramadol—Present and Future. *Anaesth Intensive Care*. 2000;28(4):363-374. doi:10.1177/0310057X0002800403
3. Cooper RJ. Over-the-counter medicine abuse – a review of the literature. *J Subst Use*. 2013;18(2):82-107. doi:10.3109/14659891.2011.615002
4. Almér Herrnsdorf E, Holmstedt A, Håkansson A. Tramadol misuse in treatment-seeking adolescents and young adults with problematic substance use – Prediction of treatment retention. *Addict Behav Reports*. 2022;16:100446. doi:10.1016/j.abrep.2022.100446
5. Miotto K, Cho AK, Khalil MA, Blanco K, Sasaki JD, Rawson R. Trends in Tramadol: Pharmacology, Metabolism, and Misuse. *Anesth Analg*. 2017;124(1):44-51. doi:10.1213/ANE.0000000000001683
6. Allegaert K, Anderson BJ, Verbesselt R, et al. Tramadol disposition in the very young: an attempt to assess in vivo cytochrome P -450 2D6 activity. *Br J Anaesth*. 2005;95(2):231-239. doi:10.1093/bja/aei170
7. Goeringer KE, Logan BK, Christian GD. Identification of Tramadol and its Metabolites in Blood from Drug-Related Deaths and Drug-Impaired Drivers. *J Anal Toxicol*. 1997;21(7):529-537. doi:10.1093/jat/21.7.529
8. Quetglas EG, Azanza JR, Cardenas E, Sádaba B, Campanero MA. Stereoselective pharmacokinetic analysis of tramadol and its main phase I metabolites in healthy subjects after intravenous and oral administration of racemic tramadol. *Biopharm Drug Dispos*. 2007;28(1):19-33. doi:10.1002/bdd.526
9. Ardakani YH, Rouini M. Pharmacokinetics of tramadol and its three main metabolites in healthy male and female volunteers. *Biopharm Drug Dispos*. 2007;28(9):527-534. doi:10.1002/bdd.584
10. El-Sayed A-AY, Mohamed KM, Nasser AY, Button J, Holt DW. Simultaneous determination of tramadol, O-desmethyltramadol and N-desmethyltramadol in human urine by gas chromatography–mass spectrometry. *J Chromatogr B*. 2013;926:9-15. doi:10.1016/j.jchromb.2013.02.019
11. Ghasemi E. Optimization of solvent bar microextraction combined with gas chromatography mass spectrometry for preconcentration and determination of tramadol in

biological samples. *J Chromatogr A*. 2012;1251:48-53. doi:10.1016/j.chroma.2012.06.060

12. Sha YF, Shen S, Duan GL. Rapid determination of tramadol in human plasma by headspace solid-phase microextraction and capillary gas chromatography–mass spectrometry. *J Pharm Biomed Anal*. 2005;37(1):143-147. doi:10.1016/j.jpba.2004.09.050
13. Rudaz S, Veuthey JL, Desiderio C, Fanali S. Simultaneous stereoselective analysis by capillary electrophoresis of tramadol enantiomers and their main phase I metabolites in urine. *J Chromatogr A*. 1999;846(1-2):227-237. doi:10.1016/S0021-9673(99)00028-X
14. Valle M, Pavón J., Calvo R, Campanero M., Trocóniz I. Simultaneous determination of tramadol and its major active metabolite O-demethyltramadol by high-performance liquid chromatography with electrochemical detection. *J Chromatogr B Biomed Sci Appl*. 1999;724(1):83-89. doi:10.1016/S0378-4347(98)00547-7
15. Ceccato A, Vanderbist F, Pabst J-Y, Streel B. Enantiomeric determination of tramadol and its main metabolite O-desmethyltramadol in human plasma by liquid chromatography–tandem mass spectrometry. *J Chromatogr B Biomed Sci Appl*. 2000;748(1):65-76. doi:10.1016/S0378-4347(00)00318-2
16. Musshoff F, Madea B, Stuber F, Stamer UM. Enantiomeric Determination of Tramadol and O-Desmethyltramadol by Liquid Chromatography-Mass Spectrometry and Application to Postoperative Patients Receiving Tramadol. *J Anal Toxicol*. 2006;30(7):463-467. doi:10.1093/jat/30.7.463
17. Musshoff F, Trafkowski J, Kuepper U, Madea B. An automated and fully validated LC-MS/MS procedure for the simultaneous determination of 11 opioids used in palliative care, with 5 of their metabolites. *J Mass Spectrom*. 2006;41(5):633-640. doi:10.1002/jms.1021
18. Zhu T, Ding L, Guo X, Yang L, Wen A. Simultaneous Determination of Tramadol and Acetaminophen in Human Plasma by LC–ESI–MS. *Chromatographia*. 2007;66(3-4):171-178. doi:10.1365/s10337-007-0268-9
19. Campanero MA, Calahorra B, García-Quetglás E, Escolar M, Honorato J. High-performance liquid chromatographic assay for simultaneous determination of tramadol and its active metabolite in human plasma. Application to pharmacokinetic studies. *Chromatographia*. 1998;48(7-8):555-560. doi:10.1007/BF02466649
20. Nobilis M, Kopecký J, Květina J, et al. High-performance liquid chromatographic determination of tramadol and its O-desmethylated metabolite in blood plasma. *J Chromatogr A*. 2002;949(1-2):11-22. doi:10.1016/S0021-9673(01)01567-9
21. Campanero MA, García-Quetglas E, Sádaba B, Azanza JR. Simultaneous stereoselective analysis of tramadol and its primary phase I metabolites in plasma by liquid chromatography. *J Chromatogr A*. 2004;1031(1-2):219-228. doi:10.1016/j.chroma.2003.11.034
22. Pedersen RS, Brøsen K, Nielsen F. Enantioselective HPLC method for quantitative determination of tramadol andO-desmethyltramadol in plasma and urine: Application to clinical studies. *Chromatographia*. 2003;57(5-6):279-285. doi:10.1007/BF02492397
23. Rouini M-R, Ardakani YH, Soltani F, Aboul-Enein HY, Foroumadi A. Development and validation of a rapid HPLC method for simultaneous determination of tramadol, and its two main metabolites in human plasma. *J Chromatogr B*. 2006;830(2):207-211. doi:10.1016/j.jchromb.2005.10.039
24. LI Q, Wang R. Simultaneous analysis of tramadol, metoprolol and their metabolites in human plasma and urine by high performance liquid chromatography. *Chin Med J (Engl)*. 2006;119(23). https://journals.lww.com/cmj/fulltext/2006/12010/simultaneous_analysis_of_tramadol,_metoprolol_and.12.aspx
25. Validation of analytical procedures: Text and Methodology. In: *International Conference on Harmonization (ICH). Commission of the European Communities*. Vol 2. ; 1996.
26. Gan S., Ismail R. Validation of a high-performance liquid chromatography method for tramadol and o-desmethyltramadol in human plasma using solid-phase extraction. *J Chromatogr B Biomed Sci Appl*. 2001;759(2):325-335. doi:10.1016/S0378-4347(01)00237-7
27. Ardakani YH, Rouini M-R. Improved liquid chromatographic method for the simultaneous determination of tramadol and its three main metabolites in human plasma, urine and saliva. *J Pharm Biomed Anal*. 2007;44(5):1168-1173. doi:10.1016/j.jpba.2007.04.012
28. Moore C, Rana S, Coulter C. Determination of meperidine, tramadol and oxycodone in human oral fluid using solid phase extraction and gas chromatography–mass spectrometry. *J Chromatogr B*. 2007;850(1-2):370-375. doi:10.1016/j.jchromb.2006.12.008
29. Cheng P-S, Lee C-H, Liu C, Chien C-S. Simultaneous Determination of Ketamine, Tramadol, Methadone, and their Metabolites in Urine by Gas Chromatography-Mass Spectrometry. *J Anal Toxicol*. 2008;32(3):253-259. doi:10.1093/jat/32.3.253
30. Chytil L, Štícha M, Matoušková O, Perlík F, Slanař O. Enatiomeric determination of tramadol and O-desmethyltramadol in human urine by gas chromatography–mass spectrometry. *J Chromatogr B*. 2009;877(20-21):1937-1942. doi:10.1016/j.jchromb.2009.04.042

ATATÜRK ÜNİVERSİTESİ YAYINLARI
ATATURK UNIVERSITY PUBLICATIONS

Review Article

DOI: 10.5281/zenodo.15729170

Green synthesis, characterization and applications of manganese oxide nanoparticles

Meshach Danjuma FRIDAY [1, 2]

[1] Department of Science Laboratory Technology, Newland Polytechnic, Ilorin, Nigeria

[2] Department of Industrial Chemistry, Faculty of Physical Sciences, University of Ilorin, Ilorin, Nigeria

ABSTRACT

Nanotechnology is a promising and rapidly evolving field. Nanotechnology has received increased attention in recent years due to the need to create biocompatible materials for a variety of applications in fields such as health, medicine, water treatment and purification, and so on. Metal and Metal Oxide is one element of nanoscience and nanotechnology that has various applications in a variety of fields and has piqued the curiosity of academics. However, manganese and manganese oxide have received less attention as a high-performance metal in a variety of applications, including medicine, biomedicine, biosensors, water treatment and purification, electronics, electrochemistry, photo-electronics, catalysis, and so on. The standard methods of synthesizing nanoparticles can be harmful to the environment and living things. Thus, the greener way to nanoparticles (NPs) synthesis is recommended. It has various advantages, including being non-toxic, environmentally friendly, clean, less expensive, and almost new, as well as the ability to be done at room pressure and temperature. This review focuses on collection of comprehensive information from recent developments in the synthesis, characterization and applications from previous scientific findings on the biological method of synthesizing manganese oxide nanoparticles (MnO NPs) due to the aforementioned advantages. Green synthesis of MnO NPs leverages the benefits of bioactive compounds from plant extracts, which help in controlling the size, shape, and surface characteristics of the nanoparticles. This results in enhanced antibacterial activity, catalytic activity, electrochemical performance, magnetic behavior, and fluorescent properties while ensuring biocompatibility and environmental safety. Consequently, MnO NPs synthesized via green methods are highly suitable for a wide range of applications, including environmental remediation, electronics, biomedical imaging, and nutritional supplements.

Keywords: Nanoparticles, Manganese oxide, Green synthesis, Biomedicine, Characterization.

INTRODUCTION

Nanomaterials, with a length scale of less than 100 nm, have garnered significant attention not only for their fundamental scientific value but also for their remarkable applications stemming from unique electrical, magnetic, and catalytic capabilities.[1] These nanoparticles are of interest due to their potential applications across diverse fields, including medicine, wastewater treatment, agriculture, energy production, and environmental remediation.[2,3] Metal nanoparticles (NPs), in particular, exhibit exceptional surface area-to-volume ratios, high surface energy, spatial confinement, and minimal defects, alongside superior physicochemical, electrical, mechanical, magnetic, thermal, dielectric, optical, and biological properties compared to as compared with other materials.[4–7]

Among the 3D transition metal oxides, manganese oxides, including MnO, Mn_5O_8, Mn_2O_3, MnO_2, and Mn_3O_4, have piqued researchers' interest due to their numerous structural and compositional variations.[8] Manganese oxide nanoparticles show significant promise for sustainable nanotechnology.[9] They find extensive applications in imaging contrast agents, magnetic storage devices, water treatment, and purification, owing to their advantageous physical and chemical properties.[10–16]

Various methods, such as chemical precipitation, sol-gel, solvothermal/hydrothermal, solid-state synthesis, electrochemical, and photochemical reduction techniques, are widely employed for the synthesis of nanoparticles.[17–19] However, physical and chemical methods often involve energy-intensive, costly processes and the use of toxic substances.[20] In contrast, green synthesis offers an alternative route to producing biocompatible nanoparticles. This eco-friendly, cost-effective, and less energy-demanding approach utilizes biological materials such as bacteria, fungi, algae, yeast, and plant extracts as reducing agents.[21–23] Among these, plant-based synthesis has garnered particular interest due to its simplicity and efficiency.[24–26] Plant phytochemicals, such as alkaloids, polyphenols, flavonoids, and terpenoids, have demonstrated their ability to reduce metal ions and synthesize stable nanoparticles.[27,28] Moreover, biogenic plant phytomolecules can enhance the nanoparticles' intrinsic properties, such as antioxidant, antibacterial, and anticancer activities, compared to their extracts.[29–31]

Received 28.10.2024
Revised 06.05.2025
Accepted 07.05.2025
Publication Date 24.06.2025

Corresponding author:
Meshach Danjuma FRIDAY
E-mail:
meshachfridaydan@gmail.com

Cite this article: Friday MD. Green synthesis, characterization and applications of manganese oxide nanoparticles. *NanoEra*. 2025;5(1):28-41

This article provides a comprehensive review of green synthesis approaches for MnO NPs to address the limitations of traditional physical and chemical synthesis methods. It begins by exploring various synthesis methods, with a focus on green synthesis and the effects of experimental parameters on MnO NPs production. Next, characterization techniques are reviewed, highlighting their role in understanding the morphology, optical properties, crystallinity, and surface chemistry of MnO NPs. Finally, the article highlights the diverse applications of MnO NPs, including antibacterial activity, dye degradation, electrochemical properties, magnetic behavior, fluorescence, and their potential as nutritional supplements. Through this structured analysis, the review aims to provide a detailed understanding of the green synthesis of MnO NPs using plant extracts as reducing and stabilizing agents, along with their emerging applications.

SYNTHESIS OF MnO NPs

Manganese oxide nanoparticles with various shapes and exceptional qualities have been synthesized via several innovative and novel methods, including the hydrothermal method, chemical method[32], sol-gel synthesis method[33], ultrasonic bath method[34], thermal decomposition method[35,36], laser ablation method[35], and green synthesis method.[16] The chart showing the various methods of MnO NPs synthesis are showed in Figure 1.

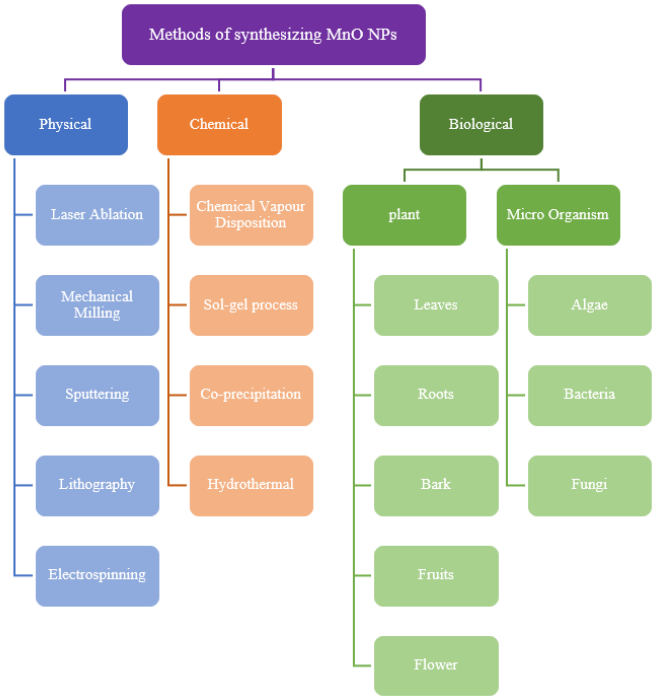

Figure 1. Flow chart representing the various methods of synthesis of MnO NPs.

Chemical Method

Atoms, molecules, and clusters are used in chemical processes to construct Manganese oxide NPs structures. As a result, the majority of these approaches rely on a bottom-up approach that employs appropriate precursors and additives.[37]. Wet chemical, chemical vapor disposition, direct precipitation, solvothermal, hydrothermal, sonochemical, microwave-assisted combustion, electrode-position, homogeneous precipitation, sol-gel, spray drying, microwave irradiation, reverse micelles, and spray pyrolysis methods, as well as the manganese-alcohol reaction, are examples of chemical processes.[38–40] Although chemical procedures are simple, economical, and continuous processes with high efficiency[41,42], they can be harmful to persons and the environment due to the presence of dangerous substances. Some of the substances utilized in chemical and physical techniques may remain on the NPs, providing major dangers to medical applications.[43] Advantages and disadvantages of this methods are shown in Table 1. In Sol-Gel Method, this technique involves the hydrolysis and condensation of metal alkoxides to form a gel, which is then calcined to produce MnO NPs. Sol-gel synthesis enabled precise control over particle morphology and crystallinity.[44] MnO_2 was successfully fabricated using a gel formation process followed by calcination at 400°C (MnO_4) and 700°C (MnO_7) in the presence of air.[44] The structural and morphological analyses revealed to be a body-centered tetragonal crystal lattice with a nano-tablet-like porous surface with size of 12.6 nm and 16.2 nm. In Co-Precipitation Method, this approach involves the reaction of manganese salts with alkaline solutions, leading to the formation of MnO NPs. For example, MnO NPs were synthesized using manganese acetate and sodium hydroxide, achieving nanoparticles with size of about 18.35 nm and high crystallinity.[45] However, the process often requires post-synthesis purification to remove by-products. Thus, cost-effective and ecologically benign technologies for Manganese oxide NPs synthesis are urgently required. Figure 1 shows the various chemical methods used for the synthesis of MnO NPs.

Physical Method

The primary physical approaches are laser ablation, mechanical milling, sputtering, lithography evaporation/condensation and electrospinning.[35] Physical synthesis methods have the benefit of avoiding solvent contamination in the generated thin films and ensuring uniform MnO NPs distribution as compared to chemical approaches. The advantages and disadvantages of this method are shown in Table 1. Physical synthesis of NPs using a tube furnace at atmospheric pressure has some drawbacks, such as the fact that the tube furnace takes up a lot of space, consumes a lot of energy while raising the ambient temperature around the source material, and takes a long time to achieve thermal stability. Furthermore, a typical tube boiler takes more than a few kilowatts of power and several tens of minutes of preheating time to achieve a steady operating temperature.[46,47] Laser ablation of metallic bulk materials in solution could be used to synthesize manganese nanoparticles. One significant advantage of laser ablation approach over other ways for producing metal colloids is the absence of chemical reagents in solutions. Manganese oxide nanoparticles in the Mn_3O_4 phase were synthesized using the laser ablation of solids in liquids technique (LASL).[48] The experiments were carried out by ablating a manganese (Mn) target immersed in deionized water as the

liquid medium, with a pulsed Nd:YAG laser with a wavelength of 1064 nm. The effect of ablation time on the formation of these oxides was studied as an important parameter, which determines the final composition of the obtained products. The results showed that the nanoparticles are well crystalized and have an approximate size between 7 and 11 nm. This approach can produce pure and uncontaminated metal colloids for future uses.[49] Figure 1 shows the various physical methods that can be used for the synthesis of MnO NPs.

Biological Method

The biological approach to MnO NPs manufacturing includes the use of organisms (bacteria, yeast, and fungi) and plant extracts as reducing agents for metal ions[50–52] as shown in Figure 2. Synthesized monodispersed orthorhombic MnO_2 with Bacillus sp., a heavy metal resistant bacterium.[10] The MnO_2 produced was intracellular and recoverable. Plant-based NP synthesis is extremely cost effective, making it an economically viable and valuable alternative for large-scale NP production.[53] Biomolecules such as flavonoids, proteins, tannins, phenols, and terpenoids have been shown to be effective reducing and stabilizing agents for MnO NP production. Plants rich in antioxidants can also be employed to make the NPs. The antioxidant polyphenols in the plant act as reducing and stabilizing agents.[54,55] A plant extract from Kalopanaxpictus and Yucca gloriosa with curcumin was utilized to create NPs of size 19.2 and 80 nm, respectively, at room temperature, without utilizing the catalyst or other costly materials.[56,57] Green synthesis of MnO NPs using plant extracts as the source of electron generation for manganese salt reduction has certain advantages over microbe-based synthesis in that it does not require cell culture upkeep and can be scaled up for large-scale production.[53] The advantages and disadvantages of the biological method of synthesis are summarized in Table 1. The synthesis of MnO NPs utilizing a plant extract of Moringa oleifera is shown in Figure 2.

The following equations indicate the probable mechanism involved in MnO NPs synthesis.

$$Mn^{2+} + \text{plant extract} \rightarrow [Mn/\text{plant extract}]^{2+}$$
$$[Mn/\text{plant extract}]^{2+} \rightarrow \text{heat } [Mn(OH)_2/\text{plant extract}]$$
$$[Mn(OH)_2/\text{plant extract}] \text{ (Incubation)} \rightarrow \text{MnO NPs}$$

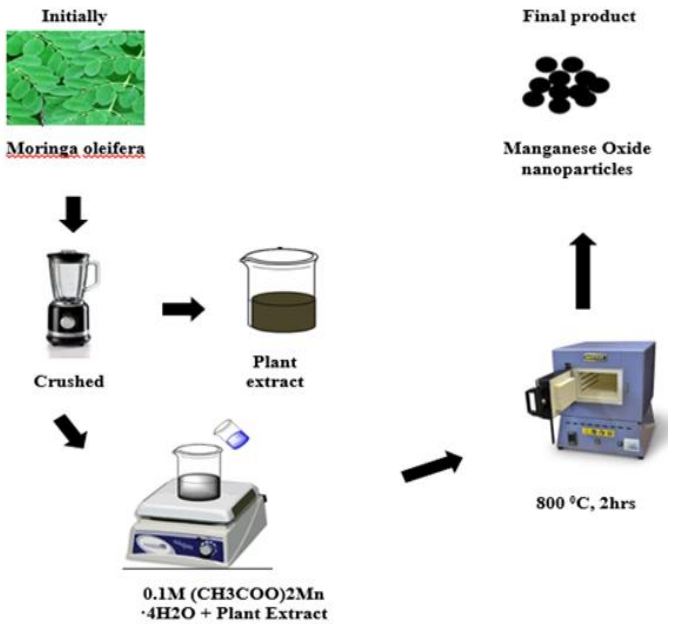

Figure 2. The green synthesis of MnO NPs

EFFECTS OF EXPERIMENTAL PARAMETERS ON MnO NPs SYNTHESIS

The biosynthesis of nanoparticles is influenced by several factors that significantly affect their characteristics and properties.[58] To obtain nanoparticles with the desired size, shape, composition, stability, and other attributes, these factors must be carefully monitored and optimized. The following are parameters impacting nanoparticle synthesis include temperature, pH, type of plant extracts and concentrations, and reaction time.[58]

Effect of pH

pH is a significant element influencing MnO NPs creation using green technology methods. Researchers revealed that the pH of the solution medium affects the size and texture of the synthesized MnO NPs.[59,60] As a result, changing the pH of the solution media can affect the size of the nanoparticles. A solution medium with pH values ranging from 7 to 9 has been identified as the ideal setting for the creation of nanoparticles from *Aeromonas hydrophila* extract.[61]

Table 1. Advantages and disadvantages of different methods of MnO NPs synthesis[59,62-68]

Method	Advantages	Disadvantages	References
Chemical	It enhances large production	Generation of non-ecofriendly products, it is energy intensive processes, use of toxic solvents as reducing and stabilizing agent	62–64
Physical	Control crystallinity, shape and production of MnO NPs with uniform, controlled size and high purity are achievable	Require high capital cost and consume large energy	65,66
Biological	This method is cost effective, non-toxic use of materials and simple	Using microorganisms is not attractive due to the requirements of aseptic cultivation and increased production cost at industrial scale	59,67,68

Effect of Temperature

Temperature is another significant element that influences MnO NPs production via all three processes. Physical procedures demand higher temperatures (>350°C), while chemical approaches require lower temperatures.[61] MnO NPs synthesis utilizing green technology often requires temperatures below 100°C or ambient temperature. The temperature of the reaction medium determines the type of nanoparticle generated.[69] The effect of temperature on the green synthesis of MnO_2 NPs was studied by varying the temperature conditions of the mixture from 75°C to 95°C.[70] The result shows that higher temperature conditions (up to 90 °C) favors the formation of MnO_2 NPs. A further increase in temperature supports the agglomeration of nanoparticles leading to decreased absorbance values. Generally, higher temperatures result in faster reaction rates but may also promote particle aggregation or undesired growth. Thus, controlling the temperature is important to achieve nanoparticles with the desired properties.[71].

Effect of Time

The duration of incubation of the reaction medium has a significant impact on the quality and kind of MnO NPs synthesized utilizing green technology.[72] Similarly, the properties of the synthesized nanoparticles changed over time and were heavily influenced by the synthesis method, light exposure, and storage conditions, among other factors.[73,74] Variations in time can occur in a variety of ways, including particle aggregation caused by long-term storage; particles that shrink or expand during long-term storage; shelf life, and so on, all of which affect their potential.[75]

Effect of type of plant extracts and concentrations

Secondary metabolites found in several living systems, including plants, operate as reducing and stabilizing agents in the creation of MnO NPs. However, the content of these metabolites changes according to the kind of plant, plant portion, and extraction method.[76] Similarly, various microbes produce different internal and extracellular enzymes in varied amounts, which influence nanoparticle production.[77] To achieve the best conditions for green synthesis of MnO NPs, the volume of plant extract must be proportional to the quantity of manganese precursor employed.[78] The yield of MnO NPs depends heavily on the volume of extract utilized for synthesis.[79] According to the findings, the volume and kind of extract utilized in nanoparticle manufacturing have a significant impact on their morphological qualities and biological activities.[80]

CHARACTERIZATION OF MnO NPs

UV-visible (UV-Vis) spectroscopy

UV-visible spectroscopy is a type of molecular spectroscopy that operates using the Bouguer Lambert Beer law. In conjunction with electromagnetic waves, this approach measures Plasmon resonance and total oscillations of the electron conduction band. It is also used to assess fluid absorption as well as other materials.[81] When a light beam passes through a solution, some of it may be absorbed while the remainder is transmitted through it. Transmittance is the ratio of light entering a sample to light exiting it at a certain wavelength. Absorbance is the negative logarithm of transmittance.[82] MnO NPs exhibited UV-Visible absorption spectra ranging from 284 to 400 nm due to $n\rightarrow\pi^*$ and $\pi\rightarrow\pi^*$ transitions.[14,83,84] Furthermore, distinct absorption peaks of MnO NPs suggested that the shape and size of manufactured nanoparticles varied depending on the synthesis process.[85,86] Metal nanoparticles' absorption spectra move towards longer wavelengths as particle size rises.[86,87] Findings on the uses and application of UV as characterization tools in green synthesis of MnO NPs are summarized in Table 2 and 3.

FTIR spectrophotometer

The FTIR analysis is used to identify organic, inorganic, and polymeric compounds by scanning the samples with infrared light. Changes in the typical pattern of absorption bands plainly show a change in material composition. FTIR is useful for identifying and characterizing unknown compounds, detecting impurities, locating additives, and determining decomposition and oxidation.[82] Infrared radiation (10,000 – 100 cm^{-1}) is transmitted through the sample, with some being absorbed and some going through. The absorbed radiation is transformed by the sample into vibrational or rotational energy. The detector produces a signal ranging from 4000 to 400 cm^{-1}, representing the sample's molecular fingerprint. Each molecule has a distinct fingerprint, making FTIR an invaluable tool for chemical identification.[88] MnO NPs are identified by conspicuous peaks such as O-H, C=O, C-O, C-N, C-H, and C≡C as shown in Table 3.

Scanning Tunnelling Microscopy (STM)

This tool produces surface pictures with atomic-scale lateral resolution. A fine probe with a tip scans the conducting sample's surface using a piezoelectric crystal, and the resulting tunnelling current is measured. Quantum tunnelling is the working principle of STM. The surface topography is determined by graphing the tip's height as a function of its lateral position over the sample.[82] STM can be employed in air, vacuum, liquid, or gas at a variety of temperature ranges. The procedure might be difficult because the tip must be sharp and the surfaces clean. Carbon nanotube tips are employed for STM.[89] It is a potentially useful technique for characterizing nanoparticles. The growth of MnO NPs is monitored using STM. Previous studies on the use of STM as a characterization technique is shown in Table 2.

Atomic Force Microscopy (AFM)

AFM is a powerful and adaptable microscopy technique for studying samples at the nanoscale.[90] It captures an image in three dimensions and gives several types of surface measurements to fulfil the needs of scientists. AFM can produce images at atomic resolution with angstrom scale resolution height information while requiring minimal sample preparation. In nanotechnology, it may be used to detect surface roughness and visualize surface texture on a wide range of materials. It is also a non-destructive approach with excellent three-dimensional spatial resolution.[82] Previous studies on the use of

AFM as a characterization technique is shown in Table 2.

Transmission electron microscopy (TEM)

TEM is regarded as the most effective electron microscopy technique for determining the morphological identities of MnO NPs and other metal nanoparticles.[91] In the TEM technique, an electron beam is delivered through the sample, interacts with it, and the transmitted electrons are used to generate a picture by magnifying and focusing them with an objective lens.[82] The upgraded version of TEM with better resolution, which permits imaging of a sample's crystallographic structure at the atomic level. Unlike traditional microscopy, which uses absorption to form images, high resolution transmission electron microscopy creates images by interference in the image plane.[82] Previous studies on the use of TEM are shown in Table 2.

Scanning electron microscopy (SEM)

SEM is used to characterize the morphology of MnO NPs. SEM is a popular approach for imaging surfaces at high resolution, and it can also be used to characterize nanoscale materials. SEM images using electrons in the same way as a light microscope does with visible light.[92] It is limited in some morphological analyses because it provides insufficient information about the true population and average size distribution.[93] SEM has been shown to harm several nanopolymers. As a result, for effective morphological examination by SEM, the NPs must be able to sustain vacuum pressure.[94] Another disadvantage of this technology is that it is quite expensive and slow. Other studies demonstrating the morphological characterization of biosynthesized MnO NPs using SEM are provided in Table 3.

Dynamic Light Scattering (DLS)

DLS is often referred to as quasi-elastic light scattering. It is a widely used approach for determining the size of MnO NPs in colloidal solutions in the nano- and submicrometer ranges.[92] The MnO NPs in a colloidal solution are in constant Brownian motion. DLS monitors light scattering as a function of time and, when paired with the Stokes-Einstein assumption, is used to calculate the NP hydrodynamic diameter (the diameter of the NP and the solvent molecules that diffuse at the same rate as the colloid) in solution. To minimize multiple scattering, DLS requires a relatively low NP concentration.[95] Previous studies on the use of DLS as a characterization technique is shown in Table 2

Energy dispersive X-ray spectrometry (EDX)

This technique provides an overall map of the sample by analyzing near-surface components and estimating elemental proportions at various places. EDX is used to qualitatively and quantitatively determine the elemental composition of MnO NPs and other metal nanoparticles. X-rays are produced when an EDX electron beam bombards MnO NPs.[96] The emitted X-rays are analyzed both qualitatively and quantitatively. For quantitative analysis, the intensities of peaks are used to determine the concentration of individual elements in MnO NPs, but for qualitative analysis, the positions of each X-ray peak on the EDX spectrum are used to identify them. EDX is used in combination with SEM. An electron beam with an energy of 10-20 keV impacts the conducting sample's surface, causing X-rays to be emitted from the material. The energy of the emitted X-rays is determined by the substance under study.[82] Previous studies on the use of EDX as a characterization technique is shown in Table 2.

X-Ray diffractometer (XRD).

XRD can provide crystallographic information as well as phase purity.[97] The average crystallite size of MnO NPs is determined using the Debye-Scherrer formula.[98]

$$D = \frac{k\lambda}{\beta \cos\theta} \quad (1)$$

Where D is the average crystal size, λ is the X-ray wavelength, k is Scherrer constant and β is the full width at half maximum. a-MnO_2 exhibits XRD peaks at 2θ = 12.7°, 18.0°, 28.6°, 37.5°, 41.9°, and 49.7°.[99] The intensity of the peak grows as the synthesis temperature and synthesis time of the NPs increase, indicating that the NPs' crystallinity increases with temperature and reaction time and corresponds to standard values. Similarly, altering the reacting species ratio can promote crystallinity.[100] Previous studies on the use of XRD as a characterization technique is shown in Table 2. Furthermore, other techniques adopted for the characterization of biosynthesis MnO NPs are documented in Table 2.

Applications of MnO NPs

MnO NPs synthesized using plant extracts have been reported to exhibit numerous applications in many fields. Some applications of MnO NPs are discussed below as shown in Figure 3.

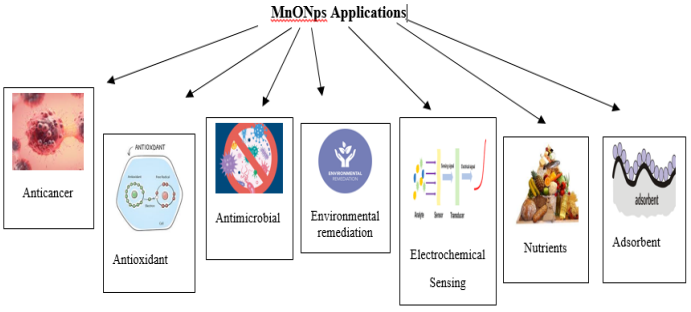

Figure 3. The various applications of MnO NPs

Table 2. Characterization techniques for synthesized MnO NPs[82,101-116]

Techniques	Purpose	Reference
Centrifugation	To separate the synthesized NPs from reaction solution.	101
Transmission electron microscopy (TEM)	Get High Resolution Pictures than a light microscope. Used to study the structure and presence of NPs.	101,102
Scanning electron microscope (SEM)	Get a three-dimensional appearance 3D based on the interaction of the electron beam with the specimen surface.	103
Scanning tunnelling microscopy (STM)	To study the local electronic structure of metal NPs as well as the structure and presence of NPs.	104
Ultraviolet-visible spectroscopy (UV-Vis)	Used for the optical study of the materials and to determine the synthesis of NPs.	101,105
Fourier transform infrared spectroscopy (FTIR)	To study the surface chemistry of metal NPs. Used for the identification of organic, inorganic, and polymeric materials utilizing infrared light for scanning the samples. Used to identify functional groups in the material.	82,106
X-ray diffraction (XRD)	Used for characterization of nanopowders of any sizes. Provide useful information and also help correlate microscopic observations with the bulk sample.	107,108
X-ray photoelectron spectroscopy (XPS)	Used to identify the elemental composition and chemical states of the elements present at the surface of a material.	109
Dynamic light scattering (DLS)	Used to measure the size of particle analyze complex colloidal systems.	101,110
Energy dispersive X-ray spectrometry (EDX)	Used to identify the elemental composition of a sample.	111,112
Atomic force microscopy (AFM)	Analyze complex colloidal systems obtains information by touching the sample's surface with a probe used to obtain high-resolution images. To study the size, shape, and surface roughness of metal NPs.	103,113
Dynamic light scattering (DLS)	Measure the hydrodynamic diameter of nanoparticles in solution.	114,115
Thermogravimetric analysis (TGA)	Study the thermal stability and decomposition of metal NPs.	116

Table 3. SPR bands, and functional groups, characterization techniques of biosynthesized MnO NPs from some plant sources[11,13-16,26,54,56,70,117-121]

Plants/Organisms names	Salt	SPR peak (nm)	Functional group prediction (cm^{-1})	Techniques	Shape	Size (nm)	Application	Ref.
Lemon methanolic extract	$Mn(OAc)_2.4H_2O$	360	OH 3650 C=O 1625 C-O 1026 C=C 1574 Mn-O 901	UV-VIS, FTIR, SEM, and HRTEM	-	50	Antibacterial and Antifungal	13
Kalopanax pictus leaf extract	$KMnO_4$		OH 3000 C=O 1623 C-O 1089 Mn-O 518	UV-VIS, XPS, FTIR, TEM, and EDX	Spherical	1–60	Dye degradation Electrochemical	15
clove, i.e., *Syzygium aromaticum* aqueous extract	$Mn(OAc)_2$	270	OH 3393 C=O 1707 C-O 1220 Mn-O 827	UV-VIS, XRD, FTIR, TGA, FESEM, DLS and TEM	-	4	Electrochemical	11
Phyllanthus amarus leaf extract	$Mn(OAc)_2.4H_2O$	360	OH 3433 C=O 1625 C-O 1021 C=C 1355 Mn-O 580	UV-VIS, XPS, FTIR, TGA, SEM, and TEM	Nanorod	40–50	Fluorescence studies	16

Abutilin indicum	$MnSO_4.H_2O$		OH 3250 C=O 1650 C-O 1060 C-H 2970 Mn-O 580	FTIR, UV-VIS, XRD, EDX and STM	Spherical	80	Photocatalytic and antibacterial	[26]
Ananas comosus (L.) peel extract	$KMnO_4$	-	OH 3450 C-H 2335 C-N 1384 Mn-O 626	FTIR, XPS, DLS and SEM	Spherical	10–34	Nutritional supplements	[117]
Dittrichia graveolens (L.) extract	$Mn(OAc)_2$	284	OH 3420 C=O 1650 C-O 1030 C=C 2917 Mn-O 798	UV-VIS, XRD, FTIR, and FESEM	Spherical	38	Dye degradation	[14]
Yucca gloriosa leaf extract	$Mn(OAc)_2$	410	OH 3400 C=O 1648 C-O 1050 C=C 2920 Mn-O 650	UV-VIS, XRD, FTIR, FESEM, TEM	Spherical	80	Dye degradation	[56]
Ocimum basilicum L leaves extract	$MnCl_2.4H_2O$	329	OH 3200 C=O 1550 C-O 1028 C-H 2900 N-H 1380 Mn-O 522	UV-Vis, XRD, FTIR, SEM and TEM	Spherical	6.5	Photocatalytic	[70]
Conocarpus erectus L leaves extract	$MnCl_2$	265	OH 3421 C=O 1638 C-C 1558 Mn-O 671	UV-VIS, XRD, FTIR, EDX, SEM, and AFM	Spherical	80	Nanofertilizer	[118]
Euphorbia heterophylla Leaves Extract	$MnCl_2.4H_2O$	-	OH 3245 C=O 1610 C-N 1071 Mn-O 559	XRD, FESEM, HRTEM, FTIR	Irregular shaped	13.5	-	[119]
Aloe vera	$KMnO_4$	-	OH 3378 C=O 1633 C-C 1060 C=C 1383 Mn-O 545	FTIR, XRD and FESEM	Spherical	22, 18 and 16	Antibacterial	[120]
Gardenia resinifera Leaf extract	$Mn(OAc)_2$	362	OH 3770 C-H 2924 C-N 1435 C≡C 2376 Mn-O 524	UV-VIS, XRD, FTIR, PSA, SEM, EDAX and HRTEM	Spherical	17-32	Antimicrobial activity	[121]
Bryophyllum pinnatum	$KMnO_4$		OH 3426 C-H 2924 C-O 1034 C=O 1618 Mn-O 524	UV-VIS, XRD, FTIR, SEM	Spherical	4-18	Magnetic property	[122]
Extracts of orange's juice	$KMnO_4$	-	-	TEM, XRD, TGA, BET	-	7.25	Electrochemical	[54]

Antibacterial

Green nanoparticles have demonstrated promising antibacterial efficacy against a variety of gram-negative and gram-positive bacteria. However, the mechanisms underlying growth inhibition and bactericidal effects are unclear. Notably, nanoparticle features such as form, size, and surface area, among others, have a significant impact on how they destroy bacterial cells. Manjula et al created manganese oxide nanoparticles using *Gardenia resinifera* leaf extract.[121] The scanning electron microscopy, or SEM, revealed the roughly spherical shape of manganese oxide with a size of around 17-32 nm. The antibacterial activity of synthesized MnO_2 nanoparticles was investigated using the agar well diffusion method. The concrete results indicate that Serratiam arcescens was the most sensitive microorganism with a maximum zone of inhibition (29 mm), followed by Pseudomonas aeruginosa (28 mm). In another study, the synthesis of manganese oxide via a green method using Lemon methanolic extract was reported.[13] The MnO NPs

exhibited the strongest antibacterial activity against S. aureus zone of inhibition (18 mm) and E. coli zone of inhibition (19 mm) and it showed moderate activity against S. bacillus zone of inhibition (17 mm). Therefore, the presence of an inhibition zone clearly indicates that the antibacterial activity of synthesized manganese nanoparticles against S. aureus is extremely superior to the standard drug, Chloramphenicol and nearly similar activity against E. coli bacteria.[122]

Dye Degradation

The paper and textile industries drain a vast volume of environmental contaminants, including carcinogenic natural and nondegradable colors. Photocatalytic techniques have received a lot of interest recently due to their ability to degrade dyes efficiently.[123–125] One study investigated the dye degradation activity of MnO_2 NPs to decompose Acid Orange.[56] In their study, MnO_2 NPs were also generated greenly utilizing Y. gloriosa extract. The photocatalytic activities of MnO_2 NPs for dye degradation were investigated with Acid Orange as an organic contaminant, and the results were promising. Time investigation of Acid Orange degradation revealed faster dye breakdown. The dye degradation activity of MnO_2 NPs was investigated using Congo Red and Safranin O dyes. MnO_2 NPs were also created utilizing a green technique involving K. pictus plant extracts.[15] MnO_2 nanoparticles were discovered to destroy two dyes: Congo red and Safranin O. Congo red and safranin O exhibited absorption maxima at 496 and 518 nm, respectively. Time course examination of Congo red degradation at absorption maxima revealed that biologically synthesized MnO_2 nanoparticles have a higher decolorization potential. Congo red was completely degraded in 8 minutes by biologically synthesized MnO_2 nanoparticles. The decolorization capacity of biologically synthesized MnO_2 nanoparticles for degrading safranin O was found to be almost same. The total degradation of safranin O was achieved within 10 to 15 minutes.

Electrochemical Application

Supercapacitors or electrochemical capacitors are energy storage devices that may provide tremendous power while also delivering energy in a short amount of time, unlike batteries. These devices are necessary for high-power supply applications such as electric/hybrid automobiles, backup memories, digital products, aeroplane emergency doors, micro-devices, mobile gadgets, and next-generation portable electronics. This is due to their low cost, low maintenance requirements, safety, short charging times, and high cycle life.[126] The use of synthesized MnO NPs in electrochemical sensing was investigated.[54] Green synthesized MnO NPs using orange peel extract were used to investigate the electrochemical characteristics and discharge performance of J-MnO_2 and P-MnO_2 NPs for possible usage as cathodes in lithium-ion batteries.[52] Galvanostatic charge-discharge investigations were carried out. The results showed that (OPMnO_2) has a greater surface area and lower K content than that made with orange juice extract (OJ-MnO_2). Higher surface area and reduced K content in OP-MnO_2 have a positive impact on its electrochemical characteristics. OP-MnO_2 has twice the capacitance of OJ-MnO_2 at a current density of 0.5 a per gram.

Magnetic Property

The magnetic characteristics of MnO nanoparticles was investigated.[126] SQUID analysis was used in their study to demonstrate the superparamagnetic behavior of MnO NPs. The SQUID results revealed MnO NPs' super-paramagnetic behavior, unlike Ullah et al.[121] study that used Bryophyllum pinnatum aqueous leaf extract as a reducing and capping agent to synthesize bio-molecule capped α-MnO_2 nanoparticles and study their magnetic properties. The study found that the α-MnO_2 nanoparticles exhibit modest ferromagnetic behavior at ambient temperature. At ground state, α-MnO_2 is antiferromagnetic due to its symmetric Mn-O-Mn bonds.[122] Biswas et al.[127] developed Mn-incorporated ZnS nanorods. The Mn-incorporated ZnS Nano-rods exhibited intense orange luminescence at approximately 585 nm. Lower Mn concentrations showed six-line hyperfine splitting in the Electron Paramagnetic Resonance (EPR) spectra, while higher Mn concentrations produced broad Lorentzian-shaped EPR spectra due to Mn-Mn cluster formation. Mn concentrations were ascribed to the Mn-Mn dipole interaction. The isolated Mn^{2+} ion and Mn cluster were also discovered using EPR.[127] EPR results indicate the presence of magnetic dipole interaction in Mn-incorporated ZnS nanorods with greater Mn concentrations. $Mn_xZn_{1-x}S$ NPs with favorable emission characteristics could be used in emissive devices.[127]

Fluorescence Property

MnO_2 nanorods were synthesized employing Phyllanthus amarus plant extract for its fluorescence activity. The fluorescence emission intensity of green synthesized MnO NPs at 518 nm was attributed to d-d transitions in Mn^{3+} ions.[16] The fluorescence emission observed in this situation may be owing to defects in the self-assembly of as-prepared Mn NPs. The d-d transitions in the associated Mn^{3+} ions can be strong due to static Jahn-Tellar distortion.[128] As a result, these could find useful applications in fluorescence-emitting materials.[16]

Nutritional Supplements

Manganese oxide nanoparticles was created from Ananas comosus (L.) peel and used them as dietary supplements for freshwater prawn Macrobrachium rosenbergii.[117] Manganese oxide nanoparticles were given to *M. rosenbergii* for 90 days. The study found that prawns fed a diet supplemented with Manganese oxide NPs had improved growth performance, digestive enzyme activities, muscle biochemical compositions, and total protein levels.[117] In addition, Manganese oxide NP supplementation greatly improved the activity of the antioxidant defense system and metabolic activities such as superoxide dismutase, catalase, glutamic oxaloacetate transaminase, and glutamic pyruvate transaminase. The study concluded that green synthesized Mn_2O_4 NPs were effective and safe as diet supplements for freshwater prawn Macrobrachium rosenbergii. According to this study, it could be used as a diet supplement for other aquatic species because it promotes prawn growth and an antioxidant defense system.[117]

CONCLUSION

The application of manganese oxide nanoparticles in the medicinal, energy storage devices, textiles, Dye degradation, water treatment, fluorescence-emitting materials and Nutritional supplement has garnered a great deal of interest, with a focus on development of more of eco-friendly, nontoxic, and environmentally benign methods using green biotechnology tools for production manganese oxide nanoparticles. This paper provides an overview of the green synthesis of manganese oxide NPs. This review provides insight to the potential of various natural extracts as replacements for physical and chemical methods of synthesizing nanoparticles, eliminating the need for additional capping agents or typical industrial surfactants that are challenging to remove post NPs synthesis and poses a threat to the environment. The recent characterization techniques used in examining the identities of manganese oxide nanoparticles were described in detail. To improve the green approach to synthesis, characterization and applications of manganese oxide nanoparticles more research should be carried out to provide more information regarding various factors that influence green synthesis of manganese oxide nanoparticles and the different techniques that can be used for characterization of the synthesized manganese oxide nanoparticles for its more efficient future applications in different industries.

Peer-review: Externally peer-reviewed.

Conflict of Interest: The author has no conflicts of interest to declare.

Financial Disclosure: The author declared that this study has received no financial support

REFERENCES

1. Burda C, Chen X, Narayanan R, El-Sayed MA. Chemistry and Properties of Nanocrystals of Different Shapes. *ChemInform*. 2005;36(27). doi:10.1002/chin.200527215
2. Sharma D, Kanchi S, Bisetty K. Biogenic synthesis of nanoparticles: A review. *Arab J Chem*. 2019;12(8):3576-3600. doi:10.1016/j.arabjc.2015.11.002
3. Islam MA, Morton DW, Johnson BB, Mainali B, Angove MJ. Manganese oxides and their application to metal ion and contaminant removal from wastewater. *J Water Process Eng*. 2018;26:264-280. doi:10.1016/j.jwpe.2018.10.018
4. Khan S, Hossain MK. Classification and properties of nanoparticles. In: *Nanoparticle-Based Polymer Composites*. Elsevier; 2022:15-54. doi:10.1016/B978-0-12-824272-8.00009-9
5. Giampiccolo A, Tobaldi DM, Jones E, et al. UV / visible sol gel W–TiO2 photocatalytic coatings for interior building surfaces. *Build Environ*. 2021;205(8):108203. doi:10.1016/j.buildenv.2021.108203
6. Narayanan KB, Sakthivel N. Green synthesis of biogenic metal nanoparticles by terrestrial and aquatic phototrophic and heterotrophic eukaryotes and biocompatible agents. *Adv Colloid Interface Sci*. 2011;169(2):59-79. doi:10.1016/j.cis.2011.08.004
7. Deng A, Zhu Y, Zhou L, Lin Y. Fabrication of TiO 2 -WO 3 hollow spheres via a templating technique for photocatalytic applications. *Micro Nano Lett*. 2018;13(1):12-17. doi:10.1049/mnl.2017.0264
8. Prasad AS. Green synthesis of nanocrystalline manganese (II, III) oxide. *Mater Sci Semicond Process*. 2017;71:342-347. doi:10.1016/j.mssp.2017.08.020
9. Veeramani H, Aruguete D, Monsegue N, et al. Low-Temperature Green Synthesis of Multivalent Manganese Oxide Nanowires. *ACS Sustain Chem Eng*. 2013;1(9):1070-1074. doi:10.1021/sc400129n
10. Sinha A, Singh VN, Mehta BR, Khare SK. Synthesis and characterization of monodispersed orthorhombic manganese oxide nanoparticles produced by Bacillus sp. cells simultaneous to its bioremediation. *J Hazard Mater*. 2011;192(2):620-627. doi:10.1016/j.jhazmat.2011.05.103
11. Kumar V, Singh K, Panwar S, Mehta SK. Green synthesis of manganese oxide nanoparticles for the electrochemical sensing of p-nitrophenol. *Int Nano Lett*. 2017;7(2):123-131. doi:10.1007/s40089-017-0205-3
12. Zhang H, Wu A, Fu H, et al. Efficient removal of Pb(<scp>ii</scp>) ions using manganese oxides: the role of crystal structure. *RSC Adv*. 2017;7(65):41228-41240. doi:10.1039/C7RA05955H
13. Jayandran M, Haneefa M, Balasubramanian V. Green synthesis and characterization of Manganese nanoparticles using natural plant extracts and its evaluation of antimicrobial activity. *J Appl Pharm Sci*. Published online 2015:105-110. doi:10.7324/JAPS.2015.501218
14. Souri M, Hoseinpour V, Ghaemi N, Shakeri A. Procedure optimization for green synthesis of manganese dioxide nanoparticles by Yucca gloriosa leaf extract. *Int Nano Lett*. 2019;9(1):73-81. doi:10.1007/s40089-018-0257-z
15. Moon SA, Salunke BK, Alkotaini B, Sathiyamoorthi E, Kim BS. Biological synthesis of manganese dioxide nanoparticles by Kalopanax pictus plant extract. *IET Nanobiotechnology*. 2015;9(4):220-225. doi:10.1049/iet-nbt.2014.0051
16. Prasad KS, Patra A. Green synthesis of MnO2 nanorods using Phyllanthus amarus plant extract and their fluorescence studies. *Green Process Synth*. 2017;6(6). doi:10.1515/gps-2016-0166
17. Abdelgawad AM, El-Naggar ME, Eisa WH, Rojas OJ. Clean and high-throughput production of silver nanoparticles mediated by soy protein via solid state synthesis. *J Clean Prod*. 2017;144:501-510. doi:10.1016/j.jclepro.2016.12.122
18. Sangeetha G, Rajeshwari S, Venckatesh R. Green synthesis of zinc oxide nanoparticles by aloe barbadensis miller leaf extract: Structure and optical properties. *Mater Res Bull*. 2011;46(12):2560-2566. doi:10.1016/j.materresbull.2011.07.046
19. Hoseinpour V, Ghaemi N. Green synthesis of manganese nanoparticles: Applications and future perspective–A review. *J Photochem Photobiol B Biol*. 2018;189:234-243. doi:10.1016/j.jphotobiol.2018.10.022
20. Koupaei MH, Shareghi B, Saboury AA, Davar F, Semnani A,

Evini M. Green synthesis of zinc oxide nanoparticles and their effect on the stability and activity of proteinase K. *RSC Adv*. 2016;6(48):42313-42323. doi:10.1039/C5RA24862K

21. Seabra AB, Haddad P, Duran N. Biogenic synthesis of nanostructured iron compounds: applications and perspectives. *IET Nanobiotechnology*. 2013;7(3):90-99. doi:10.1049/iet-nbt.2012.0047
22. Ain Samat N, Md Nor R. Sol–gel synthesis of zinc oxide nanoparticles using Citrus aurantifolia extracts. *Ceram Int*. 2013;39:S545-S548. doi:10.1016/j.ceramint.2012.10.132
23. Yamini G, Shakeri A, Zohuriaan-Mehr MJ, Kabiri K. Cyclocarbonated lignosulfonate as a bio-resourced reactive reinforcing agent for epoxy biocomposite: From natural waste to value-added bio-additive. *J CO2 Util*. 2018;24:50-58. doi:10.1016/j.jcou.2017.12.007
24. Ciorîță A, Suciu M, Macavei S, et al. Green Synthesis of Ag-MnO2 Nanoparticles using Chelidonium majus and Vinca minor Extracts and Their In Vitro Cytotoxicity. *Molecules*. 2020;25(4):819. doi:10.3390/molecules25040819
25. Khan SA, Shahid S, Lee C-S. Green Synthesis of Gold and Silver Nanoparticles Using Leaf Extract of Clerodendrum inerme; Characterization, Antimicrobial, and Antioxidant Activities. *Biomolecules*. 2020;10(6):835. doi:10.3390/biom10060835
26. Khan SA, Shahid S, Shahid B, Fatima U, Abbasi SA. Green Synthesis of MnO Nanoparticles Using Abutilon indicum Leaf Extract for Biological, Photocatalytic, and Adsorption Activities. *Biomolecules*. 2020;10(5):785. doi:10.3390/biom10050785
27. Hano C, Abbasi BH. Plant-Based Green Synthesis of Nanoparticles: Production, Characterization and Applications. *Biomolecules*. 2021;12(1):31. doi:10.3390/biom12010031
28. Gharehyakheh S, Ahmeda A, Haddadi A, et al. Effect of gold nanoparticles synthesized using the aqueous extract of <scp> *Satureja hortensis* </scp> leaf on enhancing the shelf life and removing <scp> *Escherichia coli* </scp> O157:H7 and <scp> *Listeria monocytogenes* </scp> in mince. *Appl Organomet Chem*. 2020;34(4). doi:10.1002/aoc.5492
29. Chandran SP, Chaudhary M, Pasricha R, Ahmad A, Sastry M. Synthesis of Gold Nanotriangles and Silver Nanoparticles Using Aloe vera Plant Extract. *Biotechnol Prog*. 2006;22(2):577-583. doi:10.1021/bp0501423
30. Kumar V, Yadav SK. Plant-mediated synthesis of silver and gold nanoparticles and their applications. *J Chem Technol Biotechnol*. 2009;84(2):151-157. doi:10.1002/jctb.2023
31. Muthukumar T, Sudhakumari, Sambandam B, Aravinthan A, Sastry TP, Kim J-H. Green synthesis of gold nanoparticles and their enhanced synergistic antitumor activity using HepG2 and MCF7 cells and its antibacterial effects. *Process Biochem*. 2016;51(3):384-391. doi:10.1016/j.procbio.2015.12.017
32. Jaganyi D, Altaf M, Wekesa I. Synthesis and characterization of whisker-shaped MnO2 nanostructure at room temperature. *Appl Nanosci*. 2013;3(4):329-333. doi:10.1007/s13204-012-0135-3
33. Ching S, Roark JL, Duan N, Suib SL. Sol−Gel Route to the Tunneled Manganese Oxide Cryptomelane. *Chem Mater*. 1997;9(3):750-754. doi:10.1021/cm960460k
34. Bastami TR, Entezari MH. Synthesis of manganese oxide nanocrystal by ultrasonic bath: Effect of external magnetic field. *Ultrason Sonochem*. 2012;19(4):830-840. doi:10.1016/j.ultsonch.2011.11.019
35. Liu X, Chen C, Zhao Y, Jia B. A Review on the Synthesis of Manganese Oxide Nanomaterials and Their Applications on Lithium-Ion Batteries. Yu B, ed. *J Nanomater*. 2013;2013(1). doi:10.1155/2013/736375
36. Pinc J, Bartůněk V, Kubásek J, Plecháček V, Hlásek T. Comparison of Mechanical and Superconducting Properties of YBaCuO and GdBaCuO Single Grains Prepared by Top-Seeded Melt Growth. *J Supercond Nov Magn*. 2016;29(7):1773-1778. doi:10.1007/s10948-016-3498-y
37. Cushing BL, Kolesnichenko VL, O'Connor CJ. Recent Advances in the Liquid-Phase Syntheses of Inorganic Nanoparticles. *Chem Rev*. 2004;104(9):3893-3946. doi:10.1021/cr030027b
38. Umamaheswari A, Lakshmana Prabu S, Puratchikody A. Biosynthesis of zinc oxide nanoparticle: a review on greener approach. *MOJ Bioequivalence Bioavailab*. 2018;5(3):151-154. doi:10.15406/mojbb.2018.05.00096
39. Bakeri G, Rahimnejad M. Kinetics study of hydrazodicarbonamide synthesis reaction. *Chem Ind Chem Eng Q*. 2013;19(2):273-279. doi:10.2298/CICEQ120221061B
40. Pirzadeh K, Ghoreyshi AA, Rahimnejad M, Mohammadi M. Electrochemical synthesis, characterization and application of a microstructure Cu3(BTC)2 metal organic framework for CO2 and CH4 separation. *Korean J Chem Eng*. 2018;35(4):974-983. doi:10.1007/s11814-017-0340-6
41. Umer A, Naveed S, Ramzan N, Rafique MS. Selection of a suitable method for the synthesis of copper nanoparticles. *Nano*. 2012;07(05):1230005. doi:10.1142/S1793292012300058
42. Giri PK, Bhattacharyya S, Singh DK, Kesavamoorthy R, Panigrahi BK, Nair KGM. Correlation between microstructure and optical properties of ZnO nanoparticles synthesized by ball milling. *J Appl Phys*. 2007;102(9). doi:10.1063/1.2804012
43. Dhandapani P, Siddarth AS, Kamalasekaran S, Maruthamuthu S, Rajagopal G. Bio-approach: Ureolytic bacteria mediated synthesis of ZnO nanocrystals on cotton fabric and evaluation of their antibacterial properties. *Carbohydr Polym*. 2014;103:448-455. doi:10.1016/j.carbpol.2013.12.074
44. Siddique MAB, Bithi UH, Ahmed AN, et al. Preparation of Manganese Oxide Nanoparticles with Enhanced Capacitive Properties Utilizing Gel Formation Method. *ACS Omega*. 2022;7(51):48007-48017. doi:10.1021/acsomega.2c05872
45. Mounika T, Belagali SL, Vadiraj KT. Manganese oxide nanoparticles synthesis route, characterization and optical properties. *Mater Today Proc*. 2023;75:72-76. doi:10.1016/j.matpr.2022.11.017

46. Kruis FE, Fissan H, Rellinghaus B. Sintering and evaporation characteristics of gas-phase synthesis of size-selected PbS nanoparticles. *Mater Sci Eng B*. 2000;69-70:329-334. doi:10.1016/S0921-5107(99)00298-6
47. Magnusson MH, Deppert K, Malm J-O, Bovin J-O, Samuelson L. Gold Nanoparticles: Production, Reshaping, and Thermal Charging. *J Nanoparticle Res*. 1999;1:243-251. doi:10.1023/A:1010012802415
48. Enríquez-Sánchez N, Vilchis-Nestor AR, Camacho-López S, Camacho-López MA, Camacho-López M. Influence of ablation time on the formation of manganese oxides synthesized by laser ablation of solids in liquids. *Opt Laser Technol*. 2020;131:106418. doi:10.1016/j.optlastec.2020.106418
49. Tsuji T, Iryo K, Watanabe N, Tsuji M. Preparation of silver nanoparticles by laser ablation in solution: influence of laser wavelength on particle size. *Appl Surf Sci*. 2002;202(1-2):80-85. doi:10.1016/S0169-4332(02)00936-4
50. Saravanan M, Barik SK, MubarakAli D, Prakash P, Pugazhendhi A. Synthesis of silver nanoparticles from Bacillus brevis (NCIM 2533) and their antibacterial activity against pathogenic bacteria. *Microb Pathog*. 2018;116:221-226. doi:10.1016/j.micpath.2018.01.038
51. Samuel MS, Jose S, Selvarajan E, Mathimani T, Pugazhendhi A. Biosynthesized silver nanoparticles using Bacillus amyloliquefaciens; Application for cytotoxicity effect on A549 cell line and photocatalytic degradation of p-nitrophenol. *J Photochem Photobiol B Biol*. 2020;202:111642. doi:10.1016/j.jphotobiol.2019.111642
52. Hosseini-Koupaei M, Shareghi B, Saboury AA, et al. Catalytic activity, structure and stability of proteinase K in the presence of biosynthesized CuO nanoparticles. *Int J Biol Macromol*. 2019;122:732-744. doi:10.1016/j.ijbiomac.2018.11.001
53. Iravani S. Green synthesis of metal nanoparticles using plants. *Green Chem*. 2011;13(10):2638. doi:10.1039/c1gc15386b
54. Abuzeid HM, Hashem AM, Kaus M, et al. Electrochemical performance of nanosized MnO2 synthesized by redox route using biological reducing agents. *J Alloys Compd*. 2018;746:227-237. doi:10.1016/j.jallcom.2018.02.260
55. Hashem AM, Abuzeid H, Kaus M, et al. Green synthesis of nanosized manganese dioxide as positive electrode for lithium-ion batteries using lemon juice and citrus peel. *Electrochim Acta*. 2018;262:74-81. doi:10.1016/j.electacta.2018.01.024
56. Hoseinpour V, Souri M, Ghaemi N. Green synthesis, characterisation, and photocatalytic activity of manganese dioxide nanoparticles. *Micro Nano Lett*. 2018;13(11):1560-1563. doi:10.1049/mnl.2018.5008
57. Perfileva AI, Krutovsky K V. Manganese Nanoparticles: Synthesis, Mechanisms of Influence on Plant Resistance to Stress, and Prospects for Application in Agricultural Chemistry. *J Agric Food Chem*. 2024;72(14):7564-7585. doi:10.1021/acs.jafc.3c07350
58. kazemi S, Hosseingholian A, Gohari SD, et al. Recent advances in green synthesized nanoparticles: from production to application. *Mater Today Sustain*. 2023;24:100500. doi:10.1016/j.mtsust.2023.100500
59. Gardea-Torresdey JL, Tiemann KJ, Gamez G, et al. Reduction and Accumulation of Gold(III) by Medicago sativa Alfalfa Biomass: X-ray Absorption Spectroscopy, pH, and Temperature Dependence. *Environ Sci Technol*. 2000;34(20):4392-4396. doi:10.1021/es991325m
60. Armendariz V, Herrera I, Peralta-videa JR, et al. Size controlled gold nanoparticle formation by Avena sativa biomass: use of plants in nanobiotechnology. *J Nanoparticle Res*. 2004;6(4):377-382. doi:10.1007/s11051-004-0741-4
61. Mühlen A zur, Mühlen E zur, Niehus H, Mehnert W. Atomic Force Microscopy Studies of Solid Lipid Nanoparticles. *Pharm Res*. 1996;13:1411-1416. doi:10.1023/a:1016042504830
62. Singhal G, Bhavesh R, Kasariya K, Sharma AR, Singh RP. Biosynthesis of silver nanoparticles using Ocimum sanctum (Tulsi) leaf extract and screening its antimicrobial activity. *J Nanoparticle Res*. 2011;13(7):2981-2988. doi:10.1007/s11051-010-0193-y
63. Kumara Swamy M, Sudipta KM, Jayanta K, Balasubramanya S. The green synthesis, characterization, and evaluation of the biological activities of silver nanoparticles synthesized from Leptadenia reticulata leaf extract. *Appl Nanosci*. 2015;5(1):73-81. doi:10.1007/s13204-014-0293-6
64. Varadavenkatesan T, Selvaraj R, Vinayagam R. Dye degradation and antibacterial activity of green synthesized silver nanoparticles using Ipomoea digitata Linn. flower extract. *Int J Environ Sci Technol*. 2019;16(5):2395-2404. doi:10.1007/s13762-018-1850-4
65. Ahmed S, Saifullah, Ahmad M, Swami BL, Ikram S. Green synthesis of silver nanoparticles using Azadirachta indica aqueous leaf extract. *J Radiat Res Appl Sci*. 2016;9(1):1-7. doi:10.1016/j.jrras.2015.06.006
66. Vinayagam R, Selvaraj R, Arivalagan P, Varadavenkatesan T. Synthesis, characterization and photocatalytic dye degradation capability of Calliandra haematocephala-mediated zinc oxide nanoflowers. *J Photochem Photobiol B Biol*. 2020;203:111760. doi:10.1016/j.jphotobiol.2019.111760
67. Sahayaraj K, Roobadevi M, Rajesh S, Azizi S. Vernonia cinerea (L.) Less. silver nanocomposite and its antibacterial activity against a cotton pathogen. *Res Chem Intermed*. 2015;41(8):5495-5507. doi:10.1007/s11164-014-1676-8
68. Anchan S, Pai S, Sridevi H, Varadavenkatesan T, Vinayagam R, Selvaraj R. Biogenic synthesis of ferric oxide nanoparticles using the leaf extract of Peltophorum pterocarpum and their catalytic dye degradation potential. *Biocatal Agric Biotechnol*. 2019;20:101251. doi:10.1016/j.bcab.2019.101251
69. Rai A, Singh A, Ahmad A, Sastry M. Role of Halide Ions and Temperature on the Morphology of Biologically Synthesized Gold Nanotriangles. *Langmuir*. 2006;22(2):736-741. doi:10.1021/la052055q

70. Islam B, Samir D, Sara C, Janetta N. Ocimum basilicum L. leaves extract-mediated green synthesis of MnO NPs: Phytochemical profile, characterization, catalytic and thrombolytic activities. *Results in Surfaces and Interfaces*. 2024;17:100284. doi:10.1016/j.rsurfi.2024.100284
71. Gholipour B, Shojaei S, Rostamnia S, et al. Metal-free nanostructured catalysts: sustainable driving forces for organic transformations. *Green Chem*. 2021;23(17):6223-6272. doi:10.1039/D1GC01366A
72. Darroudi M. Time-dependent effect in green synthesis of silver nanoparticles. *Int J Nanomedicine*. 2011;6:677. doi:10.2147/IJN.S17669
73. Izak-Nau E, Huk A, Reidy B, et al. Impact of storage conditions and storage time on silver nanoparticles' physicochemical properties and implications for their biological effects. *RSC Adv*. 2015;5(102):84172-84185. doi:10.1039/C5RA10187E
74. Mudunkotuwa IA, Pettibone JM, Grassian VH. Environmental Implications of Nanoparticle Aging in the Processing and Fate of Copper-Based Nanomaterials. *Environ Sci Technol*. 2012;46(13):7001-7010. doi:10.1021/es203851d
75. Baer DR. Surface Characterization of Nanoparticles. *J Surf Anal*. 2011;17(3):163-169. doi:10.1384/jsa.17.163
76. Park Y, Hong YN, Weyers A, Kim YS, Linhardt RJ. ChemInform Abstract: Polysaccharides and Phytochemicals: A Natural Reservoir for the Green Synthesis of Gold and Silver Nanoparticles. *ChemInform*. 2012;43(6). doi:10.1002/chin.201206264
77. Haverkamp RG, Marshall AT, van Agterveld D. Pick your carats: nanoparticles of gold–silver–copper alloy produced in vivo. *J Nanoparticle Res*. 2007;9(4):697-700. doi:10.1007/s11051-006-9198-y
78. de Toledo L de AS, Rosseto HC, Bruschi ML. Iron oxide magnetic nanoparticles as antimicrobials for therapeutics. *Pharm Dev Technol*. 2018;23(4):316-323. doi:10.1080/10837450.2017.1337793
79. Gholami L, Kazemi Oskuee R, Tafaghodi M, Ramezani Farkhani A, Darroudi M. Green facile synthesis of low-toxic superparamagnetic iron oxide nanoparticles (SPIONs) and their cytotoxicity effects toward Neuro2A and HUVEC cell lines. *Ceram Int*. 2018;44(8):9263-9268. doi:10.1016/j.ceramint.2018.02.137
80. Afsheen S, Tahir MB, Iqbal T, Liaqat A, Abrar M. Green synthesis and characterization of novel iron particles by using different extracts. *J Alloys Compd*. 2018;732:935-944. doi:10.1016/j.jallcom.2017.10.137
81. Reddy KR. Green synthesis, morphological and optical studies of CuO nanoparticles. *J Mol Struct*. 2017;1150:553-557. doi:10.1016/j.molstruc.2017.09.005
82. Titus D, James Jebaseelan Samuel E, Roopan SM. Nanoparticle characterization techniques. In: *Green Synthesis, Characterization and Applications of Nanoparticles*. Elsevier; 2019:303-319. doi:10.1016/B978-0-08-102579-6.00012-5
83. EL-Moslamy SH, Yahia IS, Zahran HY, Kamoun EA. Novel biosynthesis of MnO NPs using Mycoendophyte: industrial bioprocessing strategies and scaling-up production with its evaluation as anti-phytopathogenic agents. *Sci Rep*. 2023;13(1):2052. doi:10.1038/s41598-023-28749-z
84. Joshi NC, Joshi E, Singh A. Biological Synthesis, Characterisations and Antimicrobial activities of manganese dioxide (MnO2) nanoparticles. *Res J Pharm Technol*. 2020;13(1):135. doi:10.5958/0974-360X.2020.00027.X
85. Makvandi P, Wang C, Zare EN, Borzacchiello A, Niu L, Tay FR. Metal-Based Nanomaterials in Biomedical Applications: Antimicrobial Activity and Cytotoxicity Aspects. *Adv Funct Mater*. 2020;30(22). doi:10.1002/adfm.201910021
86. Chatterjee S, Ja A, Subramanian, A. Subramanian S. Synthesis and characterization of manganese dioxide using brassica oleracea (cabbage). *J Ind Pollut Control*. 2017;33(2):1627-1632.
87. Zuber A, Purdey M, Schartner E, et al. Detection of gold nanoparticles with different sizes using absorption and fluorescence based method. *Sensors Actuators B Chem*. 2016;227:117-127. doi:10.1016/j.snb.2015.12.044
88. Taha M, Hassan M, Essa S, Tartor Y. Use of Fourier transform infrared spectroscopy (FTIR) spectroscopy for rapid and accurate identification of Yeasts isolated from human and animals. *Int J Vet Sci Med*. 2013;1(1):15-20. doi:10.1016/j.ijvsm.2013.03.001
89. Pasquini A, Picotto GB, Pisani M. STM carbon nanotube tips fabrication for critical dimension measurements. *Sensors Actuators A Phys*. 2005;123-124:655-659. doi:10.1016/j.sna.2005.02.036
90. Binnig G, Quate CF, Gerber C. Atomic Force Microscope. *Phys Rev Lett*. 1986;56(9):930-933. doi:10.1103/PhysRevLett.56.930
91. Długosz O, Chwastowski J, Banach M. Hawthorn berries extract for the green synthesis of copper and silver nanoparticles. *Chem Pap*. 2020;74(1):239-252. doi:10.1007/s11696-019-00873-z
92. Mourdikoudis S, Pallares RM, Thanh NTK. Characterization techniques for nanoparticles: comparison and complementarity upon studying nanoparticle properties. *Nanoscale*. 2018;10(27):12871-12934. doi:10.1039/C8NR02278J
93. Das PE, Abu-Yousef IA, Majdalawieh AF, Narasimhan S, Poltronieri P. Green Synthesis of Encapsulated Copper Nanoparticles Using a Hydroalcoholic Extract of Moringa oleifera Leaves and Assessment of Their Antioxidant and Antimicrobial Activities. *Molecules*. 2020;25(3):555. doi:10.3390/molecules25030555
94. Ramadhan VB, Ni'mah YL, Yanuar E, Suprapto S. Synthesis of copper nanoparticles using Ocimum tenuiflorum leaf extract as capping agent. In: ; 2019:020067. doi:10.1063/1.5141680
95. Kato H. Size Determination of Nanoparticles by Dynamic Light Scattering. In: *Nanomaterials*. Wiley; 2012:535-554. doi:10.1002/9783527646821.ch8
96. Shiravand S, Mahmoudvand H, Ebrahimi K. Biosynthesis of

copper nanoparticles using aqueous extract of Capparis spinosa fruit and investigation of its antibacterial activity. *Marmara Pharm J*. 2017;21(4):866-871. doi:10.12991/mpj.2017.31
97. Wang X, Li Y. Selected-Control Hydrothermal Synthesis of α- and β-MnO 2 Single Crystal Nanowires. *J Am Chem Soc*. 2002;124(12):2880-2881. doi:10.1021/ja0177105
98. Lan B, Zheng X, Cheng G, et al. The art of balance: Engineering of structure defects and electrical conductivity of α-MnO2 for oxygen reduction reaction. *Electrochim Acta*. 2018;283:459-466. doi:10.1016/j.electacta.2018.06.195
99. Ibrahim AM, Munshi GH, Al-Harbi LM. Copper(II) oxide nanocatalyst preparation and characterization: green chemistry route. *Bull Natl Res Cent*. 2018;42(1):6. doi:10.1186/s42269-018-0006-5
100. Zhou J, Yu L, Sun M, et al. Novel Synthesis of Birnessite-Type MnO 2 Nanostructure for Water Treatment and Electrochemical Capacitor. *Ind Eng Chem Res*. 2013;52(28):9586-9593. doi:10.1021/ie400577a
101. Patil MP, Kim G-D. Marine microorganisms for synthesis of metallic nanoparticles and their biomedical applications. *Colloids Surfaces B Biointerfaces*. 2018;172:487-495. doi:10.1016/j.colsurfb.2018.09.007
102. Kohl H, Reimer L. *Transmission Electron Microscopy*. Vol 36. Springer New York; 2008. doi:10.1007/978-0-387-40093-8
103. Delvallée A, Feltin N, Ducourtieux S, Trabelsi M, Hochepied JF. Direct comparison of AFM and SEM measurements on the same set of nanoparticles. *Meas Sci Technol*. 2015;26(8):085601. doi:10.1088/0957-0233/26/8/085601
104. Wiesendanger R, Güntherodt H-J, eds. *Scanning Tunneling Microscopy III*. Vol 29. Springer Berlin Heidelberg; 1996. doi:10.1007/978-3-642-80118-1
105. Rocha FS, Gomes AJ, Lunardi CN, Kaliaguine S, Patience GS. Experimental methods in chemical engineering: Ultraviolet visible spectroscopy—UV-Vis. *Can J Chem Eng*. 2018;96(12):2512-2517. doi:10.1002/cjce.23344
106. Praseptiangga D, Zahara HL, Widjanarko PI, Joni IM, Panatarani C. Preparation and FTIR spectroscopic studies of SiO2-ZnO nanoparticles suspension for the development of carrageenan-based bio-nanocomposite film. In: ; 2020:100005. doi:10.1063/5.0003434
107. Kahle M, Kleber M, Jahn R. Review of XRD-based quantitative analyses of clay minerals in soils: the suitability of mineral intensity factors. *Geoderma*. 2002;109(3-4):191-205. doi:10.1016/S0016-7061(02)00175-1
108. Holder CF, Schaak RE. Tutorial on Powder X-ray Diffraction for Characterizing Nanoscale Materials. *ACS Nano*. 2019;13(7):7359-7365. doi:10.1021/acsnano.9b05157
109. Greczynski G, Hultman L. X-ray photoelectron spectroscopy: Towards reliable binding energy referencing. *Prog Mater Sci*. 2020;107:100591. doi:10.1016/j.pmatsci.2019.100591
110. Hoo CM, Starostin N, West P, Mecartney ML. A comparison of atomic force microscopy (AFM) and dynamic light scattering (DLS) methods to characterize nanoparticle size distributions. *J Nanoparticle Res*. 2008;10(S1):89-96. doi:10.1007/s11051-008-9435-7
111. Newbury DE, Ritchie NWM. Is Scanning Electron Microscopy/Energy Dispersive X-ray Spectrometry (SEM/EDS) Quantitative? *Scanning*. 2013;35(3):141-168. doi:10.1002/sca.21041
112. Giurlani W, Innocenti M, Lavacchi A. X-ray Microanalysis of Precious Metal Thin Films: Thickness and Composition Determination. *Coatings*. 2018;8(2):84. doi:10.3390/coatings8020084
113. Cadene A, Durand-Vidal S, Turq P, Brendle J. Study of individual Na-montmorillonite particles size, morphology, and apparent charge. *J Colloid Interface Sci*. 2005;285(2):719-730. doi:10.1016/j.jcis.2004.12.016
114. de la Calle I, Menta M, Klein M, Séby F. Study of the presence of micro- and nanoparticles in drinks and foods by multiple analytical techniques. *Food Chem*. 2018;266:133-145. doi:10.1016/j.foodchem.2018.05.107
115. Falke S, Betzel C. Dynamic Light Scattering (DLS). In: ; 2019:173-193. doi:10.1007/978-3-030-28247-9_6
116. Saldarriaga JF, Aguado R, Pablos A, Amutio M, Olazar M, Bilbao J. Fast characterization of biomass fuels by thermogravimetric analysis (TGA). *Fuel*. 2015;140:744-751. doi:10.1016/j.fuel.2014.10.024
117. Asaikkutti A, Bhavan PS, Vimala K, Karthik M, Cheruparambath P. Dietary supplementation of green synthesized manganese-oxide nanoparticles and its effect on growth performance, muscle composition and digestive enzyme activities of the giant freshwater prawn Macrobrachium rosenbergii. *J Trace Elem Med Biol*. 2016;35:7-17. doi:10.1016/j.jtemb.2016.01.005
118. Abdulameer SA, Edan R. Green synthesis of manganese oxide Nnaoparticles by aueous extract of Conocarpus erectus L. leaves. *HIV Nurs*. 2023;23(3):2009-2013.
119. Dewi NOM, Yulizar Y. Euphorbia heterophylla L. Leaf Extract-Mediated Synthesis of MnO2 Nanoparticles and Its Characterization. *Mater Today Proc*. 2020;22:199-204. doi:10.1016/j.matpr.2019.08.088
120. Joshi NC, Siddiqui F, Salman M, Singh A. Antibacterial Activity, Characterizations, and Biological Synthesis of Manganese Oxide Nanoparticles using the Extract of Aloe vera. *Asian Pacific J Heal Sci*. 2020;7(3):27-29. doi:10.21276/apjhs.2020.7.3.7
121. Manjula R, Thenmozhi M, Thilagavathi S, Srinivasan R, Kathirvel A. Green synthesis and characterization of manganese oxide nanoparticles from Gardenia resinifera leaves. *Mater Today Proc*. 2020;26:3559-3563. doi:10.1016/j.matpr.2019.07.396
122. Ullah AKMA, Haque MM, Akter M, et al. Green synthesis of Bryophyllum pinnatum aqueous leaf extract mediated bio-molecule capped dilute ferromagnetic α-MnO 2 nanoparticles. *Mater Res Express*. 2020;7(1):015088. doi:10.1088/2053-1591/ab6c20
123. Sankar R, Manikandan P, Malarvizhi V, Fathima T, Shivashangari KS, Ravikumar V. Green synthesis of colloidal copper oxide nanoparticles using Carica papaya and its

application in photocatalytic dye degradation. *Spectrochim Acta Part A Mol Biomol Spectrosc*. 2014;121:746-750. doi:10.1016/j.saa.2013.12.020

124. Pung S-Y, Chan Y-L, Sreekantan S, Yeoh F-Y. Photocatalytic activity of ZnO-MnO 2 core shell nanocomposite in degradation of RhB dye. *Pigment Resin Technol*. 2016;45(6):408-418. doi:10.1108/PRT-08-2015-0082
125. Wang J, Zhang W-D, Ouyang W-X, Yu Y-X. Hierarchically branched ZnO/CuO thin film with enhanced visible light photoelectrochemical property. *Mater Lett*. 2015;154:44-46. doi:10.1016/j.matlet.2015.04.048
126. Lokhande P., Panda H. Synthesis and Characterization of Ni.Co(OH)2 Material for Supercapacitor Application. *Int Adv Res J Sci Eng Technol*. 2015;2(8):10-13. doi:10.17148/IARJSET.2015.2903
127. Biswas S, Kar S, Chaudhuri S. Optical and Magnetic Properties of Manganese-Incorporated Zinc Sulfide Nanorods Synthesized by a Solvothermal Process. *J Phys Chem B*. 2005;109(37):17526-17530. doi:10.1021/jp053138i
128. Toufiq AM, Wang F, Javed Q-U-A, Li Q, Li Y, Khan M. Synthesis, characterization and photoluminescent properties of 3D nanostructures self-assembled with Mn3O4 nanoparticles. *Mater Express*. 2014;4(3):258-262. doi:10.1166/mex.2014.1167